CHALMERS
UNIVERSITY OF TECHNOLOGY

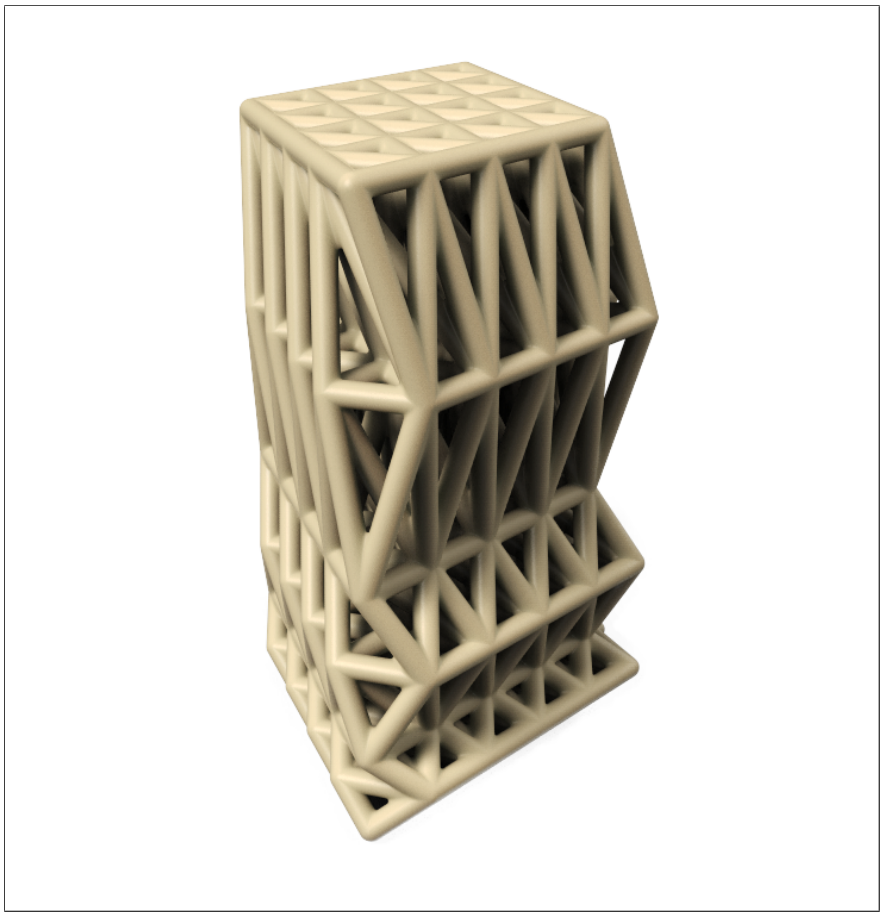

Material Characterization of 3D-Printed Energy-Absorbent Polymers Inspired by Nature

ERIK SVENSSON

Department of Materials and Manufacturing Technology
CHALMERS UNIVERSITY OF TECHNOLOGY
Gothenburg, Sweden 2017

Master's thesis 2017:192

Material characterization of 3D-printed energy-absorbent polymers inspired by nature

ERIK SVENSSON

CHALMERS
UNIVERSITY OF TECHNOLOGY

Department of Materials and Manufacturing Technology
Chalmers University of Technology
Gothenburg, Sweden 2017

Material characterization of 3D-printed energy-absorbent polymers
inspired by nature
ERIK SVENSSON

Supervisors:
Dr. Roland Dr. Spyros A. Tsampas, Research Engineer, Swerea SICOMP
Dr. Vasan Churchill SC, Research Engineer, Swerea SICOMP
Examiner:
Dr. Roland Kádár, Department of Materials and Manufacturing Technology

Master's Thesis 2017:192
Department of Materials and Manufacturing Technology
Chalmers University of Technology
SE-412 96 Gothenburg
Telephone +46 31 772 1000

Cover: Optimized 3D-printed tetrahedral structure in nylon by Markforged.
Collaborative work together with a parallel thesis project at
Department of Applied Mechanics, Chalmers and Swerea SICOMP [51].

Typeset in LaTeX
Printed by Chalmers Reproservice
Gothenburg, Sweden 2017

Material characterization of 3D-printed energy-absorbent polymers inspired by nature

ERIK SVENSSON
Department of Materials and Manufacturing Technology
Chalmers University of Technology

Abstract

The impact-absorbing liners of helmets are nowadays made of polymeric foams with uniform density throughout the thickness with a fit-for-all approach for the user. Using the latest manufacturing methods, a customizable solution with optimized arrangement is possible by utilizing concepts inspired by nature.

As of today, nature has been an inspiration for engineering design such as Velcro® with the hook-like structure; hydrophobic surfaces from lotus flower; anti-slip shoe soles with wave-like grooves inspired by dog paws; low drag swimsuits inspired by shark skin. But reproducing the natural structures has been limited due to today's conventional manufacturing because of the hierarchical structures utilized in nature. Wegst et al. [23] however suggests that this is about to change with the increasing use of additive manufacturing.

Implementing bio-inspired materials with the increasing popularity of additive manufacturing is now possible. This leads to enhanced material performance by optimizing its architecture using inspiration from nature. This also allows for complex geometries and gradient material properties. Additionally, this will effectively lead to improved energy absorbing properties combined with weight saving and optimized design.

In this study the commercially available 3D-printer filaments such as ABS, PLA, Nylon (PA) and TPU were characterized. These materials were 3D-printed and tested using tensile testing and Dynamic Mechanical Thermal Analysis (DMTA) to determine properties such as elastic modulus, tensile strength and glass-transition temperature.

In a comparative study and discussion with a parallel thesis project it was shown that Nylon by Markforged is the most appropriate choice of filament for impact absorbing applications of the tested materials. Based on the results and considering the time constraints, three optimized lattice structures were printed and tested in compression as a proof of concept for bio-inspired density gradient using today's commercially available 3D-printers.

Keywords: 3D-printing, impact absorbent, polymer, biomimicry, helmet, PA, ABS, TPU, PLA, material characterization, tensile testing, DMTA.

Acknowledgements

Thank you to Swerea SICOMP for conducting this MSc thesis together with the Department of Materials and Manufacturing Technology at Chalmers.

Thanks to Mattias Naarttijärvi and Alexander Olsson of the Applied Mechanics Department at Chalmers for the optimized structures based on found results from this study. Additional thanks for their inputs and discussions.

A dedicated thank you to Spyros Tsampas and Vasan Churchill SC for supervising and dedicating their time to help me throughout this project.

Additional thanks for inputs and discussions by Erik Marklund and Robin Olsson at Swerea SICOMP. Thanks to Johan Landberg and Peter Hellström for helping me with the experimental parts at Swerea IVF/SICOMP.

Thanks to Emil Johansson, Lenny Tönnäng and Jan Johansson at Swerea IVF for support and help on the additive manufacturing troubleshooting and providing software licenses.

Additional thank you to Swerea SICOMP in Piteå for providing the Nylon tensile test data.

Thanks to everyone involved in the MOTORIST project for discussion and generation of new ideas.

Thanks for the support and supervision by Siamak Farajzadeh Khosroshahi.

Thanks to Roland Kádár as the academic supervisor and examiner.

Finally, thanks to Jakob von Essen at Luleå University of Technology, LTU for his valuable suggestions and corrections.

Erik Svensson, Gothenburg, June 2017

Nomenclature

Symbol	Description
E'	Storage modulus
E"	Loss modulus
E^*	Complex modulus
$\tan(\delta)$	Loss factor/damping
T_g	Glass-transition temperature
T_m	Melting temperature
T_t	Peak temperature (DMTA)
t	Thickness
w, h	Width
L	Length
E	Elastic modulus
ρ	Density
ρ_{ratio}	Aspect ratio
σ	Stress
σ_u	Tensile strength
σ_y	Yield strength
ϵ	Strain
ϵ_B	Elongation at break %
F	Load
δ	Elongation
σ_{eng}	Engineering stress
ϵ_{eng}	Engineering strain
σ_{true}	True stress
ϵ_{true}	True strain
G_p	Shear modulus
FDM	Fused Deposition Modeling
AM	Additive Manufacturing
SL	StereoLitography
SLS	Selective Laser Sintering
CLIP	Continuous Liquid Interface Production
DLP	Digital Light Processing
RP	Rapid prototyping
PLS	Polymer/Layered Silicate
CNC	Computer Numerically Controlled
ABS	Acrylonitrile-butadiene-styrene
PLA	Polylactic Acid
PU	Polyurethane
PA	Polyamide (Nylon)
TPE	Thermoplastic elastomer
DMTA	Dynamic Mechanical Thermal Analysis
$\dot{V}_{extrusion}$	Extrusion multiplier
v_{nozzle}	Printing speed

Contents

List of Figures

List of Tables

1
Introduction

In nature there is a wealth of mineral-based and protein-based bio-composites specially designed to resist impact and crushing. Some examples are enamel, dentin, horn, hoof and bone among others which are exhibiting unique reinforcing and toughening mechanisms that allow them to withstand large impact- and compressive loads [1]. Such bio-composites feature complex multi-scale and hierarchical structures with several levels and types of reinforcements, density/stiffness gradients and porous phases that act in synergy to efficiently absorb the impact energy [70].

These multiscale architectures/concepts will be utilized to aid the designing of lighter, safer and tailored helmet liners for cyclists, motorcyclists and athletes. This means moving from the conventional EPS foams used nowadays as liner material, to a customized architecture with a liner based on the rider's skull. But also the head morphology/physiology and impact resistance/absorption requirements mimicking architectures found in nature.

The effectiveness of such structures is an example of concepts inspired by nature that can be used to realize more customized/purpose-built and energy absorbing architectures, a process called biomimicry. For centuries, designers and architects have been looking to nature for inspiration for the best source of inspiration with its 3.85 billion years of evolution [42]. Today, the tailored density gradient, nature's ability to rearrange its structure as well as the self-healing property found in e.g. bones is not achievable using any conventional manufacturing, therefore additive manufacturing is the way forward for solving the tailored density gradient problem.

In additive manufacturing or 3D-printing, three-dimensional objects/components are manufactured by deposition of materials in a layer-by-layer fashion. The layer thickness and path are controlled by computer models. Such a manufacturing approach has received rather large global attention the last few years. The reason is that very complex objects can be built which are difficult or impossible to create using conventional, subtractive manufacturing methods. This new way of manufacturing can produce highly customizable components with minimal material waste.

Considering the high complexity of the aforementioned bio-composite structures and the vast capabilities of additive manufacturing, it is foreseen that the combination would enable the realization of complicated 3D-printed architectures capable of withstanding impact and crushing inspired by the long-proven strategies found in living organisms and animals.

2

Background

2.1 Helmet fundamentals

2.1.1 Components and materials

The helmet is generally constructed of two major parts: the shell and the liner. A typical bicycle helmet can be seen in Figure 2.1. The shell is a hard outer protection layer which absorbs and distributes the concentrated impact force thus increasing the energy absorption of the underlying liner [2]. The material of the shell is usually acrylonitrile-butadiene-styrene (ABS) [54] and nowadays more and more fiber reinforced polymers (FRP) featuring carbon or aramid fibers/fabrics.

Figure 2.1: Foam, liner and padding of a bicycle helmet [6].

The liner is made of a shock-absorbing foam, usually expanded polystyrene (EPS) which is the most commonly used one in both bicycle- and motorcycle helmets today. Its role is to reduce the peak translational acceleration and increase the pulse duration [54], i.e. increasing the stopping time of the head during an impact in order to reduce the risk of brain injury. The liner acts as a crushable foam and slowly collapses during the impact [2]. Furthermore, as the compression of the foam liner is permanent, helmets must be discarded after experiencing larger impacts as the foam liner would not exhibit adequate head protection properties and thus serve its design purpose [54].

The polymerization process of EPS produces spherical beads. Products made from EPS are processed via three stages: Pre-expansion where the beads are expanded between 40–50 times their original size, conditioning where equilibrium temperature and pressure are met and finally moulding where the material is formed into customised products [19].

2.1.2 Design, manufacturing & performance

The mechanical response of the helmet is mostly affected by its design. The liner needs to be thick and soft. A thicker foam stops an impact better, but too thick and the helmet becomes too heavy and the aesthetic aspects of the helmet are reduced drastically. There are general standard test methods where the helmet is impacted on different anvils and the accelerometer inside the headform must decelerate below 300 g, which is 300 times the acceleration of gravity. The American National Standard (ANSI Z90.4) uses a falling headform striking a rigid flat steel plate or a hemisphere of steel with a 50 mm radius to test bicycle helmets [89].

To decelerate according to the Head Injury Criteria (HIC) standard [8], the thickness of the foam is usually in the region of 20-50 mm. Striking a balance between the thickness of the foam and its density is one of the most important factors to successfully handle an impact [2][17].

There are two categories of foams: open-cell and closed-cell, see Figure 2.2. The closed-cell structure consists of walls and struts, encompassing gas, whereas an open-cell structure consists solely of struts. The work accumulated in open-cell foam is basically the energy required for buckling of struts and pushing air out of the structure. A closed-cell foam absorbs energy through strut buckling, cell wall bending and the compression of trapped gas.

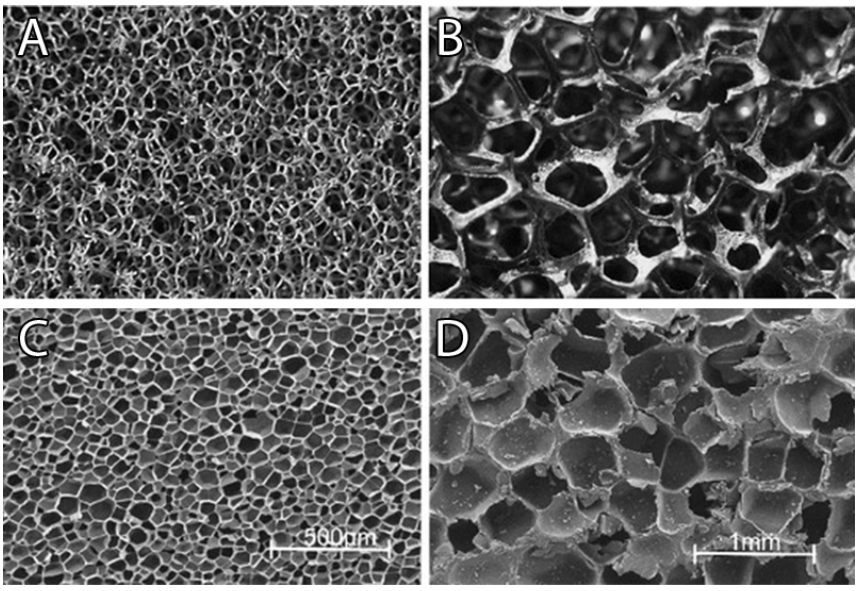

Figure 2.2: Open- (A and B) and close-celled (C and D) polymeric foams, after Berinskii et al. (2015) [13] (used with permission).

The characteristic curve of a compressive behaviour for a foam usually consists of three regimes. Initially, the linear elastic region where a low amount of energy is absorbed. Then a plateau region where the stress is constant followed by a densification where the stress is increasing sharply [44]. A typical behaviour of a foam stress-strain curve can be seen in Figure 2.3.

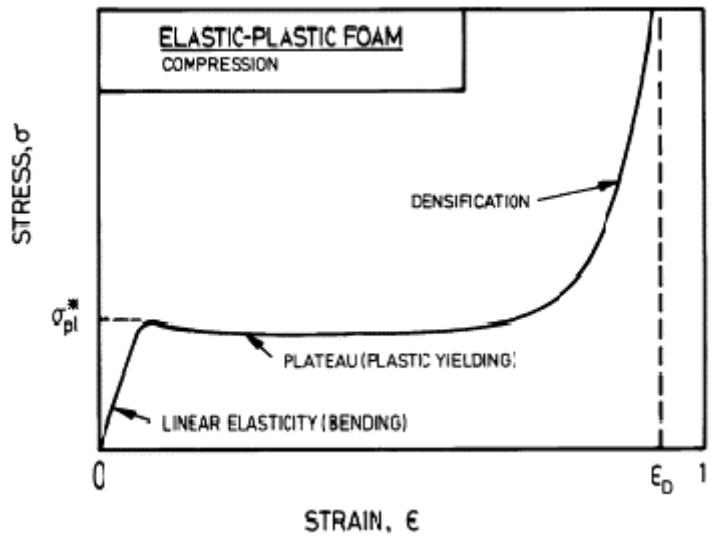

Figure 2.3: Typical stress-strain curve for a foam structure [26] (used with permission).

Studies on the impact response of bicycle helmets at different impact severities performed by DeMarco et al. suggested that an increased thickness of the liner generally reduces the acceleration at higher impact velocities [28]. Brennan-Craddock et al. demonstrated in preliminary tests that lattice structures designed by additive manufacturing can show similar compressive property responses compared to that of conventional foams by utilizing the geometric complexity available using 3D-printing [44].

Further studies on helmets designed with additive manufacturing were performed by Soe et al. where the focus was to evaluate the usage of thermoplastic elastomers (TPEs) in the liner of the helmet. The used method was selective laser sintering (SLS) and the foam had a cellular structure. The results showed reduced acceleration and pulse duration, thus demonstrating an improved energy-dissipation [54]. More on additive manufacturing methods and its materials can be found in section 2.4.

2.2 Energy absorbent materials & architectures found in nature

Natural biological materials are lightweight and impact-resistant tissues built with a handful of major elements such as C, O, H, P, N, S, Ca and Si. They are efficient, meaning that they fulfill complex requirements with using as little material as possible. Typical requirements could be to support static or dynamic loads, the need to store and release elastic energy or resistance to fracture. In contrast to engineering structures, the building material is accumulated and later hardened in specific locations e.g. where bending stresses are present [25]. This process is called bio-mineralization, a process dedicated to deposit minerals to a soft-matrix in order to both strengthen and stiffen it [53]. With increased strength the resistance to fracture is sacrificed/compromised, see Figure 2.4. This would suggest that the polymer of choice that is best dedicated to impact loading should have a low mineral content [1]. Figure 2.4 shows on the left y-axis the work of fracture (WOF) defined as the material's resistance to continued fracture in the presence of a crack. The right y-axis shows the bending strength.

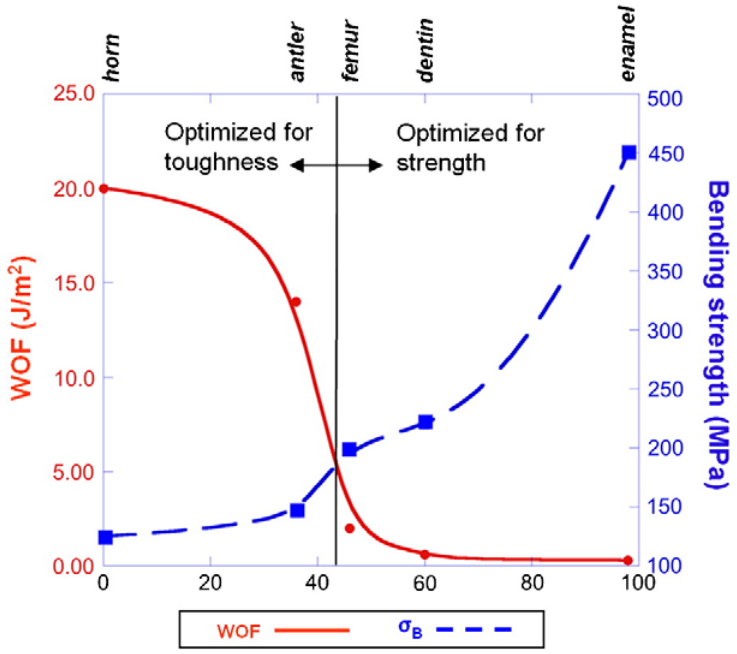

Figure 2.4: Effect of mineralization for various bio-composites [1] (used with permission).

Most natural materials are recyclable thus making them an environmentally friendly alternative for modern day engineering. The biological materials show a synergistic relation between the bio-polymer and mineral phase. They are both dependent on each other to exhibit its multi-objective mechanical properties. As previously mentioned, nature utilizes a limited resource of polymeric and ceramic components that can be thought of as building blocks which usually can be considered as composites [1][23].

Design strategies in nature

Animal tissues consist largely of collagen, elastin, keratin, chitin and minerals. Collagen and hydroxyapatite (HAp) are the basic structural elements for both soft and hard tissues in animals. Studies on natural materials subjected to impact such as bones, teeth, tusks and hooves, all part of mammalian structural materials, have been performed by McKittrick et al. [1] In their studies they managed to establish the relationships between structural and mechanical properties of these materials which is a major step in the design of bio-inspired materials [1].

One particular design strategy found in bones, antlers, teeth, horns and hooves is the presence of multiple reinforcing layers with energy absorbing properties as well as unique deformation mechanisms. Another similarity was the usage of hierarchical structures and the materials all showing an anisotropic behaviour due to the presence of tubules and structural protein fibers embedded in the hierarchical structures [1]. Additionally, natural materials can have both layered and columnar or fibrous patterns. They are often found in combinations. Man-made composites reinforced with complex fiber arrangements such as textile ceramic composites come close, but have yet to match the complexity of natural materials which are characterized by features spanning over multiple length scales [53].

Nanocrystalline reinforcements

In bones and teeth, additional reinforcement is achieved by nanocrystalline carbonated hydroxyapatite crystals in the form of platelets having a large aspect ratio ($\rho_{ratio} = 7$ for hydroxyapatite), this ratio gives a higher elastic modulus [1]. This mineral phase can therefore be considered as nanocrystalline. Furthermore, the biological composites exhibit a toughness several orders of magnitude higher than a single-phase mineral [1].

Finally, since the mineral phase is nanocrystalline, it does not fracture but rather strengthens the matrix. This can be demonstrated through the Griffith equation for failure strength which for bone (35–40 µm) shows a critical flaw size much higher than the size of the minerals (50 nm). Failure in composite is therefore not through brittle fracture of the mineral phase. The interaction between mineral phase and the bio-polymer is very high and both mechanical and chemical in nature, thus the rules of mixture cannot describe its mechanical properties [1].

Biomimetics

Bio-inspired materials are synthetically man-made materials fabricated to mimic the mechanical properties and structure of biological materials. The challenge to successfully mimic these biological materials lies in the need for multi-materials that synergistically can exhibit both high toughness and strength [23]. The relationship between the structure and function of a material usually stems from its surface structure [43]. The fine structure plays an important role in the organism and can be considered the first step for successfully replicating materials found in nature using biomimetics [43].

The natural materials have a similar behaviour as polymers, in that their yield strength and toughness both increase with increased strain rate. This is due to the lack of necessary time needed for proper alignment and thus acting like a polymer network [1].

Ashby charts

The materials found in nature have an outstanding range of mechanical properties. These are most easily presented in material property charts, more commonly known as Ashby charts. Different material indices can be plotted against each other to easily identify materials with extreme values of indices for different loading cases without experiencing failure [23].

All materials of the same characteristic class appears in bubbles as shown in Figure 2.5. The width is determined by the composition and micro-structure of the material. In the case of natural material this is determined by the growth condition and age, whereas this is controlled by the manufacturing process itself for engineering materials [23]. Note the clear superiority of the natural polymers found in the top right corner of Figure 2.5.

The property charts become more comparable by using material indices, also known as guidelines. This makes material selection for a specific application possible using "Ashby-charts" [23]. The toughness of a material is measured by the material's resistance to propagation of a pre-existing crack. The material with the best ability to absorb a given impact energy without failing has the largest value of toughness ($M_1 = J_c$). Those materials are found in the top of Figure 2.5, particularly antler and wood. Antlers is very impact resistant due to their low mineralization [4]. The toughness modulus is defined as the area under a stress-strain curve and is a widely used metric for the fracture resistance of biological materials [35]. When a material already contains a crack, the safest choice would then be the one with the largest fracture toughness value $M_2 = K_{1c} \approx (EJ_c)^{1/2}$.

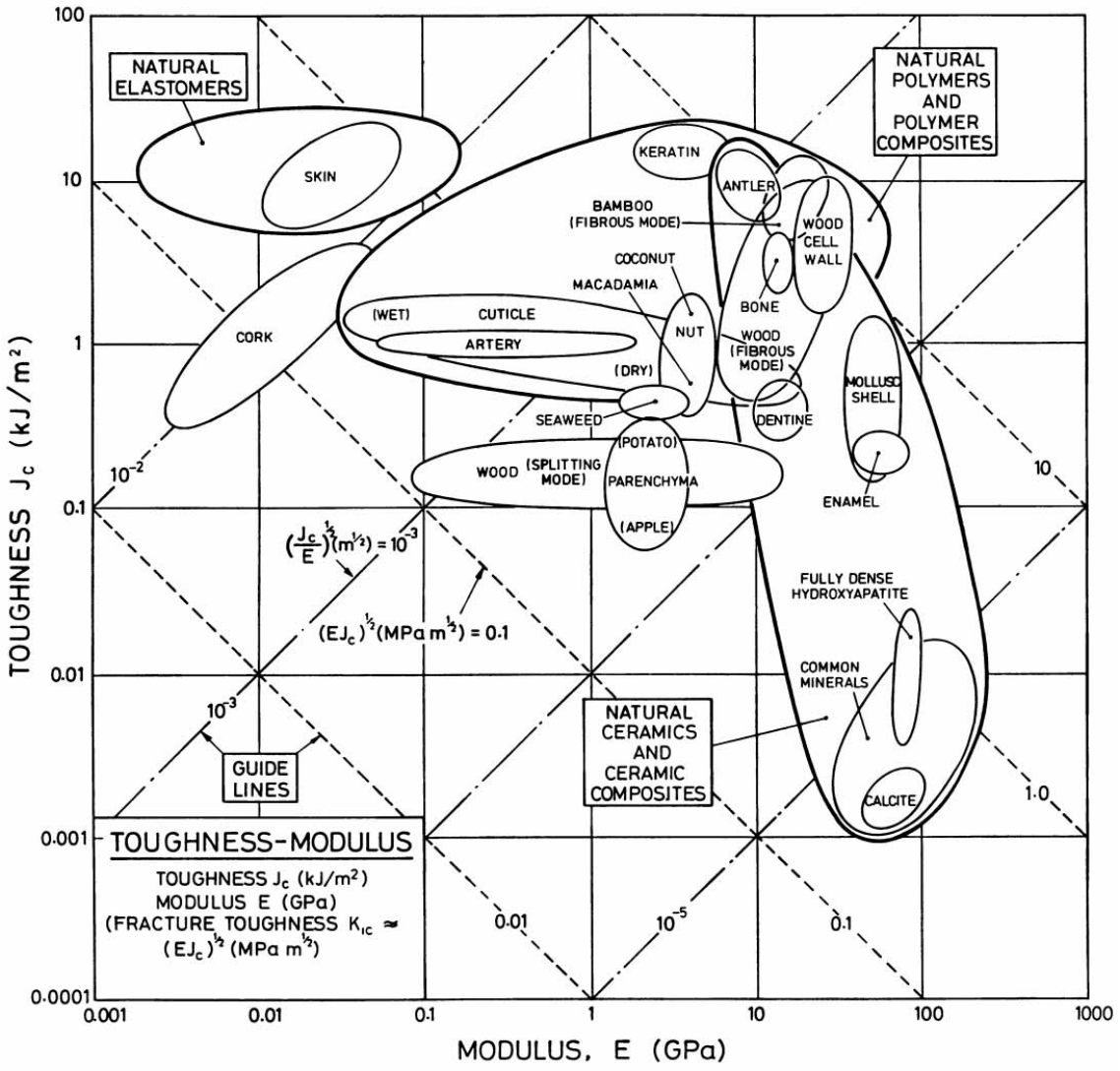

Figure 2.5: Ashby chart showing toughness vs. elastic modulus for various materials [23] (used with permission).

Many engineering materials such as aluminum and its alloys have higher toughness and fracture toughness than the most prominent natural materials. However, the toughness of natural ceramics such as bone, enamel, dentine and nacre are an order of magnitude higher than conventionally manufactured engineering ceramics such as alumina. The toughness comes from the microstructure: platelets of ceramics such as aragonite, calcite and hydroxyapatite bonded in a small volume fraction of polymer. Their toughness increases with a decreased mineral content and increasing collagen content [23]. Additionally, the hardness value increases with increased mineral content. McKittrick et al. found that the yield strength can be related as approximately 1/3 of the hardness value, this shows that the yield strength is expected to increase with an increased mineral content in biological materials [1].

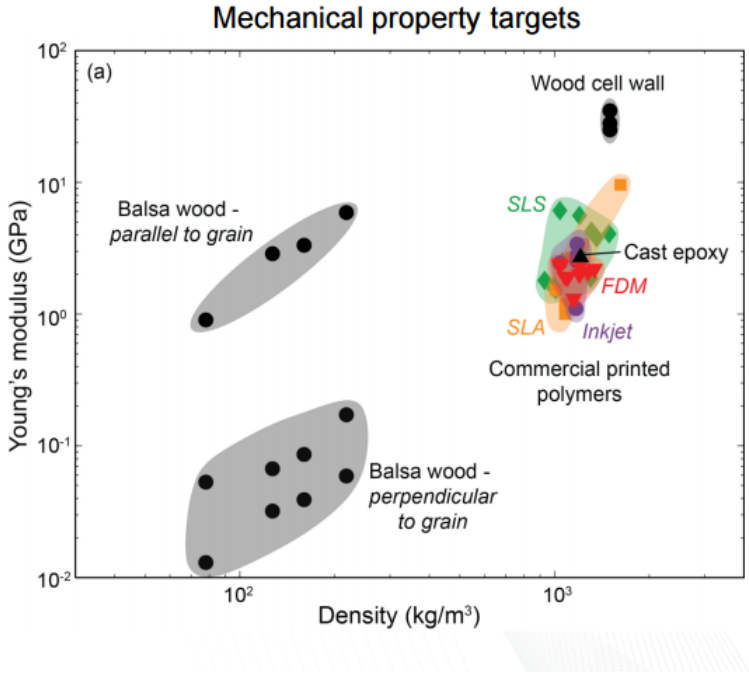

Figure 2.6: Ashby chart showing elastic modulus vs. density for various commercially available 3D-printed materials and natural materials [38] (used with permission).

Natural materials can exhibit many different functions such as providing stiffness, strength and toughness. They do so using a limited set of proteins, calcite and aragonites arranged in complex interwoven structures. Their outstanding efficiency is seen in their performance per unit mass. This, as already mentioned, can be easily depicted in Ashby's material properties charts [23].

Natural cellulose

Natural cellulose fibers are specifically interesting due to their environmentally and economically friendly production, compared to their synthetic counterparts. There are however weaknesses associated with cellulose fibers such as being sensitive to water and their lower thermal stability. All in all, the advantages of using natural cellulosic fibers outweigh the disadvantages. Furthermore, the increased environmental awareness also promotes the use of natural polymer based materials over synthetic ones [41]. Figure 2.7 shows a typical source of natural cellulose.

From a mechanical performance point of view, the individual building blocks do not consist of any particular features in and of themselves. Cellulose shows similar elastic modulus as that of a nylon fishing-line. In contrast hydroxyapatite has a fracture toughness comparable with man-made ceramics. This indicates that the hierarchical structure is responsible for making these natural materials so efficient [23]. This has further offered a path for material design, as nature has solved the challenge of combining both strong and tough materials [53].

Figure 2.7: Kapok seeds, a typical source of natural cellulose [9] (used with permission).

The natural polymer cellulose has the highest efficiency in tension, it exceeds that of steel by a factor of 2.6. Balsa wood is another natural material that when loaded parallel to its grain can show a resistance to buckling five times greater than that of normal steel [23]. Balsa wood even rivals the best engineering materials in terms of specific bending stiffness ($\frac{E^{1/2}}{\rho}$) and specific bending strength ($\frac{\sigma^{2/3}}{\rho}$). This is due to the composition and architecture controlled over multiple length scales [38]. This is not surprising as their environmental conditions such as wind and snow cause huge principal loads. Bamboo wood is even more efficient due to its fibers being oriented along the stem in a very fine arrangement. The plant's efficiency is increased even further by its tubular shape causing a high moment of inertia and a gradient of modulus throughout the wall thickness, this will be discussed further in terms of impact absorption [23]. Similarly sections through plant stems or stalks such as those of sedge plants exhibit forms that resembles an architectural I-beam, they are therefore usually described as "biological I-beams". Again, they exhibit a high area moment of inertia and are therefore very well suited for bend- and torsion-applications [25].

Bone, antler, enamel and dentine are all made up of hydroxyapatite, calcite or argonite in a matrix of collagen, their density ranges between 1.8 and 3.0 Mgm^{-3}. Natural polymers and polymer composites including protein, collagen, chitin and keratin all have densities around 1.2 Mgm^{-3} but their tensile strengths are larger that of normal engineering polymers. Cellulose fibrils have an elastic moduli between 50–130 GPa and a strength of 1 GPa. Comparing this to man-made polymers, only Kevlar fiber has a higher stiffness and strength: 200 GPa and 4 GPa respectively. This is achieved through covalent bonds and highly structured and oriented molecular structures [23].

2.3 Impact resistant/absorbent bio-composite architectures

The most common impact resistant structures found in nature consists of a hard outer shell distributing the impact but also retaining the strength and flexibility [53], much like the one found in a helmet, with a soft and porous core for absorbing the impact energy. As the porosity ranges from being lowest at the surface and increasing farther into the material an inverse relation to the elastic modulus exists [1]. This structure is for example found in the toucan's beak [11], mammalian cortical bone [29] and teeth [4] as well as the armor of the armadillo [3] to name a few. There is also a twisted plywood formation found in for example the stomatopod dactyl club [5] or the exoskeleton of crab and American lobster Homarus americanus [21]. Here we will look closer into the bone and teeth structure as well as the Bouligand structure. As the bones and teeth are two of the most common structures found in nature, these will be the two looked into closer below.

2.3.1 Bone and tooth structure

Bones consist of proteins and minerals. About 60 % of the weight is mineral closely resembling calcium and phosphate [27]. The remaining percentage consists of water and a soft-matrix. Roughly 90 % of the soft-matrix is collagen which is a strong material that forms bone, cartilage and tendons. During the natural manufacturing process the collagen is formed into chains twisting into triple helixes. These are bonded together into fibrils and then arranged in layers. Lastly mineral crystals, also known as hydroxyapatite, are deposited between the layers. The mechanical properties of bone can basically be compared to a fiber-reinforced composite, although certain care must be taken when considering failure behaviour due to its hierarchical structure as the failure can occur at any of these levels. In general, the main function of the bone in our body is to provide stiffness [4].

Categories of bones

Bones can be divided into two main categories: cancellous bone and compact bone. In comparison, the porous structure of cancellous bone is much weaker and less stiff than compact bone. It turns out that cancellous bones can be re-shaped and differ majorly in mechanical properties from compact bone [27][4].

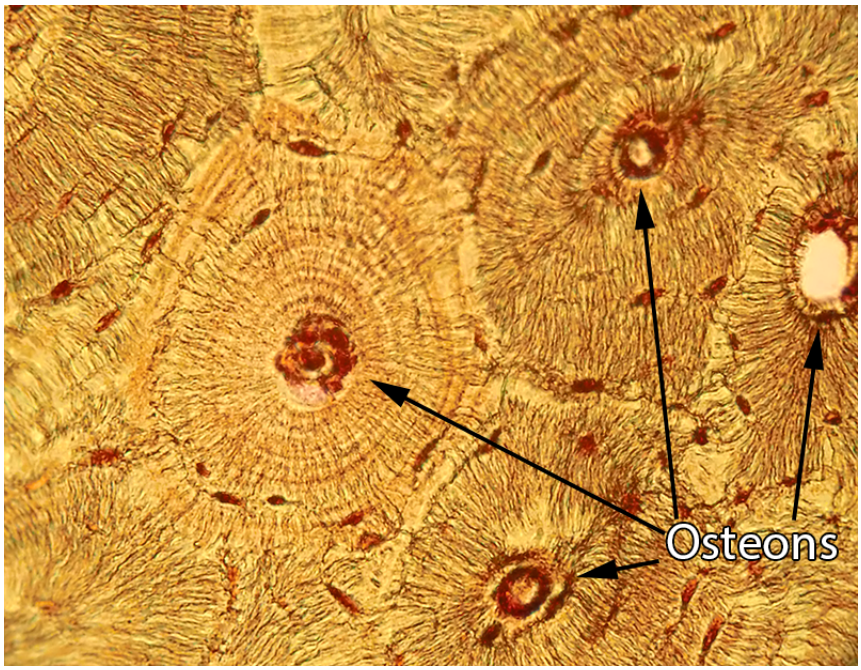

Figure 2.8: Compact bone structure of a human bone [20] (used with permission).

Teeth in mammals consist of three main components: enamel, dentin and cementum. The function of the enamel is to provide the hard outer shell made for crushing food. Enamel is about 97 % mineral with a defined crystal structure. Dentin is the major constituent and very much resembles compact bone. The cement works as the link between the collagen fibers that connects to the bone. The main difference compared to bone is that the dentin cannot be remodelled once laid down, whereas the bone has the possibility to do so [4].

2.3.1.1 Hierarchical architecture

The nano-structure of bones and teeth consist of plate-like mineral crystals - hydroxyapatite (HAp) embedded in a collagen-rich protein soft-matrix with the size ranging between 2 and 4 nm thick and 100 nm long. The volume ratio between the mineral to soft-matrix can be of the order up to 2. Figure 2.9 shows the staggered mineral crystal plates in a soft-matrix for a typical bone structure [16].

One suggestion why nature uses nano-sized structures comes from the fact that nano-size makes mineral crystals insensitive to crack-like flaws, where normally these minerals would show a brittle material behaviour. The nano-size combined with the exceptional energy absorbing capabilities of the soft-matrix gives a robust natural bio-composite [16].

Put in contrast, most engineering materials have been developed through the formulation and synthesis of new compounds with structural control acting primarily on the micrometer scale. Utilizing nanotechnology, possibilities of mimicking nature's structure at this level might be the way forward in perfecting biomimicry [53].

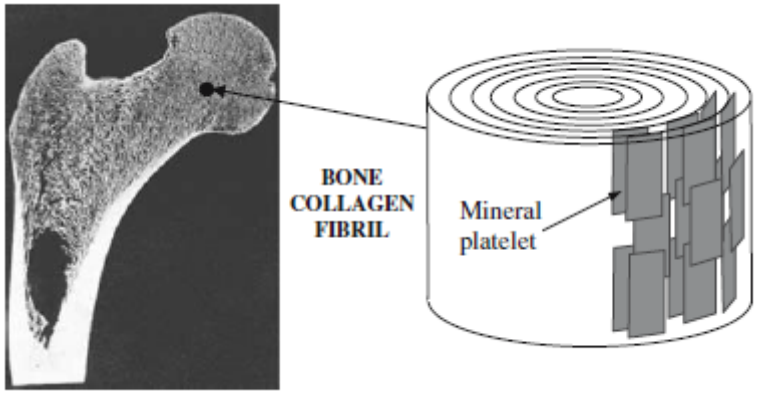

Figure 2.9: Nanostructure of bone consisting of plate-like mineral crystal platelets embedded in a soft protein-rich collagen matrix [36] (used with permission).

2.3.1.2 Mechanical behaviour

The soft-matrix in bones constitutes a high volume fraction phase, roughly 60 % and can usually be several magnitudes softer than the mineral crystals. The question of how nature can still create a stiff composite despite this dominating soft-matrix can be answered through a simple scaling law composed by H. Gao [16]. Assuming linear elasticity in the soft-matrix and moderately sized aspect ratios:

$$E \propto G\rho_{ratio}^2$$

where ($\rho_{ratio} = \frac{L}{h}$) is the aspect ratio of the mineral crystals, E is the composite's stiffness and G is the shear modulus of the soft-matrix. This relation shows that despite the high volume fraction of soft-matrix, the bio-composite can achieve additional stiffness through increasing the aspect ratio, i.e. the stiffness stems from the large aspect ratios of the mineral crystals and thus compensates for the energy absorbing soft matrix [16]. The defined dimensions for the staggered hard mineral platelets can be seen in Figure 2.10 below.

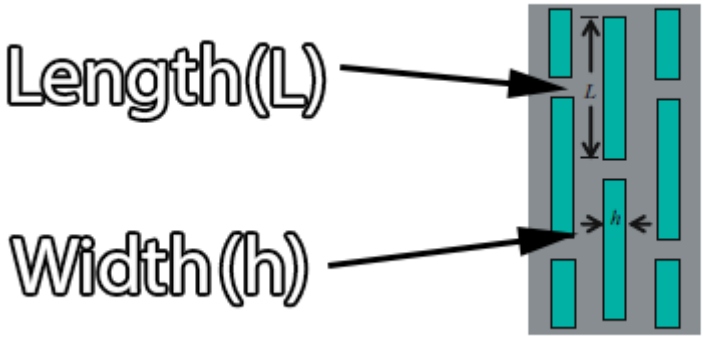

Figure 2.10: Principal sketch of the staggered hard plates (turquoise) embedded in a soft-matrix (grey) found in bones [37] (used with permission).

The elastic modulus is greatly affected by the mineral content and porosity of bones and the ultimate tensile strength (UTS) is related to the mineral volume fraction, i.e. the higher the mineral content the lower the strain [4]. One important characteristic is the effect of hydration. Bones show a higher elastic modulus and yield strength in dry conditions. Water is believed to promote more deformation of the collagen [1]. Furthermore, the high porosity comes usually at the expense of mechanical stability [53].

The staggered alignment of the mineral crystals and aspect ratios of the aforementioned mineral crystals has been discussed regarding their role in the stiffness of the composite. However, a stiff structure is usually brittle with a relatively low toughness. Therefore nature uses hierarchical structures to increase the toughness while still maintaining its stiffness. This causes the soft-matrix to undergo large deformations through strain amplification mechanisms at the microstructural level, allowing the soft-matrix to fully deform and dissipate energy, while the composite itself only deforms at very small strains on the composite level. However as already mentioned this requires that the mineral crystals be designed in the nano-meter scale to prevent a brittle fracture of the crystals [16].

The synergy properties between the soft-matrix and the HAp found in bones was studied by Katti et al. [32] where the mechanical behaviour of models was investigated with the presence and absence of HAp in a collagen matrix and showed that approximately five times more energy is expended in the presence of HAP. This is highly relevant from the perspective of energy absorption, yet proving that the bone-structure is well suited for impact absorbing applications [32]. McKittrick et al. found that the Hashin-Shtrikman model produces the closest fit for the elastic modulus as a function of mineral content [1].

2.3.1.3 Deformation and toughening mechanisms

At sub-micrometer scales, the motions of the mineralized collagen fibrils are the origin of post-yield or permanent deformation in bones. This is resisted primarily by non-collagenous proteins in an aqueous environment [30].

At the level of individual mineralized collagen fibrils the slip-mechanisms are important for energy dissipation of cracks. The slipping leads to the formation of a plastic zone where the elastic energy can be dissipated and thus hinder further spreading of cracks. As loads are applied to the structure, it is carried as tension in the mineral platelets and transferred between the platelets via shearing of the soft-matrix. The interface, intermolecular cross-linking and sacrificial bonds all play an important role for promoting fibrillar sliding efficiently. This turns out to be the dominant toughening mechanisms also found in ductile materials such as nickel and copper [30][53].

It has thus been proposed that collagen fibrils that span between crack surfaces could increase the bone's toughness to fracture. Fibrils spanning over micro-cracks therefore exert a crack closure mechanism much like fiber reinforcement in composites [31].

Deformation mechanisms appearing in bone were shown successful in both computational and physical testing mimicking the bone structure performed by Dimas et al. [35].

At micrometer level the toughness of bones are related to the "recoverable"-bonds, also known as sacrificial-bonds. Individual mineralized collagen fibrils can be considered to be glued together by such bonds [30].

For other bio-mineral systems these sacrificial bonds have been shown to contribute to a thousand-fold increase in fracture toughness of the composite compared to the mineral alone. When strain on the bone is removed, these sacrificial bonds can reform and thus provide a mechanism for repeatable energy dissipation of cracks. This is a remarkable feature of bones usually termed as "self-healing" [31]. This of course poses an even greater challenge for mimicking natural structures [53].

Finally it can be concluded that bone derives its resistance to fracture through deformation and toughening mechanisms operating at many size scales, ranging from nanoscale all the way to macroscopic physiological scale [53].

2.3.2 Bouligand structure - twisted plywood

Arthropods are animals characterized by their exoskeleton. Simply put, the bones make up the outer layer of their body. The exoskeleton mainly consist of chitin, a hard fibrous chitin–protein tissue containing a large amount of calcium carbonate minerals (usually crystalline or amorphous calcite [22]), and its mechanical rigidity comes from the high degree of mineralization [21]. The exoskeleton layer can be divided into three regions: epicuticle, exocuticle and endocuticle where the two latter are the main structural parts that handle mechanical loads.

The exoskeletons' unique feature is their well-defined hierarchical organization with several structural levels resembling plywood. The plywood is stacked in a twisted helicoidal structure made up of bundles of fibers stacked in planes that consist of fibrils wrapped in protein. The twisted plywood structure is called Bouligand structure and can also be found in collagen networks in bones [21]. This structure is able to dissipate large amount of viscoelastic energy during deformation, much like a shock-absorber [1]. In the case for exoskeletons the minerals are in the form of calcite or amorphous calcium carbonate within a chitin-protein matrix. Figure 2.11 shows the Bouligand structure found in e.g. crabs.

The twisted plywood structure is also suggested to be the mechanism on how nature has developed a strong and tough material, using otherwise relatively weak units: chitin and proteins [21]. Most fish scales (skin) exhibit a conventional plywood structure, layers in orthogonal orders. But fibers in all kinds of arrangements exists ranging from strictly orthogonal- to helicoidal- and even more seemingly random orientations. The precise mechanical property difference is not known, but nature clearly shows that any sort of plywood formation is yielding a more isotropic mechanical behaviour of the material [4].

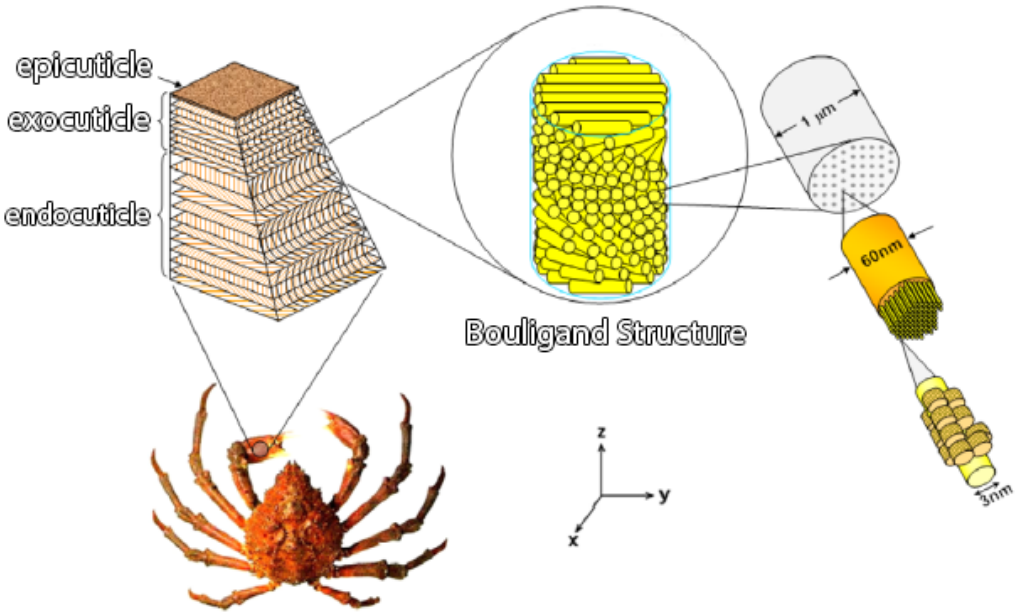

Figure 2.11: Exoskeleton composition of a crab showing the Bouligand (twisted plywood) structure [21] (used with permission).

Further investigation into the Bouligand structure by Raabe et al. [22] revealed that the planes found in the twisted plywood formation form planar honeycombs with fibers connected in an hexagonal array [22]. Honeycomb structure has its name from the structure used by honeybees, geometrically speaking, a rhombus-shaped lattice structure [25] which will be discussed more regarding its use in impact resistant applications in section 2.9.

Chen et al. [21] performed analysis to reveal a gradient structure in the twisted plywood structure between its outer and inner layer. The hardness values were found to be twice as large for the outer layer compared to the inner layer. Such design can be found in many places in nature as already mentioned in e.g. teeth, with its harder outer enamel covering an internal dentine. This is also found in the Dactyl club (a hypermineralized hammer-like club of a highly aggressive marine crustacean) which has a gradient structure with thinner and thinner packing of laminates farther into the club, which renders incoming shocks harmless to the performance of the club [21][5].

Although attempts have been made to explore both the topographical, compositional and structural gradient on the mechanical properties in man-made materials, we have yet to match the structural complexity of materials found in nature [53].

2.4 Additive Manufacturing (AM)/ 3D-printing

Additive manufacturing, also known as 3D-printing, represents one of the most effective and easiest ways to manufacture customized parts with significant complexity. This explains its potential use in industry, academia as well as personal use [29]. Currently various techniques for additive manufacturing include for example:

- Fused Deposition Modeling (FDM)
- Selective Laser Sintering (SLS)
- Examples of methods utilizing light as curing:
  - Stereolithography (SL)
  - Continuous Liquid Interface Production (CLIP)
  - Digital Light Processing (DLP)

Although FDM has become the most widely used method due to its simplicity, low cost and environmentally friendly features [40]. The materials available for additive manufacturing are currently very limited and specific to each process [45].

Randomized fiber is the standard for systems without any control. One of the greatest challenges of additive manufacturing technology is to orient discontinuous fibre-reinforced composites. Fibers aligned parallel to the predominant stress reinforces the entire composites while orthogonally oriented fibers weakens the matrix. The randomized orientation performs between these two extremes and affects the composite strength whilst drastically reduces the ductility [29].

To enhance the mechanical properties of 3D-printed parts, fiber-reinforcements are used in composites. However, the addition of fibers may result in composites being more susceptible to fracture during extrusion. Therefore special additives may be necessary to ensure continuous and homogeneous filaments such as plasticizers. Research performed by Weng et al. [40] showed improved mechanical properties along with increased heat distortion temperature and thermal stability of the polymer-matrix by the addition of polymer/layered silicate (PLS) nano-composites [40][33].

2.5 Fused Deposition Modeling (FDM)

FDM is a type of additive manufacturing (3D-printing) process commonly used for modeling, prototypes and production applications. It is a fast growing rapid prototyping (RP) technology with the ability to build functional parts with relative complex geometrical shapes in an acceptable time period [34]. FDM is most commonly used for polymers. Figure 2.12 shows the FDM process.

However, the current limits of FDM include that the mechanical strength of the produced parts is usually worse when compared to injection moulding due to the weakness in the interfaces between the individual fiber layers. An additional weakness is the warping (shrinkage) happening during the cooling process [40].

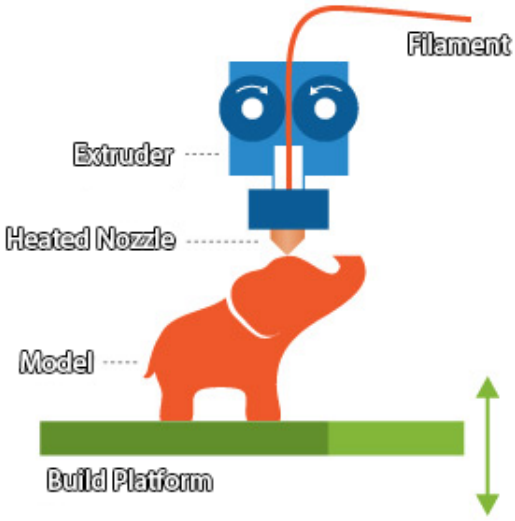

Figure 2.12: Typical Fused Deposition Modeling (FDM) process [10] (used with permission).

The 3D-printer gantry is basically a computer numerically controlled (CNC) machine equipped with two or more extruder-head nozzles, one for the modeling material itself and the other for support material to be deposited around the part, although there are cases when the same material is used for both support and deposition. In the FDM process, parts are produced by extruding molten "beads" of usually thermoplastic polymers through a heated nozzle in an already prescribed pattern, layer-by-layer hence the name additive manufacturing. After the semi-molten material is deposited onto a worktable it fuses together with adjacent filament material.

FDM prototypes are governed by its structure at the extruded filament scale which is determined by the manufacturing parameters. By tailoring these parameters the FDM process can produce prototypes with desired properties, some of which include width of the filament, layer thickness, deposition orientation and gap size between filaments. Li et al. [33] argues that the most important parameters to control the mechanical properties include the direction of layers and gap sizes between the individual deposited filaments [33].

2.5.1 Material filaments used in FDM

The FDM process uses several types of commercially available materials [33] such as:

- Acrylonitrile-butadiene-styrene (ABS) - $(C_8H_8{\cdot}C_4H_6{\cdot}C_3H_3N)_n$
- Polyactic acid (PLA) - $(C_3H_4O_2)_n$
- Nylon 6 (PA) - $(C_6H_{11}NO)_n$
- Polyurethane (PU) - $(C_{27}H_36N_2O_{10})$
- Thermoplastic elastomers (TPE)

2.5.1.1 Acrylonitrile-Butadiene-Styrene (ABS)

ABS is by far the most common printer filament material, it is a hard and durable plastic that stays strong at higher temperatures. However, the downside is that ABS requires a heat bed because the material tends to warp during cooling [49]. It also requires ventilation during printing due to toxic fumes. ABS is commonly used as the outer harder shell of helmets today. with an elastic modulus (E) of 2 495 MPa, shear modulus (G) of 950 MPa and density (ρ) of 1 151 kgm^{-3} [54]. The filament used in this study was manufactured by Innofil3D and can be seen in Figure 2.13.

Figure 2.13: ABS 3D-printer spool by Innofil3D.

2.5.1.2 Polylactic Acid (PLA)

ABS has previously been the go-to material in industrial applications and personal desktop printers but more and more consumers are now gradually shifting towards using PLA [79]. The advantage with PLA over ABS is that it's eco-friendly and bio-degradable and does not require any ventilation. Additional benefits include reduced smell and lower shrinkage during cooling. However, there are disadvantages such as warpage commonly seen in corners. PLA is also showing a weaker temperature resistance which may result in deformation during usage [47]. PLA does not require a heated bed due to its relatively low extruding temperature, 210 °C [49]. The tensile strength (σ_y) of PLA ranges from 2.7 to 16 GPa [50]. Commercially available PLA is commonly known as having a lower strength than ABS which can be seen as a disadvantage. The PLA filament used in this study was manufactured by Primaselect and can be seen in Figure 2.14.

Figure 2.14: PLA 3D-printer spool by Primaselect.

2.5.1.3 Nylon (Polyamide 6)

Nylon is a very versatile material that can exhibit a broad range of stiffness. However, certain care needs to be taken with the printing of nylon due to its weakness caused by fiber orientation. Nylon 618 and 645 are two available formulations where the numbers refer to the molecular structure [49]. Nylon is a semicrystalline thermoplastic with unique properties due to its shape and hydrogen bonds [14]. 3D-printing nylon further requires a high-temperature nozzle, but does not require a heated bed [49].

2.5.1.4 Thermoplastic Elastomers (TPE)

Elastomers are a combination between thermoplastics and rubber. Parts made out of TPEs are strong and flexible. However, a disadvantage is the slow printing speed needed to avoid overstretching of the filament during printing [49]. Thermoplastic polyurethane (TPU) is known for having excellent impact properties thus making them a perfect candidate in energy absorbing structures. TPUs can be processed in the same manner as traditional thermoplastics and therefore printed using SLS or FDM [45].

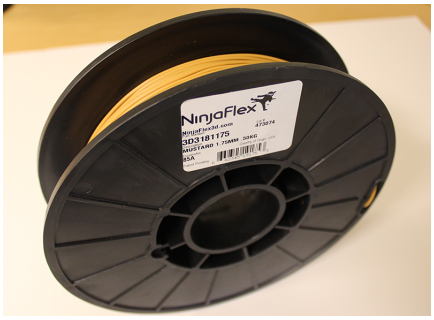

Figure 2.15: TPU (NinjaFlex) 3D-printer spool by NinjaTek.

An example of a TPU that is now available commercially is NinjaFlex, see Figure 2.15. The material offers excellent flexing abilities previously only achievable in high-end equipment. Examples of applications for the filament include prosthetics and protective cases for smartphones [81][82].

2.6 Stereolitography (SL)

SL uses ultraviolet light to polymerize and cure a photosensitive liquid resin. The technique cures a predetermined section with ultraviolet light. This is repeated layer-by-layer until the part is created. SL has a high accuracy and creates good surface quality [7].

2.6.1 Materials used in SL

SL mainly uses plastic materials that can exhibit the characteristics of for example ABS and PP. The technique also allows for combined processes to produce new products in materials such as glass, ceramics and metals [15].

2.7 Selective Laser Sintering (SLS)

SLS uses a reflected laser to selectively fuse powdered materials together. The part is supported by the surrounding un-sintered powder as the part is being built, this is later removed, e.g. with compressive air or in a water bath.. This support mechanism is also advantageous to lattice type structures, due to other additive manufacturing processes requiring support structures to be built along the part during manufacturing. This would result in a both time-consuming and difficult process when removing the support from the lattice structure [44][7].

2.7.1 Materials used in SLS

Typical materials used in SLS technology include photopolymer resins and TPE [44]. The material Duraform® Flex, a type of TPE was shown in testing performed by Soe et al. [54] to be reducing the peak acceleration and increasing the pulse duration in liners used for bicycle helmets.

2.8 Additive manufacturing for impact absorbing architectures

Additive manufacturing (AM) allows for more complex design and therefore cellular structures allowing tailored dissipation of energy can be built. These repeating structures are shown to be potentially effective in impact attenuation. The cellular structures in honeycomb architecture formations can be used in foams and thus provide an effective ability to dissipate energy [54].

Honeycomb structures have been thoroughly investigated for their use in energy absorption applications, as mentioned in Gibson and Ashby's famous book on cellular solids [26]. More recent studies include cellular structures in bicycle helmet applications by Soe et al. [54] and honeycombs for repeated tailored energy absorption by Bates et al. [45].

As already mentioned, traditional manufacturing methods greatly limit the complexity of repeating lattices and their energy absorbing capabilities. Additive manufacturing of lattice structures thus provides a geometrical design freedom that cannot be achieved in conventional manufacturing as of today [45].

The rising popularity of additive manufacturing has further allowed the possibility of creating honeycombs with multi-material structures. Along with structural hierarchy and gradient density, additive manufacturing allows tailoring of energy absorbing honeycombs [45]. Studies performed by Bates et al. [45] not only showed that honeycomb structures used in energy absorption applications are possible with additive manufacturing, the research further showed that the energy absorption behaviour of honeycomb structures are dependent on the strain rate and cell orientation with respect to the compressive direction [45].

2.9 Materials and methods for energy absorbing architectures

Bio-inspired materials are usually hybrids that combine two dissimilar materials e.g. a polymer and a ceramic, which may be difficult to process using only a single technique. Below we take a look at different attempts at mimicking the structures found in nature using single techniques. Additive manufacturing with its possibility to integrate new functions and produce complex structures looks very promising for producing bio-inspired structural materials in the future. However, further research is needed in terms of controlling the surface quality and micro-structure of layers which drastically decreases the mechanical properties of the finished part [53].

Brennan-Craddock et al. [44] suggest using SLS for producing lattice structures used in impact absorbing structures. This is with consideration of the current relative strength and range of commercially available polymers. However, SLS does not allow for open-cell form as the powder would become trapped within the cells and thus rendering it impossible to remove in post-processing [45]. Furthermore, FDM allows for printing of multiple materials, which would be highly suitable for varying the stiffness within cellular structures thus allowing structural tailoring [45].

Hierarchical structures in additive manufacturing

Using the hierarchical structure found in nature Dimas et al. demonstrated the composites can be made so strong that it does not fail at the interfaces, which is usually the weakest part of a composite. They also showed that the stiffness ratio in a two-phased composite plays an important role regarding the distribution of stress and strain prior to initial crack propagation [35].

Furthermore, an appropriate stiffness ratio can even alleviate stress concentrations in specimens to reduce the tendency of composites failing in a brittle manner. Finally, the experiments by Dimas et al. shows that a system can achieve a toughness modulus up to 20 times larger than its constituents [35].

Lightweight cellular composites

An emerging class of high-performance materials finding applications in absorbing energy are lightweight cellular composites composed of an interconnected network of solid struts that form the edges or faces of cells. Using an epoxy-based ink with a controlled alignment of fiber reinforcement inspired by balsa wood, Compton et al. [38] was able to produce cellular composites. These materials exhibit elastic modulus values that are an order of magnitude higher than those obtained by thermoplastics and photo-curable resins used in commercially available 3D-printers. Yet these composites retain a comparable high strength. Normally inks undergo solidification using an on-the-fly polymerization by UV-light although the epoxy resin by Compton et al. solidify during ambient conditions. An additional thermal curing at 100–220 °C is however required to complete the polymerization process [38].

3

Methodology

3.1 Overview

Within the course of this study, a work with familiarization of the geometry of various impact- and crushing-absorbent bio-composites found in nature has been carried out. Nature solves these geometrical and material problems by utilizing different length scales as well as hierarchical structures, while still only using a limited amount of building materials yet still efficiently absorbing impacts and compressive loads [25][53].

Through an iterative process in a parallel project (virtual testing using impact and compressive/crushing loading conditions) biomimetic architectures were optimized whilst taking into consideration the technical and practical constraints of the current 3D-printers available today. The parallel project title is *"Design optimisation for 3D-printed impact resistant architectures inspired by nature"* [51] by Mattias Naarttijärvi and Alexander Olsson in the Applied Mechanics Department at Chalmers.

The optimized structures from the parallel project [51] were printed using the suitable material and optimized process parameters. They will serve as a demonstrator and achievement of the current study.

Biomimetics can usually be divided into two categories: the material and the architecture. Due to the commercially available additive manufacturing technologies and limited bio-inspired filament materials, the architecture, material characterization and processing were the main considerations when performing the experiments described in the Results & Discussion (see section 4).

The bio-materials and bio-ink are today still very expensive and hard to process and still only available for research purposes. The magnetic 3D printer method proposed by Martin et al. [29] to align fibers magnetically is today in its early stages of production and has a limited printing speed and size but has a very bright future. 3D-printing of thermosetting polymers today is not very common and also very difficult, as seen in studies performed by Compton et al. [38]. Although difficult processing, it is worth mentioning the possibility of manufacturing complex structures with the only current alternative being manufacture by hand [39].

As mentioned in the background, see section 2.4, SLS and FDM have been used with success to produce foam like structures for impact absorbing applications [45][44]. SL is a very expensive method and not currently available at SICOMP. Therefore FDM will be the choice of method for the Results & Discussion (see section 4).

SICOMP has the possibility to print FDM parts using a MakerBot Replicator 2 with interchangeable filaments and nylon with a Markforged Mark One. This study will only focus on the following thermoplastics: PLA, ABS, nylon and TPU. General properties in the impact absorption capabilities are described below.

- The ABS is usually injection molded and shows a promising impact resistance and toughness, however this is slightly reduced for 3D-printed ABS [73].
- 3D-printed filament shows a higher toughness than injection molded one, in a study performed by Song et al. [74], the reason being due to the filament layered nature of the 3D-printed material and the complexity that this induces in the microscopic mechanisms of fracture.
- Nylon 6 (PA6) exhibits high toughness and rigidity [75]. Stratasys has produced a FDM nylon 12^{TM} (PA12) which has particularly high impact strength and resistance to fracture [72].
- TPU possesses excellent performance in toughness properties and bio compatibility. TPU has been used as a toughening agent to improve the impact strength of composites and even polyamide (PA) [77].

The experimental part will use a lattice structure to represent the liner part of the helmet as this is today the most suitable part of the helmet to utilize additive manufacturing (AM) on. The gradient density possibility with AM is the major advantage for the liner of the helmet.

3.2 Limitations

This study did not look into the optimization of the structure, which was carried out by a parallel thesis project performed by the Department of Applied Mechanics [51]. Through discussion and based on material characterization carried out in the Results & Discussion (see section 4), the optimal structure was then printed and tested for energy absorption during impact.

The FDM-printers did not allow for adjusting the filament orientations, see section 3.4.2. The adjustable process parameters are discussed and reviewed in-depth in section 3.4.1.

The limited amount of controllable parameters constrains the characterization and understanding of this study on AM technology. Therefore SICOMP is moving towards using a 3D printing gantry, thus allowing complete control of parameters which are not adjustable in commercially available printers today.

3.3 Selection of filament materials

As previously mentioned and based on current equipment at SICOMP, FDM will be used as the AM technology to print the biomimetic-structures, see section 3.1. For the FDM technique, a wide choice of commercially available filaments was presented, therefore a review on materials to find the ones with superior mechanical and processability qualities were the main interests. Based on a comparable study between filaments performed by Filaween [55], the material selection spectrum was reduced considerably. Table 3.1 shows the choice of materials used for this material characterization. Filaween's findings are aimed to guide users to correctly find the filament of choice for their particular purpose and also provide recommended printing parameters. Here, the interest were the filament quality, strength and recommended printing parameters.

Table 3.1: Filaments based on printing quality and strength based on Filaween's findings [55].

Materials (Thermoplastics)	**Choice (Manufacturer)**	**Quality**	**Strength (kg)**	**URL (Manufacturer website)**
ABS	Innofil3D	14/20	22.5	`https://goo.gl/xCVjny`
PLA	Primaselect	17/20	48	`https://goo.gl/IfZAQO`
PU (NinjaFlex)	NinjaTek	-[1]	-[1]	`https://goo.gl/xdiRFi`
Nylon	MarkForged	-[1]	-[1]	`https://goo.gl/OJqBes`

3.4 3D-printers

The 3D-printer used to print parts in PLA and TPU was a MakerBot Replicator 2 [61]. For the ABS, the MakerBot Replicator 2x [62] with fume-hood will be used due to ABS's ultra-fine particle emission and emission of gas-phase pollutants during printing [66].

The technology of the MakerBot printers was Fused Filament fabrication (FDM). The MakerBot uses the software *MakerBot MakerWare* which supports stl, obj and thing file-formats for printing. Slicing of the models i.e. instructions for the printer is programmed with either x3g or G-Code [61]. The MakerWare workspace can be seen in Figure 3.1 also note the enclosed volume showing the available workspace.

[1]No information on properties covered in Filaween's findings.

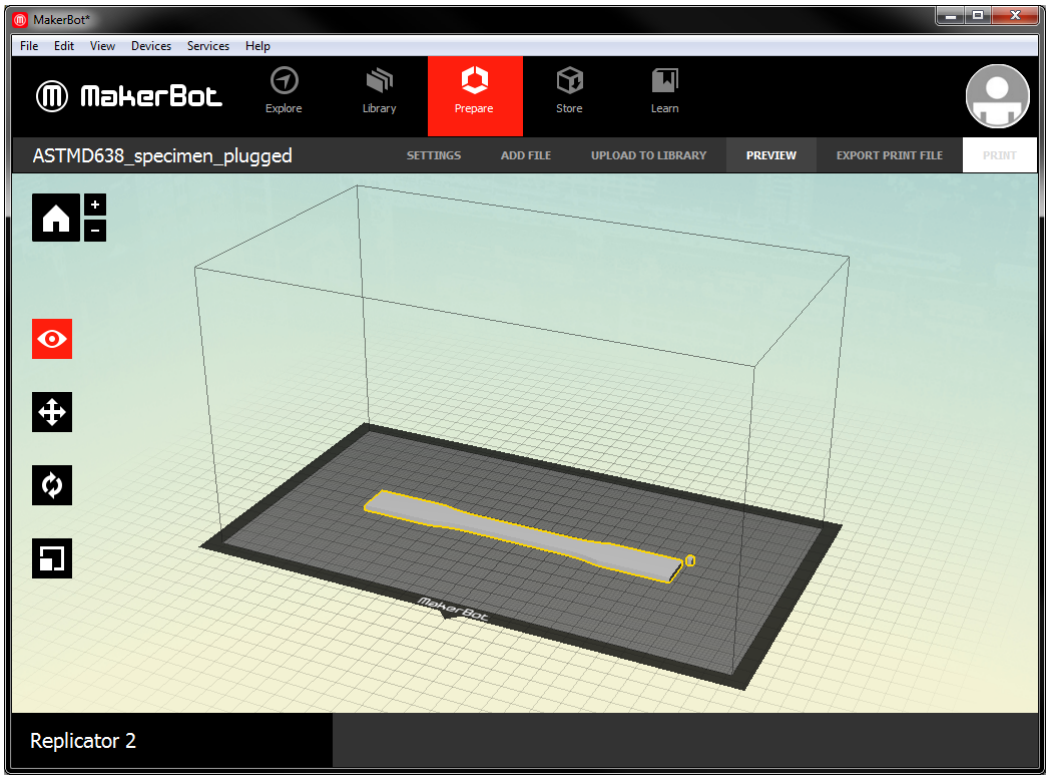

Figure 3.1: Tensile test specimen following the ASTM D638 standard [56] highlighted in yellow in MakerBot's MakerWare program.

3.4.1 3D-printing parameters

Parameters configured in both Replicator 2 and 2x were the following:

- *Infill density* can be set between 1–100 % where 100 % is a pure solid. For the reference tensile test and DMTA specimens in this study a 100 % infill was used. This is to correctly comply with the standard of the tensile and DMTA testings. The infill density percentage for the prints can be determined, however the "gaps" caused between the layers due to the choice of infill cannot. This consequently leads to varied density values between printers [60].
- *Layer thickness* adjusts the quality of prints. A higher value would result in less layers whereas a lower value would yield a coarser printed structure. For the reference tensile test and DMTA specimens, a layer thickness of 0.2 mm was used. Beyond this layer thickness, the maximum stress is fairly constant for PLA based on studies performed by 3D Matter [78]. The same results can be found for ABS in studies performed by Rankouhi et al. where the thickness was shown to provide the highest elastic modulus and tensile strength [83].
- The outer surface of a part is called *shell*. Each layer of the shell is called a perimeter. Additional perimeters result in a stronger object but an increased printing time [65][79]. Typically this number is set to 2 but for the specimens used in this study this parameter was set to 3.

The influence of this parameter is highly dependent on the geometry and dimension of the part, although according to EngineerDog's findings the optimal number is 3 for ABS. Thereafter the yield stress per unit weight then diminishes [80].

- *Infill pattern* is determining how the inner non-visible support structure should be patterned. The MakerBot MakerWare 3.10.0.1364 allows for six different support structures including hexagonal, linear, diamond, catfill, sharkfill and moroccanstar.
  - *Hexagonal* allows for strong and sturdy objects yet saving weight.
  - *Linear* is made up of straight parallel lines and thus provides an easy path for the printing nozzle.
  - *Diamond* is a rather new pattern which promises a strong structure with a fast print. The current version 3.10.0.1364 also provides a *diamond (fast)* which claims to print even faster with only slight compromise of the sturdiness.
  - The *catfill*, *sharkfill* and *moroccanstar* are only for aesthetic value at exposed parts [65] and were therefore not included in this study.

3.4.2 3D-printing software

The settings were adjusted in the MakerWare program prior to printing. A comparable study between the different materials with the same parameters used was thus conducted. 3D-printed tensile test specimens after ASTM D638 standard [56] and DMTA specimens according to ASTM D7028 standard [86] were used as references with a 100 % infill and linear infill pattern.

The MakerWare as of version 3.10.0.1364 [61] provides no choice of adjusting the angle of the filaments for the printing pattern of the parts. This was further investigated by orienting the test specimen in a -45°, 0° and +45° degree angle in the build platform, shown in Figure 3.1 of the MakerWare software and still yielded the same orientation of the filaments regardless of specimen orientation in the build platform, see Figure 3.1.

The standard printing speeds in MakerWare were used:

- *First Layer* determines the speed of the first layer: 30 mm/s.
- *Outline*, the outermost layer of the shell (see section 3.4.1): 30 mm/s.
- *Infill*: 90 mm/s.
- *Inset*, all shells except for the outermost one on each layer: 90 mm/s.

Upon adjusting the infill pattern it was noted that the linear, hexagonal and diamond patterns all resulted in layers positioned in an alternating [-45°/45°] angle plywood formation with an infill set to 100 %. Therefore, the infill pattern was eliminated as a parameter for the reference specimens of all materials. This is understood by the 100 % infill results in a complete solid and thus independent on the set infill pattern.

3.5 3D-printer settings & preparations

Table 3.2: Nozzle- and printer bed temperatures used for the 3D-printing filaments.

Materials	Nozzle temperature [°C]	Printer bed temperature [°C]
ABS (Innofil3D)	235[1]	100[1]
PLA (Primaselect)	215[1]	N/A[3]
PU (NinjaFlex)	210[2]	N/A[3]
Nylon (Markforged)[2]	260	N/A[3]

3.5.1 MakerBot Replicator 2

The build platform was cleaned using water and isopropanol [$CH(CH_3)_2OH$] to remove any grease and dust. After drying the platform, a thin coating layer of hairspray is applied to the platform. The hairspray contains vinyl-neodecanoate-copolymers and acrylates copolymers which is believed to be the reason for achieving a smoother and stickier platform and also help the adhesion between the glass build-platform and the thermoplastic with the use of the copolymer's reactive chain-groups which create hydrogen bonds.

3.5.2 MakerBot Replicator 2x

The printing of ABS was performed on a heated bed with a temperature of 100 °C, see Table 3.2 for more details on printing temperatures. The Replicator 2x was equipped with dual nozzles, which allows for multi-material deposition. The build platform was covered with a kapton tape for better adhesion of the first layer of ABS to the heated build platform.

3.5.3 Markforged Mark One

The nylon was printed in a Markforged Mark One printer at Swerea SICOMP in Piteå. The technology is identical to FDM but rather called Continuous Filament Fabrication (CFF). The Mark One has a much higher precision and quality prints than desktop printers for home usage, see section 3.5.1 and 3.5.2. The following settings were used:

- Similar to the shell, the *Roof and Floor layers* determine the amount of perimeters in the z-direction. This was set to 4.
- *Wall Layers* was set to 2 and this parameter is identical to MakerBot MakerWare's *shell*.

[1]Based on findings by Filaween [55].
[2]Based on recommendations from manufacturer's datasheet.
[3]Not applicable, no printer bed used.

- *Infill density* was set to 100 % with a fill pattern of *rectangular fill*. The *layer height* was set to 0.1 mm. Additionally, the XY precision of the machine is 0.00625 mm.
- Supports were activated but no *brim*, an enclosing outer layer, or expanding of thin features were used.
- The printing bed was covered with a thin layer of Elmer's glue-stick to make the first printing layer adhere better to the bed.

3.6 Material testing methods

Below the testing methods that were performed for the material characterization in this study are described. These include tensile testing and DMTA to characterize the 3D-printer filaments.

3.6.1 Dynamic Mechanical Thermal Analysis (DMTA)

In dynamic mechanical thermal analysis (DMTA) the material is deformed sinusoidally, where the strain and the corresponding strain controlled stress is measured. The applied load is low so the material is assumed to exhibit linear viscoelastic properties [84]. Testing methods includes tensile, compressive and shearing. The strain applied to the material is determined by:

$$\epsilon = \epsilon_0 \sin(\omega t) \tag{3.1}$$

where the ϵ_0 is the amplitude and ω is the angular frequency. Because of the nature of the viscoelastic material, the stress response is not in phase with the strain. This shift is usually denoted δ (phase angle). The resulting stress will then be:

$$\sigma = \sigma_0 \sin(\omega t + \delta) \tag{3.2}$$

The assumption that the stress varies sinusoidally holds as long as the material is in the linearly viscoelastic region. The equation for sinusoidal stress can then be:

$$\sigma_0[\sin(\omega t)\sin(\delta) + \cos(\omega t)\sin(\delta)] \tag{3.3}$$

In equation (3.3) the stress is expressed in two terms and we can then define the elastic (3.4) and viscous (3.5) moduli respectively:

$$\text{E'} = \frac{\sigma_0}{\epsilon_0}\cos(\delta) \tag{3.4}$$

$$\text{E''} = \frac{\sigma_0}{\epsilon_0}\sin(\delta) \tag{3.5}$$

To fully represent the total dynamic modulus we also define the complex modulus E*:

$$\text{E}^* = \frac{\sigma(t)}{\epsilon(t)} = \frac{\sigma_0}{\epsilon_0}[\cos(\delta) + i\sin(\delta)] = \text{E'} + i\text{E''} \tag{3.6}$$

The elastic modulus can be thought of as the storage modulus (E') whilst the viscoelastic modulus can be thought as the loss modulus (E"). In order to determine a material's energy absorption a loss tangent can be defined as:

$$\tan(\delta) = \frac{E"}{E'} \tag{3.7}$$

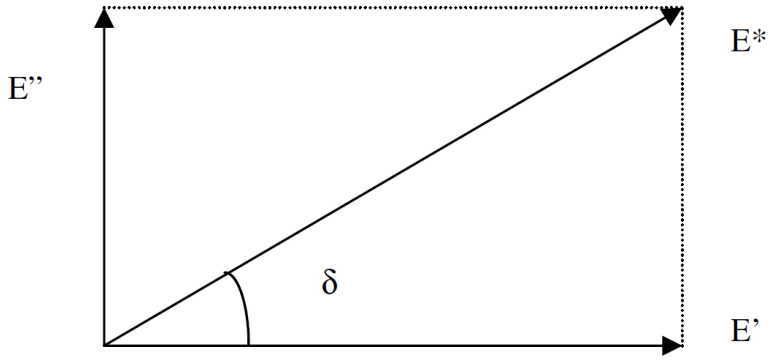

Figure 3.2: Relation between storage (E')/loss (E")/complex modulus (E*) viewed in the complex plane [84].

The relation between E', E" and tan(δ) is geometrically represented in Figure 3.2 on the complex numbers plane. Using complex numbers allows us to fully describe the loss and stored energy [84].

3.6.1.1 DMTA for characterization of polymers

For a purely elastic material, the tan(δ) would be zero. In the case of polymers, the tan(δ) is relatively high due to the viscoelastic properties and long molecular chains and thus generally used for damping materials.

DMTA data from solid amorphous polymers are usually determined in a temperature range including the glass transition temperature (T_g) which is where the polymer transitions from a hard, glassy material to a soft and elastic material.

For semi-crystalline polymers, however a temperature range slightly below the melting point (T_m) are used. Apart from T_g there is also secondary transitions that can be measured. The T_g is usually associated with the movements of the main chain of the polymer whereas secondary transitions are associated with movements of the main chain's side-groups [84].

3.7 Tensile testing

The mechanical behaviour of a material is characterized by its deformation and fracture characteristics under applied tensile, compressive stress. A tensile test provides basic information about the strength of the material. In tensile testing, the material is subjected to a continuously increasing uni-axial load while elongation of the specimen is observed [85].

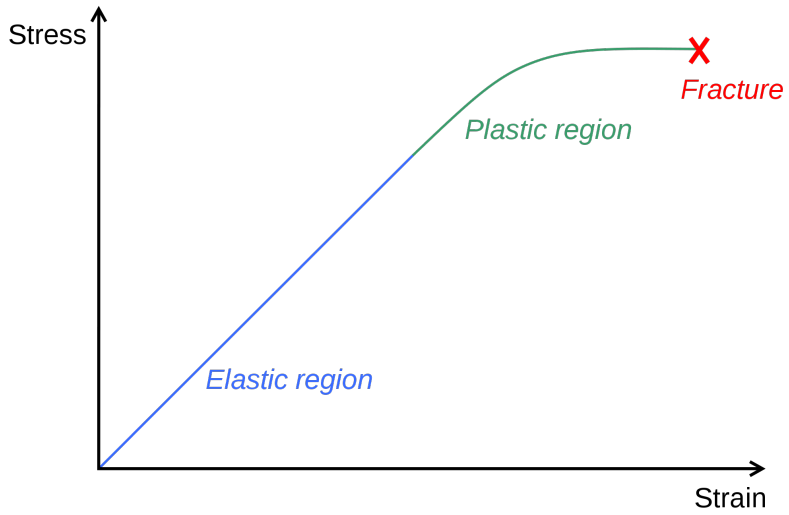

Figure 3.3: Typical stress-strain curve from a tensile strength testing [48] (used with permission).

The load (F) and elongation (δ) are used to calculate the stress (σ) and strain (ϵ). More specifically engineering stress (σ_{eng}) and strain (ϵ_{eng}) are taking the cross-sectional area change into consideration where true stress (σ_{true}) and strain (ϵ_{true}) are only valid during uniform deformation [85]. For the application of energy absorption, where the material is deformed until failure, the engineering stress and strain values are of more interest. Below, some general properties and definitions found in a typical stress-strain curve are defined. See Figure 3.3 for more details.

- Tensile strength (σ_u) is the maximum load a specimen can withstand and is usually the most frequently quoted value from a tensile test.
- Yield strength (σ_y) is the stress at which plastic deformation or yielding of the material is observed.
- Elastic modulus (E) is the slope of the initial linear portion of a stress-strain curve. It is a measure of the stiffness of the material. The modulus depends on the binding-forces between the atoms and is therefore one of the most structure-insensitive mechanical properties of a material.
- Toughness is defined as the material's ability to absorb energy in the plastic range. The toughness may be considered as the total area under the stress-strain curve. This is an indication of how much work per unit volume a material can be subjected to without causing rupture.

To determine the elastic modulus (E) and yield strength (σ_y) used for characterization of the different filament materials, a tensile test was performed. Test data was also compared with the provided material data from the manufacturer. The material parameters were determined from a stress-strain curve. The testing was performed according to the ISO 527 standard [93] for the tensile testings performed in the MTS/20 testing machine, see section 3.7.2.3.

3.7.1 Specimens & preparation

Five specimens were tested for each material according to the ISO 527 standard, the number of measurements above five only yields a greater precision of the mean value [93]. The standard used for the specimens was the ASTM D638 standard [56]. The specimens were grounded prior to the testing according to the grinding procedure described in section 3.8.2.1.

The tensile testing specimens were conditioned in a conditioning room with 50 % relative humidity and a temperature of 23 °C for 48 hours prior to testing to remove any residual stress.

To properly determine the stress-strain curves the thickness and width of the specimens are needed, i.e. the part geometry. The specimens were all measured at three points for the thickness (t), which is uniform over the whole specimen and the width (w), at the smallest section using a digital caliper from TECOS and then taking the average of the measured values. To see the full table of measurements, see appendix A.1.

3.7.2 Tensile testing machines

Below, the different tensile testing machines are discussed regarding limitations and settings.

3.7.2.1 MTS 20/M

For the ABS and PLA, a MTS 20/M tensile testing machine was used. The load was applied at a displacement rate of 1 mm/min. The extensometer with the MTS machine has a fixed length of 50 mm with the possibility to elongate up to 25 mm. The TPU exceeds this value with an outstanding elongation of up to 600 %, therefore an Instron was used for the testing of TPU (see section 3.7.2.3). The MTS 20/M tensile testing machine can be seen in Figure 3.4.

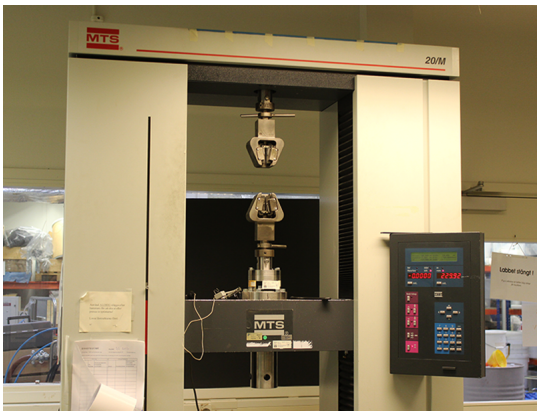

Figure 3.4: MTS 20/M tensile testing machine.

3.7.2.2 Instron 8501

The nylon tensile testing was performed at Swerea SICOMP in Piteå [64] on an Instron 8501 with a 5 kN load cell. The followed standard was ISO 527 [93] and the number of test specimens were seven. The testing speed was 1 mm/min until 0.3 % strain (ϵ) followed by 5 mm/min until 50 % strain (ϵ).

3.7.2.3 Instron 5966

The Instron 5966 used a 1 kN load cell with a displacement of 50 mm/min. The Instron was used for the TPU due to the elongation until break reaching up to 600 % according to datasheet provided by NinjaTek 4.5. The Instron 5966 can be seen in Figure 3.5.

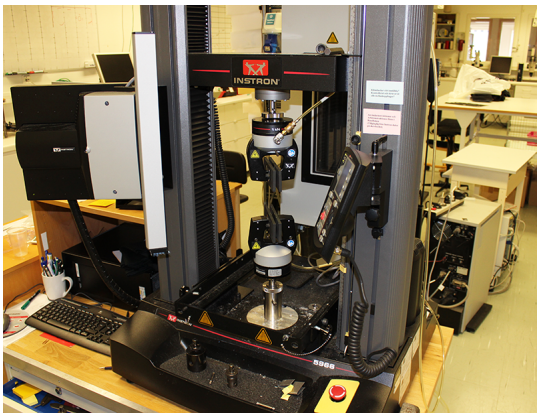

Figure 3.5: Instron 5966 tensile testing machine with optical extensometer.

The Instron uses two predetermined points on the specimens and by using video-processing calculates the elongation for the provided stress-strain curves. This did however cause problem for the TPU, as this machine was not made for handling such large elongations.

3.7.3 Tensile test setup

The different tensile test setups can be seen in Figure 3.6.

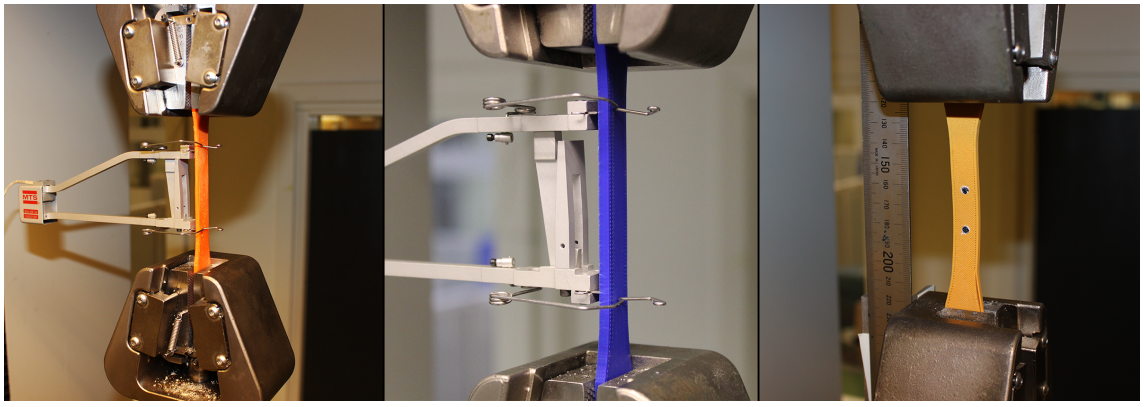

Figure 3.6: Tensile test setup for (from left) ABS, PLA and TPU showing the attached extensometer for ABS and PLA.

- ABS: A moduli test was performed according to ISO 527 standard [93] to calculate a more precise elastic modulus (E) of the material. The load cell used was 1 mm/min and operating in the elastic region with a strain (ϵ) up to 0.3 %. The elongation region was set to 0.05–0.25 %. After the modulus test a tensile test until break was performed on all five specimens, the settings used can be found in section 3.7.2.1.
- PLA: A tensile test until break was performed for all five specimens. The settings used can be found in section 3.7.2.1.
- TPU: The tensile test was performed in an Instron 5966 tensile testing machine. The settings used can be found in section 3.7.2.3.

3.7.4 Compressive testing rig

To test the reference and optimized lattice structures that were decided from points found in section 3.9.1, a compressive testing rig created by SICOMP was mounted in the MTS/20 machine (see section 3.7.2.1). This rig was able to crush specimens in an one directional compressive test. The distance between the clamps was measured using a laser attached to the top piece of the testing rig.

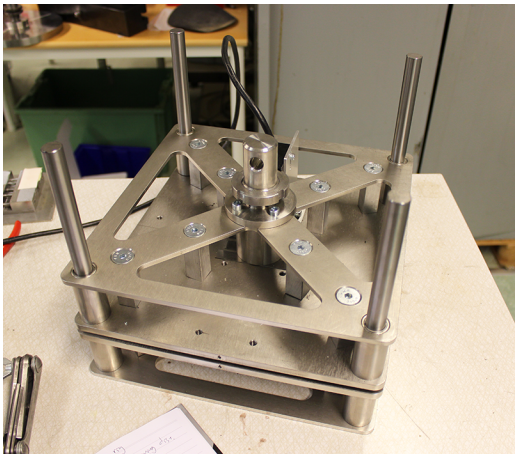

Figure 3.7: Unmounted compressive testing rig by SICOMP.

3.7.5 Failure analysis

After testing, a USB-connected Dino-Lite Digital Microscope was used to examine the fractured surfaces of the tensile test specimens. The USB camera had an adjustable zoom and the live-view of the camera could be seen in the DinoLite-microscope software DinoCapture 2.0 version 1.5.21.A. The mounted digital microscope can be seen in Figure 3.8.

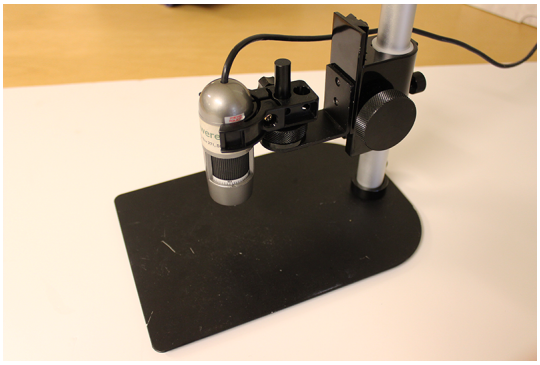

Figure 3.8: Dino-Lite Digital Microscope attached in an adjustable stand.

ABS, PLA and TPU specimens were all analyzed using the digital microscope and representative fracture surfaces were chosen and then further discussed in the Results & Discussion (see section 4).

3.8 DMTA

Figure 3.9 shows representative DMTA specimens for all materials tested in this study.

Figure 3.9: DMTA specimens used, from the left: PLA, ABS, TPU and nylon.

Initially as a part of material characterization, DMTA compression testing was planned to be carried out at the Department of Materials and Manufacturing Technology at Chalmers University of Technology. The machine was a RSA-II with the standard specimen sizes of 16, 25 and 46 mm in diameter and a free variable of thickness. The RSA-II has a temperature range of 150–600 °C. The maximum load for the RSA-II was 10 N.

After consulting the supplied handbook for the RSA-II machine it was noted that only the TPU with an elasic modulus of 12 MPa would be in the recommended output region according to the manufacturer data provided by NinjaTek (see Table 4.5). This would require a test specimen with a height of 1000 mm, which was definitely not feasible. The different diameter standards were investigated but no combination would yield results in the recommended region, therefore, single cantilever DMTA testing would be carried out at SICOMP for all materials. Later it was found out that the TPU would preferably be tested in a tensile DMTA testing mode due to its elastic behaviour.

3.8.1 Rheometrics DMTA Mark IV

The machine used at Swerea IVF for the actual DMTA was a Rheometrics DMTA Mark IV with a maximum force of 15 N. Due to defects in the machine, it could only perform up to 3.7 N. For the single cantilever bending test no pre-tension was used. An additional prerequisite for the test setup was to keep the specimen perpendicular to the oscillating instrument in the test rig for correct results. The suggested modes of testing for the specimens are shown in Table 3.3.

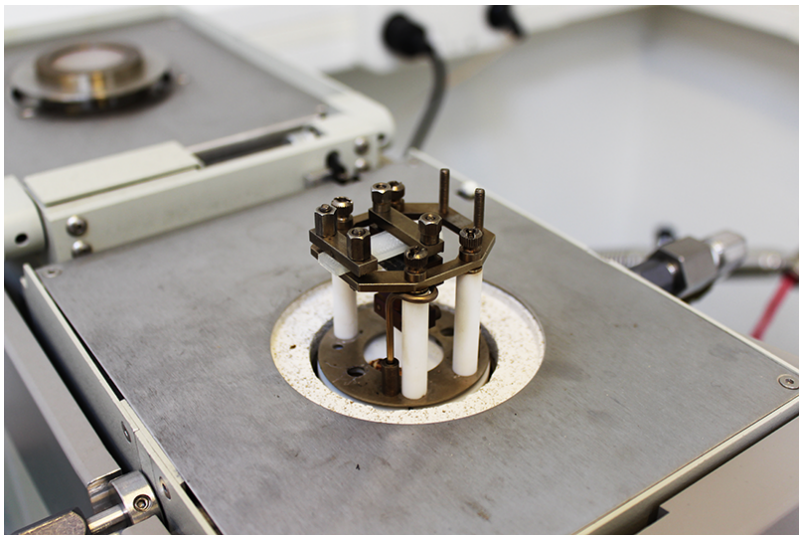

Figure 3.10: DMTA setup of a single cantilever bending, showing a mounted nylon specimen.

Table 3.3: Modes of testing for the DMTA.

Materials	DMTA testing mode
ABS (Innofil3D)	Single cantilever bending
PLA (Primaselect)	Single cantilever bending
TPU (NinjaFlex)	Tension
Nylon (Markforged)	Single cantilever bending

3.8.1.1 Single cantilever bending

Settings of the DMTA were the following:

- The specimens were mounted in a medium sized 14 mm specimen holder and tightened with a torque of 30 cNm as recommended in the suppliers handbook.
- *Dynamic temperature ramp tests* were performed on all specimens. The geometries were adjusted after the specific specimen geometries.
- Frequency was set to 1 Hz according to the ASTM D7028 standard [86].
- The temperature range was set to 25–140 °C. According to ASTM D7028 [86] for DMTA the ramp rate of 5 °C/min is standard, however due to the thickness of the specimens, the rate was set to 2 °C/min. It should be noted that this is a non-standard specimen configuration.
- The strain was set to 0.02 % due to the thickness causing a higher bending stiffness.

3.8.1.2 Tensile testing

Due to the elastic behaviour of the TPU (thermoplastic elastomer), a tensile DMTA testing mode would have been the choice of DMTA testing method to be performed on the NinjaFlex TPU. According to the material datasheet provided by NinjaTek, the T_g temperature is -35 °C. As the temperature range for the DMTA testing is at maximum 25–140 °C, DMTA testing of the TPU was not performed in this study as it would not yield any results.

3.8.2 Specimens & preparation

For the DMTA, specimens of 35x10x3 mm were chosen for the single cantilever DMTA of ABS, PLA and nylon. The specimens size was within the dimensional range according to ASTM D7028 [86]. Representative specimens of all the materials can be seen in Figure 3.9.

Additionally the surfaces of the specimens should be clean, straight and dry to prevent slippage in the grips and mitigate any effects due to moisture. 3D-printing a material usually results in a slightly rough surface due to the layers, therefore grinding of the 3D-printed cantilever specimens was conducted. The specimen size was two per material, according to the ASTM D7028 standard [86].

3.8.2.1 Grinding procedure

The procedure of grinding the specimens was performed in a Struers LaboPol-5 machine. SICOMP already has a standard for grinding procedures which was utilized in this study. The different P-values below refer to the sizes of the abrading particles on the sandpaper. The following procedure was carried out on the specimens:

- The specimen, sandpaper and grinding turntable as well as specimen holder place was rinsed with running water after each and before the first step.
- The first step consists of sandpaper of P500 during 2 minutes on the lowest speed of 300 rpm.
- The force was slightly deviated from the procedure of metals: 20 N due to the specimens being polymers. The cantilever specimens were held by hand and the build-up for the sandpaper was also adjusted to steps of P220, P320, P500 and finally P800.

The dimension for the nylon cantilever was set to 35x10x2 mm and due to the high printing precision of the Markforged Mark One machine, little to no grinding was needed on these specimens prior to testing.

3.9 Optimized lattice structure for energy absorbing applications

In conjunction with a parallel project performing the optimization [51], three optimized lattice structures in the filament material nylon were chosen, printed and then tested in a compressive testing rig (see section 3.7.4).

Settings and testing procedure are presented below:

- The compressive tests were performed up until 10 kN was registered in the load-cell. This is also the maximum load of the load-cell.
- The speed was set to 8 mm/s for all structures.

The sample size was set to one per material due to high costs and the main purpose being to only show the proof of concept. In general, more energy absorbent efficient structures can be printed in today's commercially available 3D-printers by tailoring the structure whilst saving material.

3.9.1 Selection of optimized lattice structures

The CAD renderings of the three selected structures optimized for nylon by Markforged can be seen in Figure 3.11 and the final printed structures can be seen in Figure 3.12. All lattice structures were optimized for maximum energy absorption based on the material properties of nylon. The following aspects were taken into consideration when selecting the final structures to be printed:

- The precision of the 3D-printer, its manufacturability and reproducibility of produced prints. Furthermore, an appropriate size that still would allow for post processing of the prints was a main goal, although difficulty of support structure removal was experienced for the tetrahedron.
- Material properties based on the characterization of this study. Mainly, the strength-to-elongation ratio.
- The resulting energy-absorption values (toughness) determined from the area under the tensile testing-curves.
- Results from the tan(δ)-curves from the DMTA, an additional way of characterizing the energy absorbing capability of the material.

3.9.1.1 3D-printing & structures

When printing the lattice structures, a fine precision of the 3D-printer was needed. In this regard, the Markforged Mark One is the superior of the commercially available desktop printers compared to MakerBot Replicator 2 and 2x. With a precision of 0.00625 mm compared to 0.1 mm of the MakerBot, the Markforged completely outperforms the MakerBot printers, although at the expense of the cost.

The nylon and thus Markforged printer were therefore the choices of material and printer used in this study.

After deciding on the three lattice structures, the stl files of the optimized geometries were then analyzed and fixed for geometry errors in *Materialize Magicx*. Finally, the lattice structures were then printed in pure nylon by a Markforged printer.

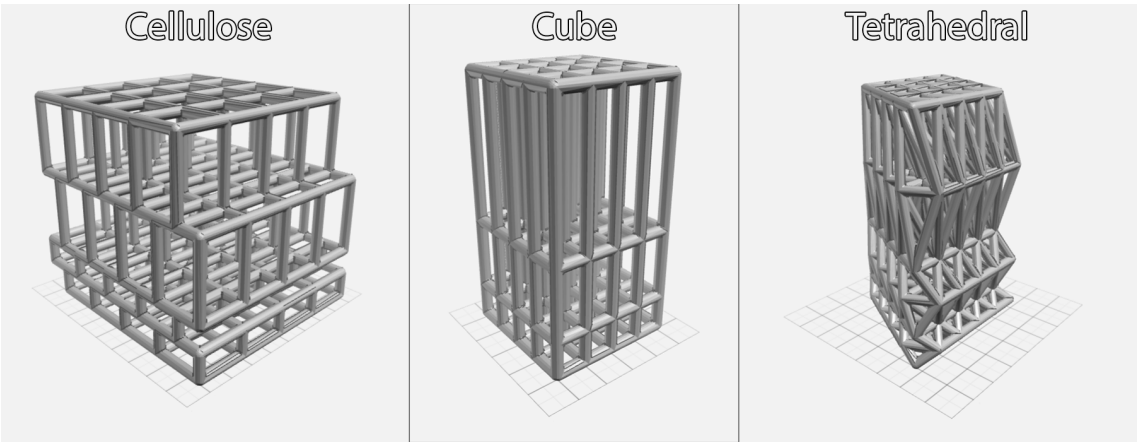

Figure 3.11: CAD images of the optimized nylon lattice structures [51].

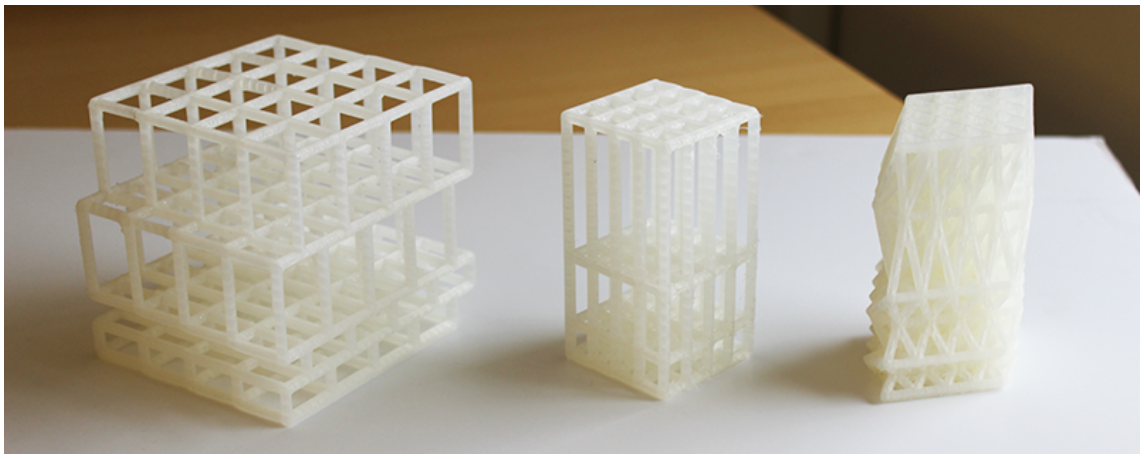

Figure 3.12: 3D-printed optimized nylon lattice structures.

Printing challenges

- Cellulose: The printing of the cellulose failed in some beams and was therefore fixed using manual hot soldering and matching the printing temperature of the Markforged Mark One. In theory this would yield identical results to that of a normal 3D-printer. See Appendix A.3 for more details on successful and failed beams.
- Tetrahedral: The support structures for the two bottom layers were not able to be removed due to the high resolution and fine details of the print causing limited reach with additional post processing tools.

Weight of the structures

To compare the energy absorption capabilities of the lattice structures with the conventional EPS foams the weight of the samples was required. The optimized lattices structures were weighted with a VWR SE 622-scale with a 0.01 g accuracy. The weights of the structures are presented in Table 3.4.

Table 3.4: Weights of the optimized 3D-printed nylon lattice structures.

Structure	**Weight [g]**
Cube	27.60±0.01
Cellulose	61.61±0.01
Tetrahedral	62.00±0.01

3.9.1.2 Test setup

The compressive test of the optimized lattice structures was performed in an MTS/20 tensile testing machine. The testing was video recorded with a Canon 600D. Additional lightning was used using a Lastolite RayD8 C5600 with an 85 W fluorescent bulb with 5600 K (daylight) temperature. The compressive test setup can be seen in Figure 3.13.

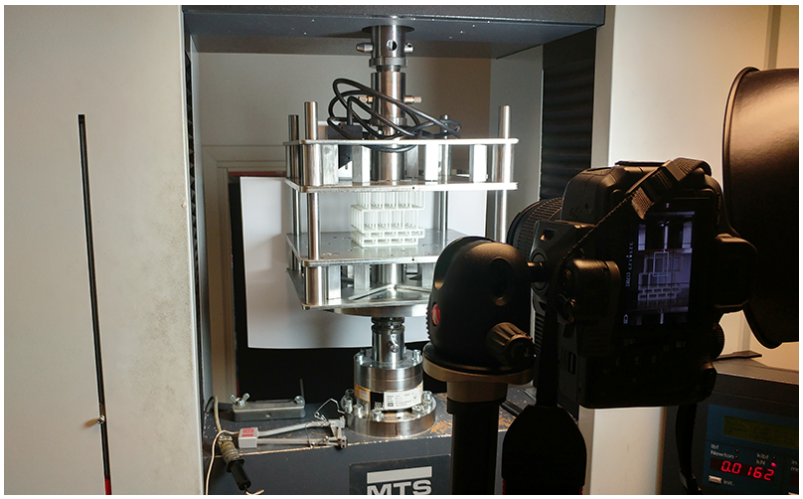

Figure 3.13: Compressive test setup for the compressive test in MTS/20 tensile testing machine.

4

Results & Discussion

4.1 3D-printing

Processing challenges were experienced when printing the ABS and TPU. The 3D-printing of these two materials is discussed in the section below. The PLA had little to no difficulties during printing.

4.1.1 ABS

A well known fact for printing ABS is its difficulty during printing, usually the adhesion to the build platform [79]. Especially in the case of the Replicator 2x, the build platform's level is crucial for a successful print [63]. In contrast, printing of PLA in the MakerBot Replicator 2 was a relatively straightforward process.

When 3D-printing of the thermoplastic ABS in the Replicator 2x, the build platform appeared to be shaking and almost vibrating during printing. This may have caused incorrect placement of the filament and ultimately affected the final structure and its mechanical properties during testing.

4.1.2 TPU

The temperature was initially adjusted for the TPU which was suggested to be the cause of unsuccessful prints. It was later noted that this was instead caused due to the speed of the nozzle when depositing the filaments.

As mentioned in section 3.7, adjusting the speed of the nozzle in the MakerBot Replicator 2 had no desired effect. The third-party slicer software Simplify3D had the possibility to adjust this parameter correctly. This shows that using a third-party software can drastically increase the quality of the prints. If the ABS and PLA tensile test specimens were to be printed again, the usage of a 3rd-party software to create their respective x3g/G-code would be considered. This problem was noticed after printing the tensile test specimens in NinjaFlex TPU where the undesired infill density caused unsuccessful prints when using the MakerBot MakerWare.

Using the MakerBot Replicator 2 with the MakerWare software did not yield desired results regarding the infill and shell density. The printing speed was therefore adjusted in *Simplify3D* to ensure proper deposition of the filament. The following parameters were used in *Simplify3D*:

- The *Simplify3D* does not distinguish between the infill and shell printer speed and instead uses a global speed for the whole print. The printing speed was decreased to 1800 mm/min (30 mm/s).
- *Filament size* was adjusted after measuring the filament using a digital caliper, this was set to 1.72 mm for the filament used in this study. This adjustment helped solve the problem of insufficient amount of material being extruded through the nozzle.
- The *printing order* was changed to *outside-in* instead of the normal setting *inside-out* to minimize problems with infill according to recommendations from Swerea IVF.
- *Extrusion multiplier* allows for tweaking of the flow rate with respect to time. E.g. a value below 1.0 would not fill to 100 % regardless of the infill density. This was set to 1.0 to ensure sufficient flow rate.
- *Overlap* determines how much of the infill will overlap the outer shell. This was set to 20 % for tensile test specimens 1–3, 30 % for the 4th specimen and 50 % for the 5th specimen, see Figure 4.5. Increasing this parameter further yielded little to no change. This was verified when printing the DMTA specimens.
- *Layer height* was held constant at 0.2 mm to match the layer height set in the MakerBot printers.

4.2 Tensile testing

Tensile testing was performed on standard tensile test specimens according to the ASTM D638 standard [56] used for polymers. To characterize the material properties of the materials the elastic modulus (E), tensile strength (σ) and elongation at break (ϵ_B) was determined from the stress-strain curves. The materials were compared in a qualitative study. The calculated material properties from the tensile testing from each of the materials are presented below, see 4.1 for a full comparison.

4.2.1 Material properties

The elastic modulus (E) was determined by using the curve-fitting (trendline) tool in Microsoft Excel for the linear 0.1 – 0.3 % elongation region of the stress-strain curves [56]. The found slope was then the estimated elastic modulus (E) of the material, see Table 4.1 for calculated elastic modulus.

Table 4.1: Calculated material properties for the 3D-printed tensile test specimens.

Materials	Elastic Modulus (E) [GPa]	Tensile Strength (σ) [MPa]	Elongation at break (ϵ_B) [%]
ABS (Innofil3D)	1.93±0.04	33.26±0.91	2.46±0.03
PLA (Primaselect)	3.41±0.26	60.12±1.97	2.63±0.03
TPU (NinjaFlex)	0.0039[1]	10.51±1.47	548±8
Nylon (Markforged)[2]	0.89±0.06	29.54±0.5	42.96±0.78

4.2.2 ABS

For the ABS, a modulus- and tensile test until break was performed. During testing, the 4th specimen was experiencing sliding, the test was aborted and the specimen had to be roughened up using a steel brush to increase the friction between specimen and tensile machine holder. The test was then performed again, however this did not show any difference compared to other specimens for the stress-strain curve seen in Figure 4.1. The fractured specimens are shown in Figure 4.2. Test specimen 1 was omitted from the calculations presented in Table 4.1.

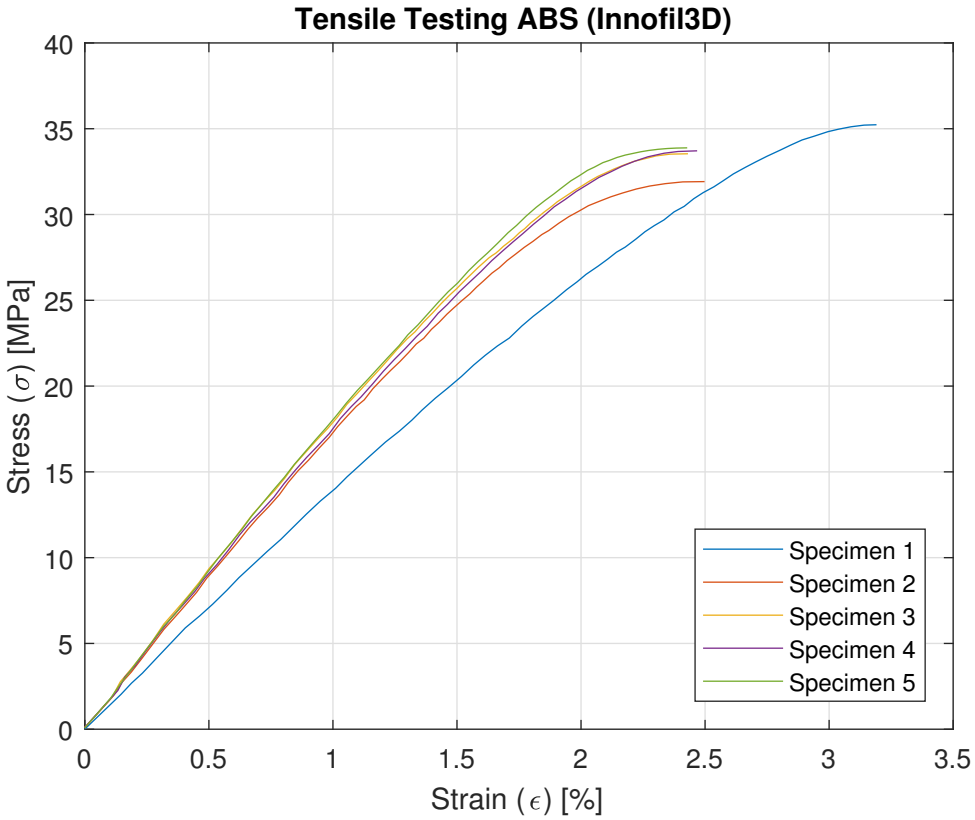

Figure 4.1: Stress-strain curve of the tensile tested 3D-printed Innofil3D ABS.

[1]Elastic modulus (E) determined from specimen 1 in 0.1–0.3 % strain region.
[2]Tests performed by Swerea SICOMP, Piteå [64].

Figure 4.2: Fractured tensile test specimens of the 3D-printed Innofil3D ABS.

Specimens 1–5 all fractured in a brittle manner, i.e. little to no plastic deformation was shown. However, the location of the fracture differs between specimens, this would suggest local defects. No necking was visible on the specimens.

Innofil3D (ABS) - Manufacturer datasheet

The material properties provided by Innofil3D can be found in Table 4.2 below.

Table 4.2: Material properties by Innofil3D ABS with 100 % infill density according to ISO 527 standard [93].

Innofil3D ABS Material Datasheet		
Elastic Modulus (E) [GPa]	**Tensile Strength (σ) [MPa]**	**Elongation at break (ϵ_B) [%]**
2.03 ± 0.45	29.3 ± 0.8	3.7 ± 0.9

The provided manufacturer material properties for the ABS show the standard deviation for the specimens which makes the comparison of found material properties more significant and also show the predictability of reproducibility of the prints. The reproducibility is a main issue with additive manufacturing where this usually tends to be very poor, especially in commercially available 3D-printers today.

4.2.3 PLA

A consecutive tensile testing until failure was performed for five 3D-printed PLA tensile test specimens. Test specimen one was omitted from the calculations found in Table 4.1 due to major deviation from the rest of the samples. The resulting stress-strain curve can be seen in Figure 4.3.

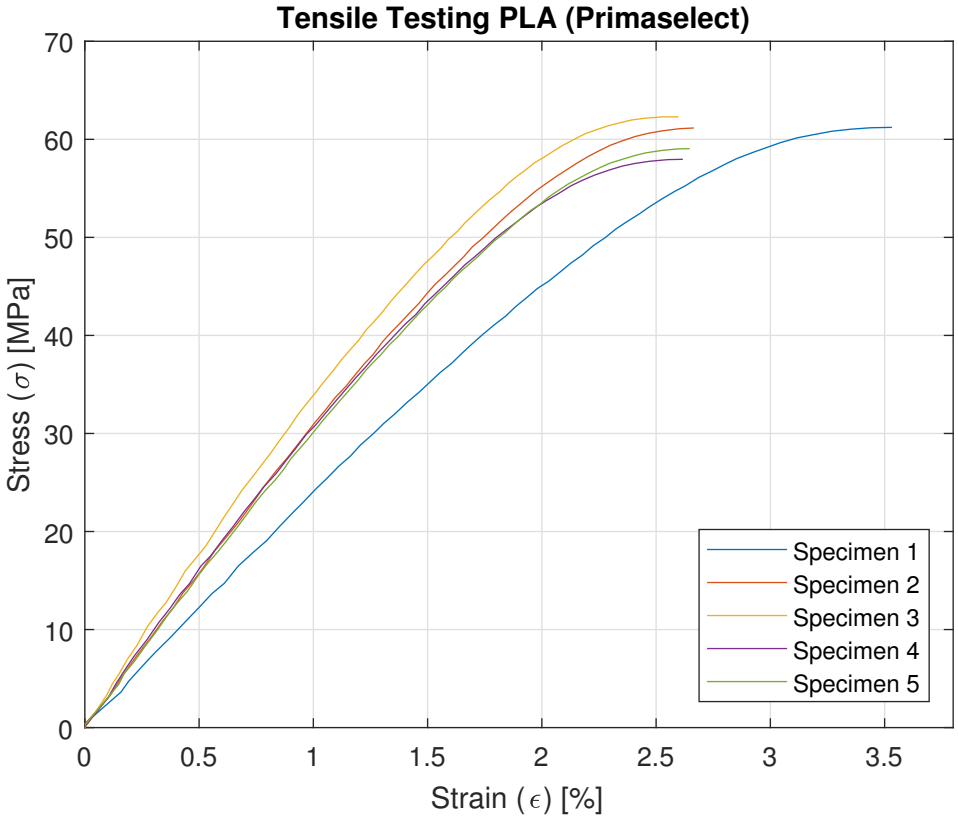

Figure 4.3: Stress-strain curve of the tensile tested 3D-printed PLA by Primaselect.

Specimens 1–5 all fractured in a ductile manner, i.e. showing a large plastic deformation. However, the 4th specimen only had a small portion of visible ductile fracture over its fractured surface. It can therefore be concluded that the remaining part experienced a rapid crack growth. Figure 4.4 shows the fractured specimens of the PLA tensile testing.

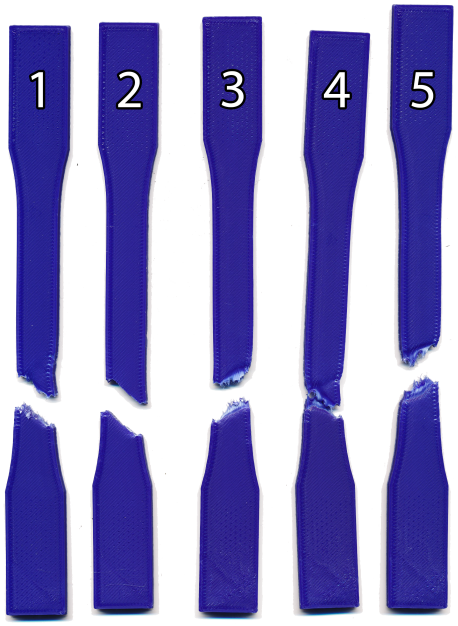

Figure 4.4: Top view of the fractured 3D-printed tensile test specimens in PLA by Primaselect.

Primaselect (PLA) - Manufacturer datasheet

The material properties provided by Primaselect can be found in Table 4.3 below.

Table 4.3: Material properties provided by Primaselect according to ASTM D882 standard [87] performed in machine direction (MD).

Primaselect PLA Material Datasheet		
Elastic Modulus (E) [GPa]	**Tensile Strength (σ) [MPa]**	**Elongation at break (ϵ_B) [%]**
3.31	110	1.6

The provided material datasheet does not show any standard deviation, i.e. the reproducibility or spread of the 3D-printed PLA filament is therefore not shown. The standard used by the manufacturer was ASTM D882 which is a method for thin plastic sheets [87]. This may describe the large difference in the tensile strength (σ) from the found material property. However, the found elastic modulus (E) for the tests performed corresponds well to the provided material properties from Primaselect.

4.2.4 TPU

Due to the low rigidity and high elongation of the NinjaFlex (TPU), performing a normal tensile test according to the standard method ISO 527 [93] was not possible. Therefore the stress-strain curve presented in Figure 4.7 was calculated from the obtained load-displacement data. The tensile test specimens used for the testing of the TPU can be seen in Figure 4.5. Note the increased density between the shell and the core with increased specimen number.

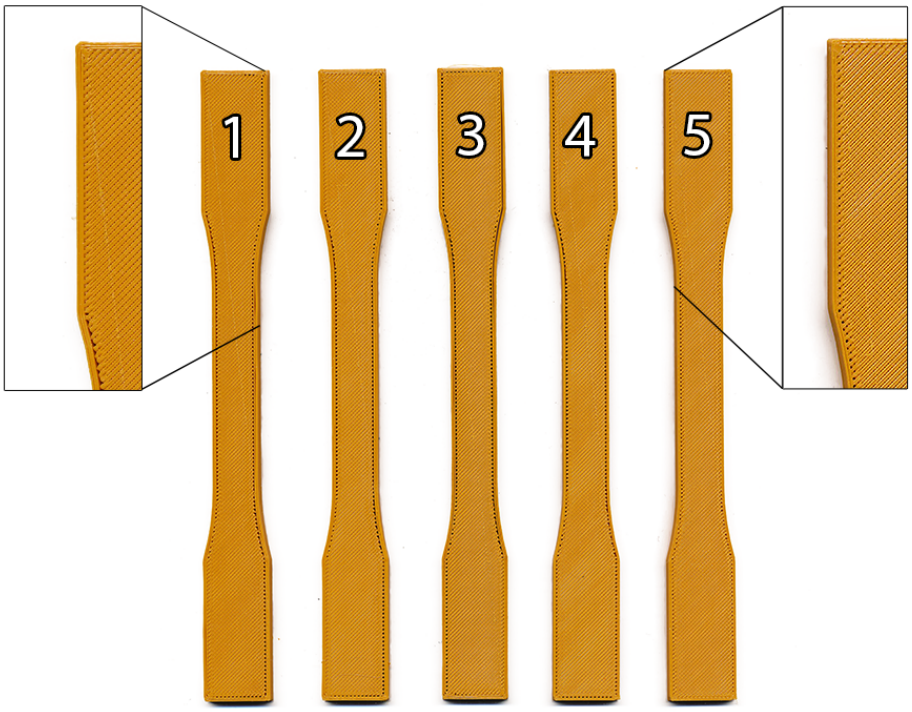

Figure 4.5: Tensile test specimens for TPU according to ASTM D638 standard [56], showing the coarse infill on specimen 1 and uniform infill on specimen 5.

Setup and testing

The low rigidity of the TPU did not allow for the attachment of an extensometer, therefore the strain was not recorded using a normal extensometer.

The Instron 5966 machine has the possibility for optical extension recording, where two points are marked on the specimen and then synced by using a camera. This would allow specimens with low rigidity to be tested that cannot have an extensometer attached to them, which is the case for the TPU. However, the optical extensometer was only able to correctly record an elongation up to 1 % for test specimen one. After this, the test specimen went outside of the boundaries of the optical extensometer's field of view.

Tensile specimen two was tested in the MTS/20 machine but the limit of the machine was reached before failure. Therefore, the rest of the specimens were then again chosen to be performed in the Instron 5966 machine.

The tensile testing for specimens 3–5 in the Instron 5966 machine had only the possibility to record the load vs. displacement data. The extension was therefore recorded manually using a bevel gauge which can be seen in Figure 4.6. The average and standard deviation of these manual measurement of the elongation at break are presented in Table 4.1 for the TPU. The manually measured elongation (ϵ) for specimens 3–5 can be seen in Table 4.4. The load vs. displacement curves for the specimens can be seen in Figure 4.7 and the calculated stress-strain curve based on the load vs. displacement curves is shown in Figure 4.8.

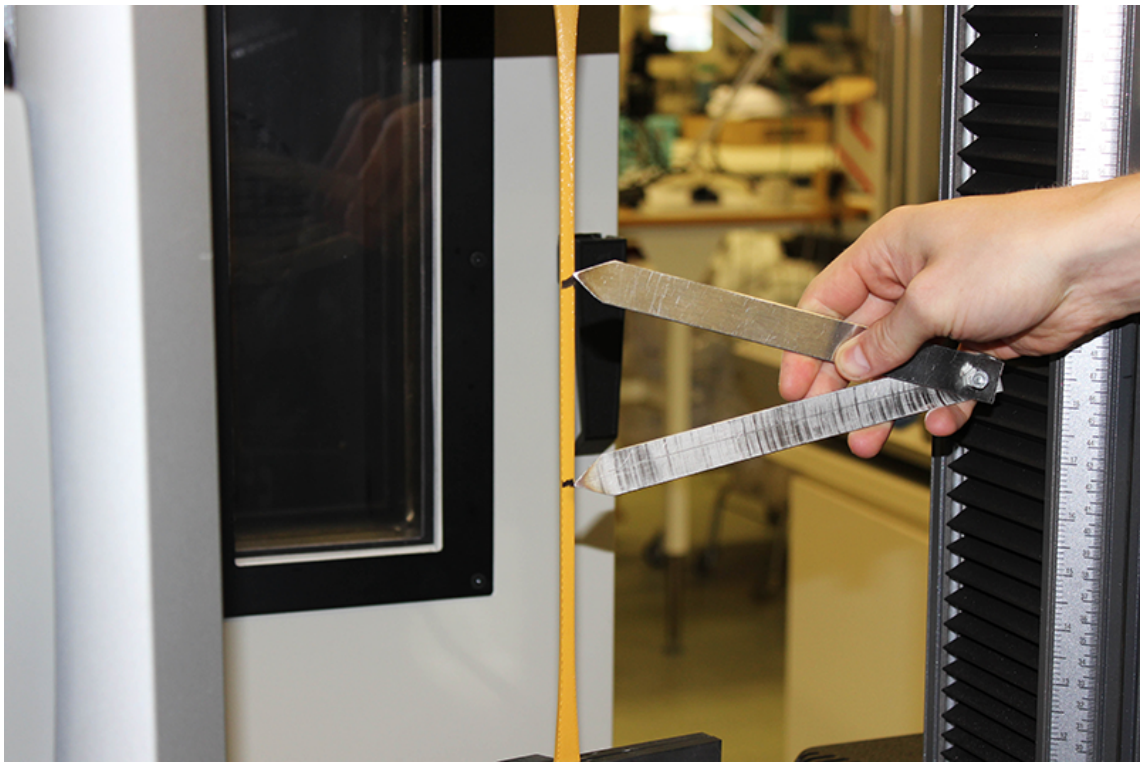

Figure 4.6: Manual measurement of elongation using a bevel gauge for NinjaFlex TPU in an Instron 5966 machine.

Table 4.4: Elongation at break (ϵ_B) measured manually with bevel gauge for TPU tensile test specimens 3–5 according to the ASTM D638 standard [56].

NinjaFlex TPU (NinjaTek)	
Test specimen	**Elongation at break (ϵ_B) [%]**
3	540
4	548
5	556

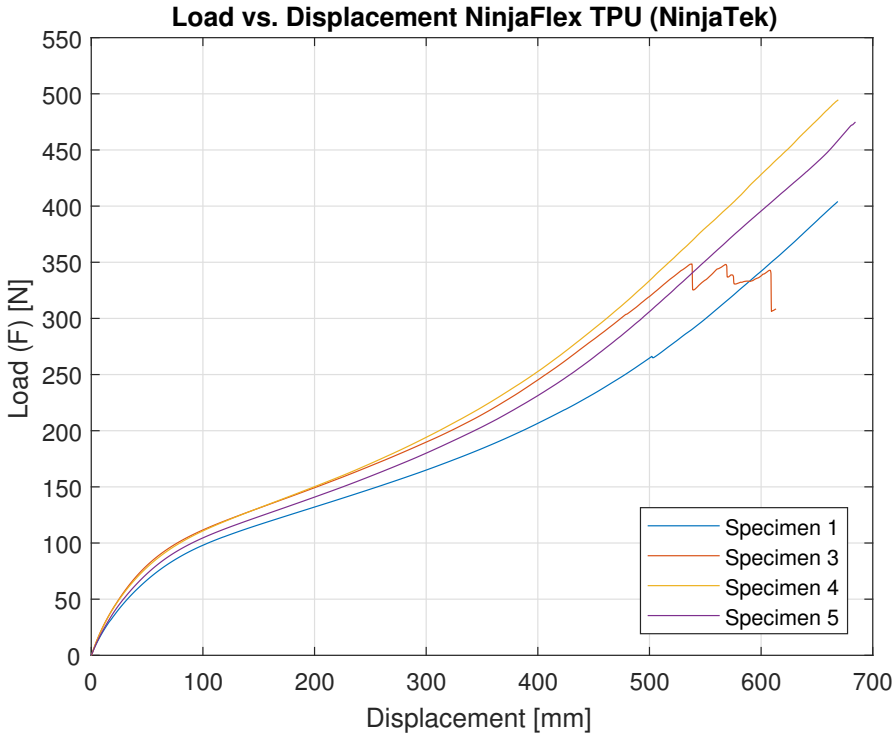

Figure 4.7: Load vs. displacement curves for NinjaFlex TPU.

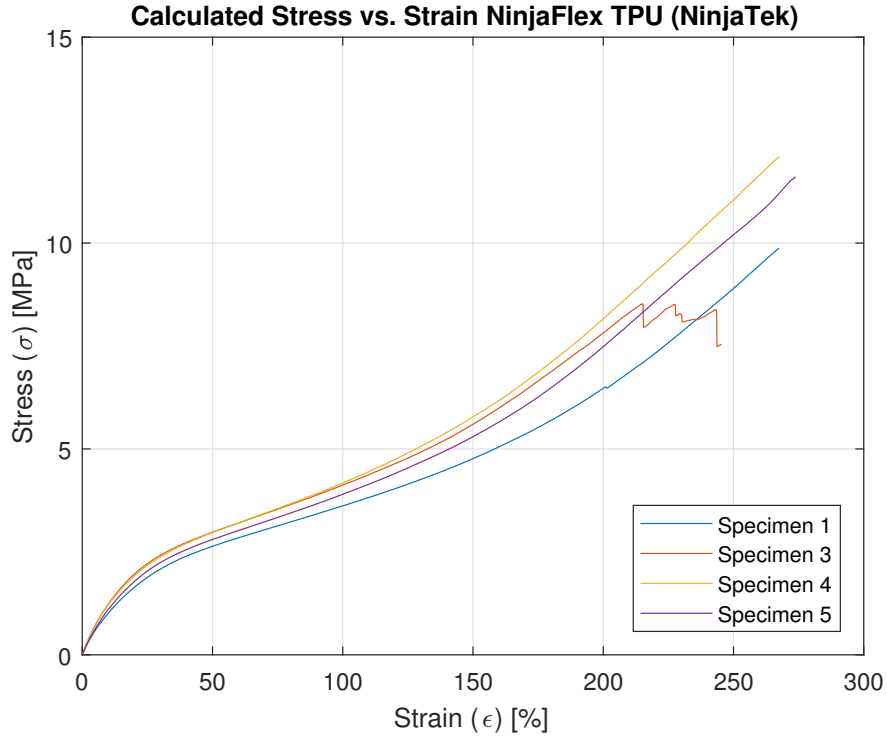

Figure 4.8: Calculated stress-strain curves from the load vs. displacement data for NinjaFlex TPU.

Only the load vs. displacement and calculated stress-strain curves were presented for the TPU. This is however not correct as the displacement records only the movement of the grips and the initial L_0 which is used to calculate the strain values from these values was unknown.

The found elastic modulus (E) was only determined from test specimen 1 as this test was the only specimen using the optical extensometer. The settings were identical for the remaining specimens 3–5, however only the manual extension was measured. For the application of bicycle helmets we want to determine the behaviour of the material response all the way until break, as these tests ultimately only yielded a single correct value, i.e. the elongation at break, this is not of much use for the impact-absorbing applications. However, it can be understood from the comparison that the TPU is by far the most elastic of the materials tested in this study.

Furthermore, elastic modulus is usually calculated at fixed strain percentages: 100, 200, 300 % and so on for rubber materials, which would be the ideal case for the TPU. This would however make the quantitative study between the materials difficult.

It was noted during testing that the outer shell layer of the TPU snapped gradually on test specimen 3, from the outside and in. This was noted in the form of a fluctuating load in the load vs. displacement-curve as shown in Figure 4.7.

This gradual snapping was not shown for test specimen 4 or 5, which can be linked to the extrusion multiplier-setting which was increased to a multiplier above 1.0 for these specimens. This successfully fused the outer shell layers together and thus preventing separation between the outer shell and the infill (core) of the specimen. More on the extrusion multiplier can be found in section 4.8.1.

NinjaTek NinjaFlex (TPU) - Manufacturer datasheet

The datasheet provided by NinjaTek is presented in Table 4.5 below.

Table 4.5: Material properties for NinjaFlex by NinjaTek according to ASTM D638 standard [56].

NinjaTek NinjaFlex Material Datasheet (TPU)		
Elastic Modulus (E) [GPa]	**Tensile Strength (σ) [MPa]**	**Elongation at break (ϵ_B) [%]**
0.012	26	660

4.2.5 Nylon

Tensile tests performed on nylon from Markforged were carried out by Swerea SICOMP in Piteå [64]. The specimens followed the ISO 527 standard [93] and were printed in a Markforged Mark One 3D-printer. No grinding procedures were performed on the specimens prior to tensile testing. The specimen testing size was set to 7. The tests were performed in an Instron 8501 with a 5 kN loadcell. The resulting stress-strain curve can be seen in Figure 4.9.

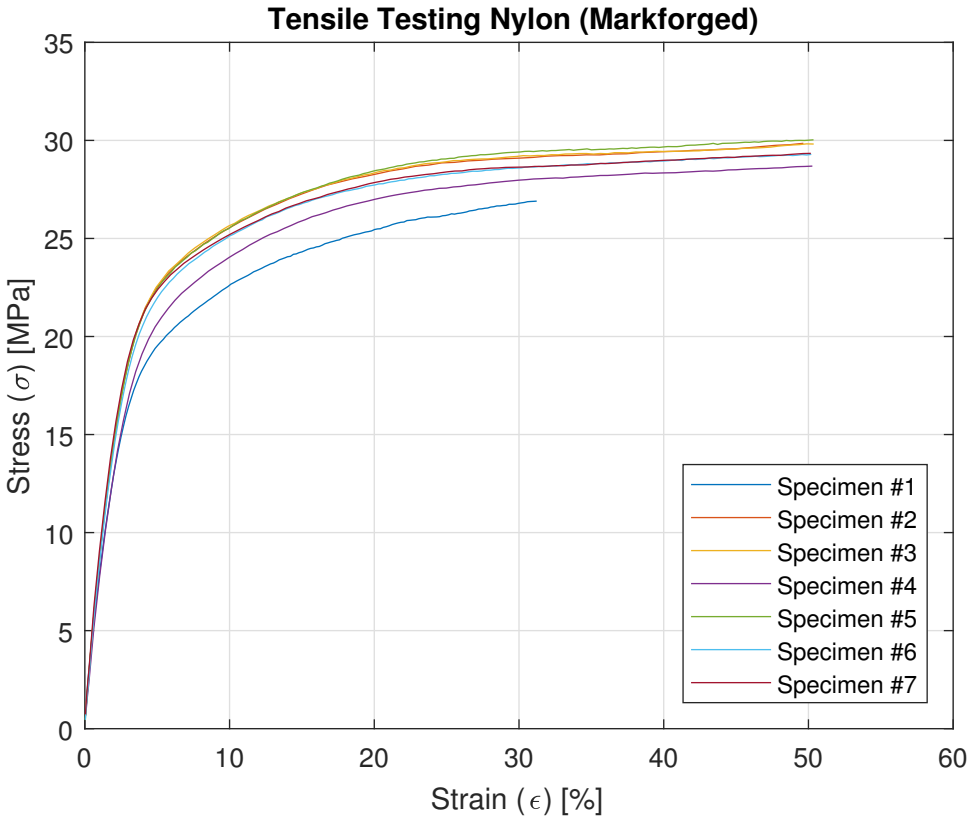

Figure 4.9: Stress-strain curve of nylon by Markforged.

When comparing the found results with the properties provided by Markforged, it was noted that no deviations were presented by the manufacturer and thus making it harder to determine the spread of the values. The material properties provided by Markforged can be found in Table 4.6.

Markforged nylon - Manufacturer datasheet

The manufacturer datasheet from Markforged is presented in Table 4.6 below.

Table 4.6: Material properties provided by Markforged for nylon.

Markforged nylon Material Datasheet		
Elastic Modulus (E) [GPa]	**Tensile Strength (σ) [MPa]**	**Elongation at break (ϵ_B) [%]**
0.94	54	2.6

4.3 Tensile test comparison

The representative stress-strain curves for ABS, PLA, nylon and TPU can be seen in Figure 4.10.

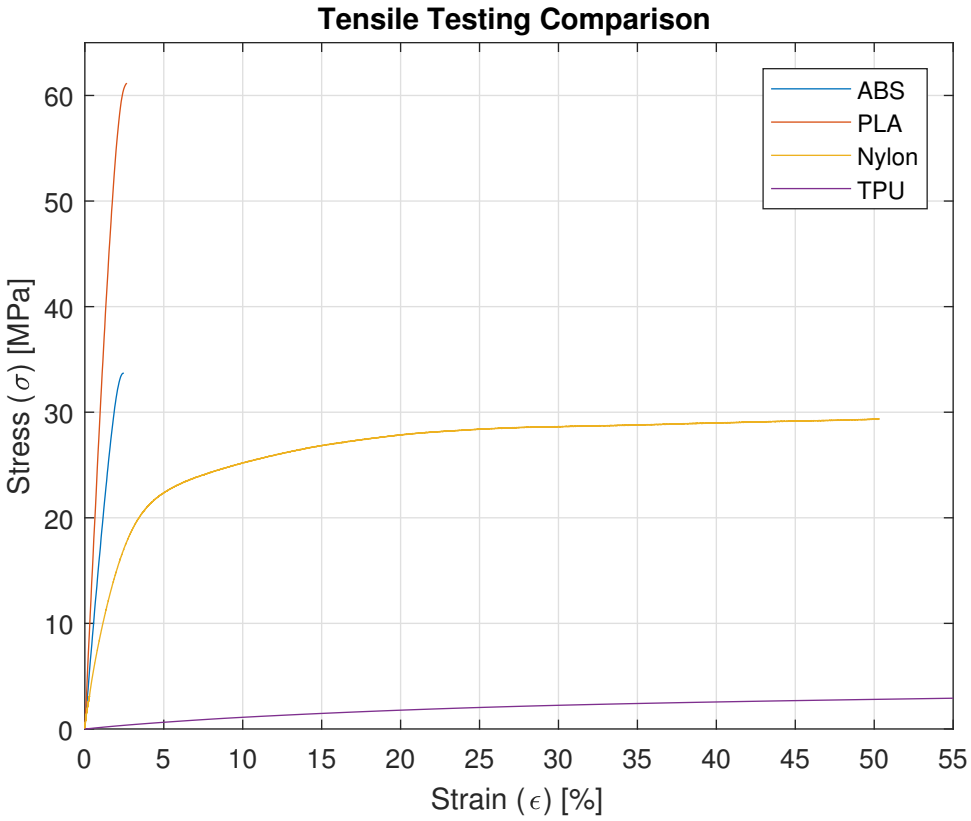

Figure 4.10: Representative stress-strain curves for ABS, PLA, nylon and TPU.

From the comparison graph, it is clear that TPU has an excellent strain (ϵ) but very low strength (σ) compared to ABS and PLA with a moderate to high strength but low strain values. The nylon however, exhibits a high elongation yet moderate strength.

4.3.1 Material toughness

When comparing the stress-strain curves of the different materials, the area under the curves was calculated. The toughness was calculated in MATLAB using the function *trapz* which estimates the area under the curve via the trapezoidal method. See Figure 4.11 and Table 4.7 for estimated toughness on each material. The toughness can also be thought of as a measure of the material's energy absorption, it is measured in J/m^2.

Worth noting is that the results are based on a tensile test, whereas in impact energy absorption we are interested in the compressive properties. In the case of polymers, the material tends to exhibit a much higher compressive strength compared to its tensile strength. There is little to no benefit of tensile strength in an impact-absorbing application other than tensile stresses that might occur in a connected lattice structure system. However, the toughness based on the tensile test gives a comparison between the material for applications subjected to tensile forces.

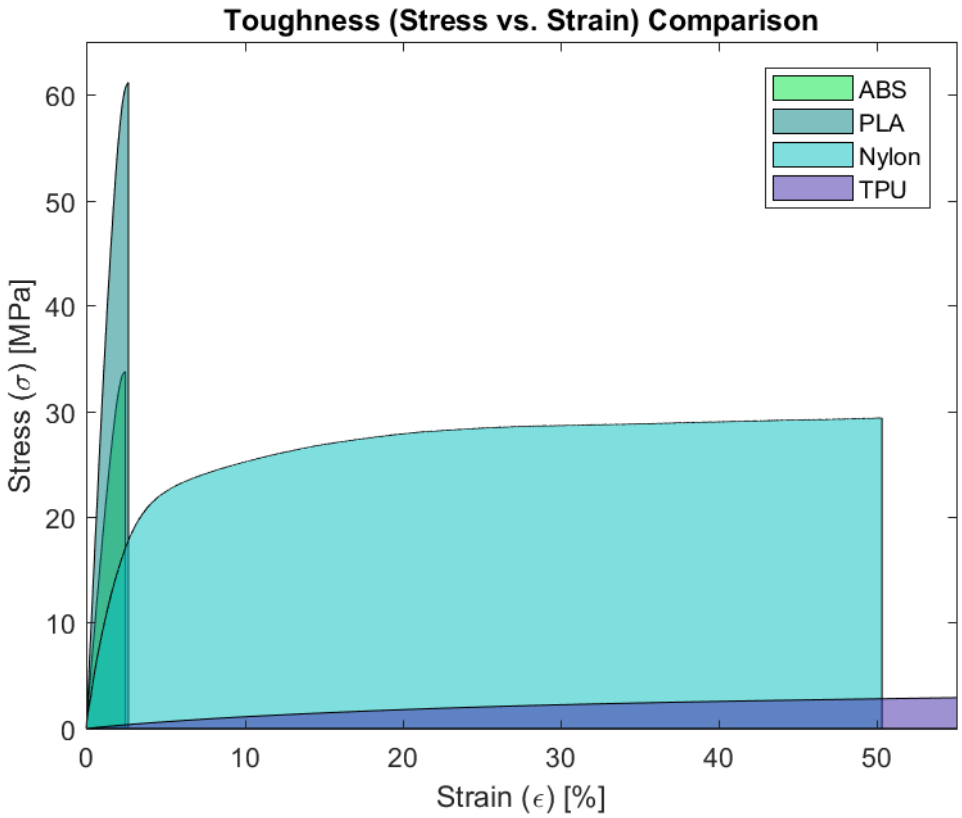

Figure 4.11: Areas under the stress-strain curves for the tested filament materials.

Table 4.7: Tensile toughness of 3D-printed filament materials.

Materials	Calculated toughness [J/m^2]
ABS (Innofil3D)	4.95×10^5
PLA (Primaselect)	9.90×10^5
TPU (NinjaTek)	1.50×10^7
Nylon (Markforged)	1.34×10^7

4.4 Failure analysis

Generally, the fracture of a specimen can generally occur as a result of either material defect or maximum ultimate stress of the material is reached.

The characteristic failures for all materials are presented below, two in the case of PLA and one for ABS and TPU. Fracture occurred with negligible necking for all materials. The resulting microscopy images of each material are presented in the subsections below.

4.4.1 ABS

The fractured surface shows clear indications of porosity between the 3D-printed filaments. Song et al. [74] concluded in their studies on 3D-printed specimens that the porosity can be minimized by adjusting the printing temperature, extrusion speed and nozzle speed. The influence of the extrusion speed are further discussed in section 4.8. The microscopy of the fractured ABS surface and fractured pieces put together, respectively, can be seen in Figure 4.12 (views A and B).

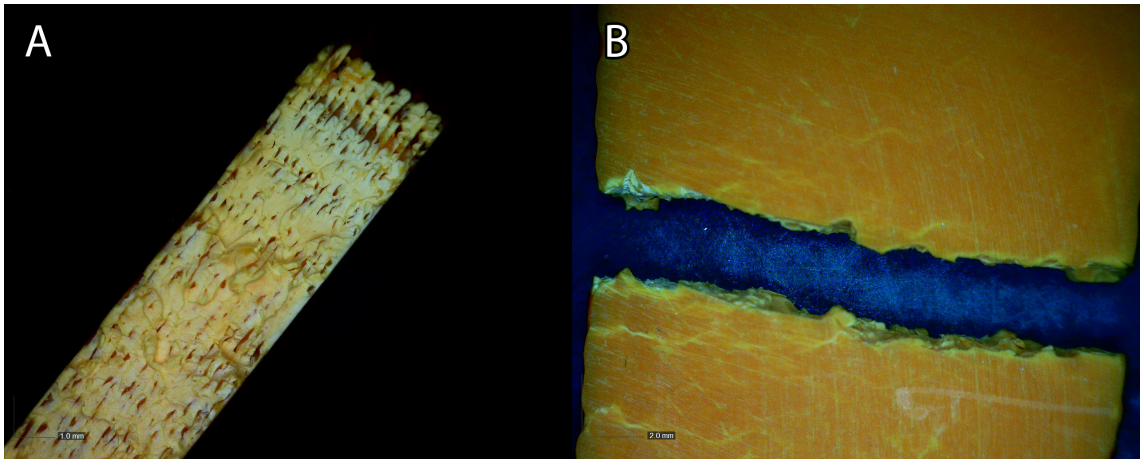

Figure 4.12: Micrographs of failed Innofil3D ABS tensile test specimen five.

4.4.2 PLA

The PLA specimens fractured in two characteristic types of failures:

- Brittle fractured PLA surface and fractured pieces put together, respectively, can be seen in Figure 4.13 (views A and B).
- Ductile fractured PLA surface and fractured pieces put together, respectively, can be seen in Figure 4.13 (views C and D).

In the case of brittle fracture, the fracture seems to have started in the edge of the specimen in a ductile manner, possibly initiated by a surface defect. The crack was then propagated in shear through the layers and finally ended in a ductile fracture on the other end of the specimen in the width direction before final rupture occurred. The brittle fracture surface can be correlated with the low elongation at break (ϵ_B). The microscopy of the two representative fractured PLA surfaces and fractured pieces put together can be seen in Figure 4.13.

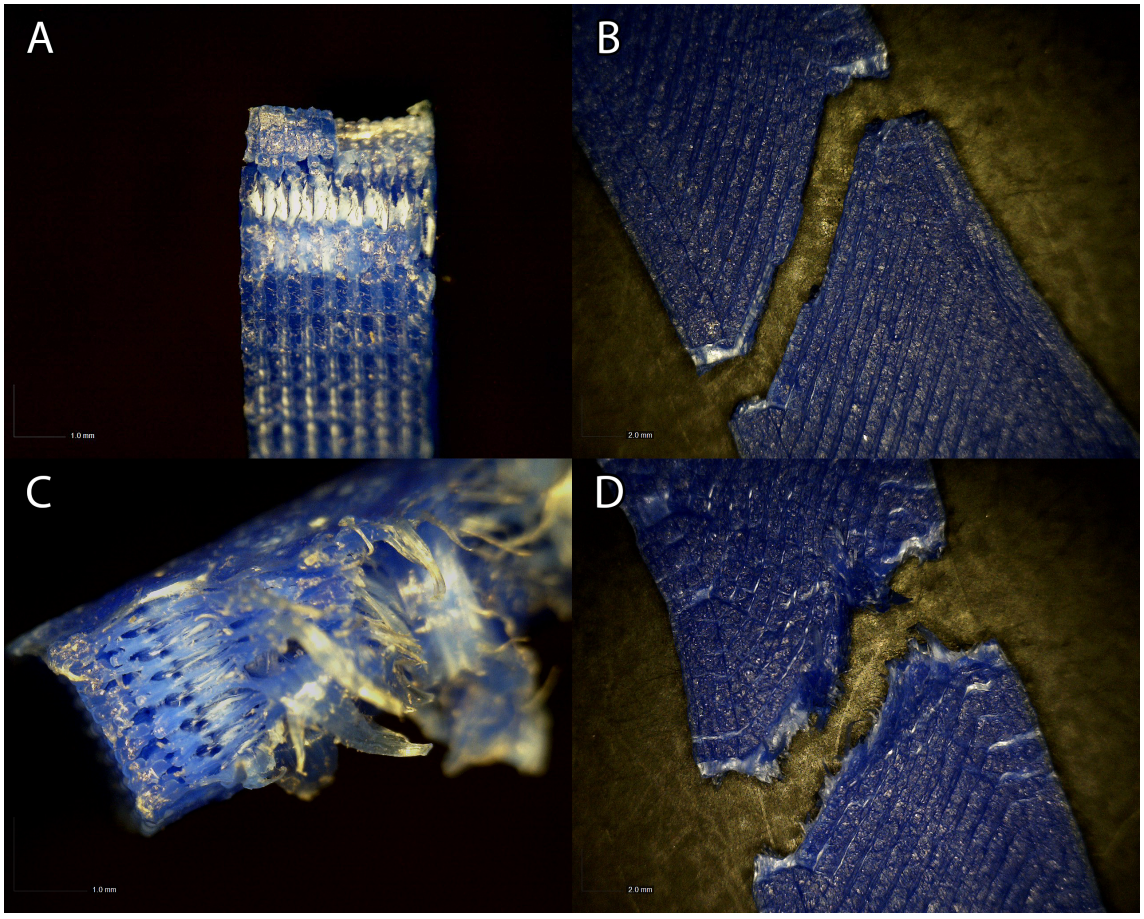

Figure 4.13: Micrographs of failed Primaselect PLA tensile test specimen four and five.

4.4.3 TPU

The microscopy of the fractured TPU surface and fractured pieces put together, respectively, can be seen in Figure 4.14 (views A and B).

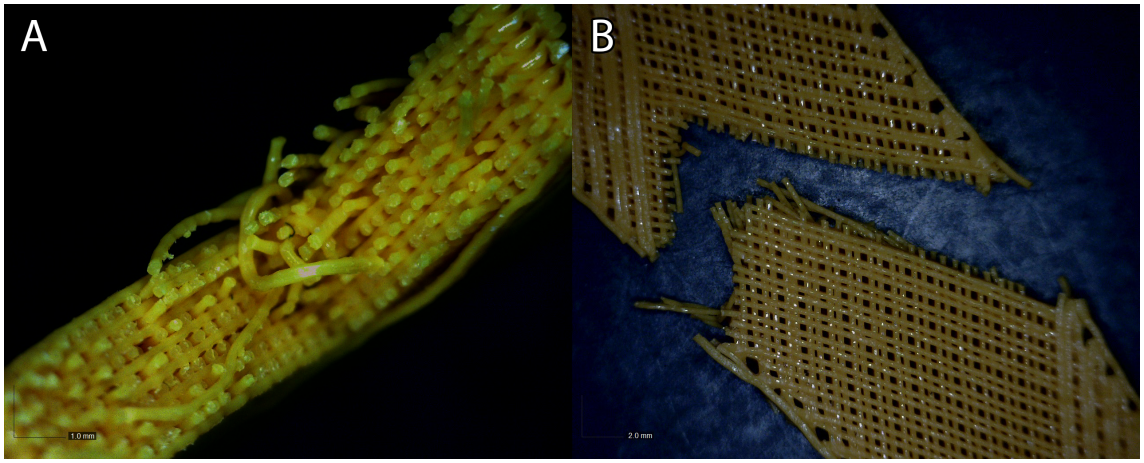

Figure 4.14: Micrographs of failed NinjaFlex TPU tensile test specimen four and five.

The specimen exhibits an angled fracture which would indicate shearing taking place. It was noted during testing that the failure happened gradually, starting at the outermost shell layer and moving into the infill. As previously mentioned in section 4.2.4, the porosity between the infill and shell layers differed between the samples. This is suggested to have caused a faster fracture for samples with a higher porosity. The 3D-printed filaments can be clearly seen in the cross-sectional fracture surface in Figure 4.14 (view A).

4.5 DMTA

The plots presented below present the storage (E') and loss (E") moduli and tan(δ) curves over temperature (°C) according to the ASTM D7028 standard [86]. The results are shown in a semi-log scale where the tan(δ) and temperature (°C) are using a linear scale. The resulting material properties from the DMTA are found in Table 4.8.

4.5.1 Measurements and results

The measured T_g is following the steps according to the ASTM D7028 standard [86]. The T_g and the peak temperature (T_t) of the tan(δ) curve are identified for comparison purposes. The results are presented in Table 4.8.

Table 4.8: Found material properties from the DMTA at 1 Hz with a specimen size of two.

Materials	**Glass-transition temperature T_g [°C]**	**Peak temperature T_t [°C]**
ABS (Innofil3D)	95.9	107.7
PLA (Primaselect)	50.26	56.94
TPU (NinjaFlex)	N/A[1]	N/A[1]
Nylon (Markforged)	N/A[2]	N/A[2]

To characterize the energy absorbing capabilities of the materials the tan(δ) from the DMTA tests was compared in a qualitative study between the materials. A lower tan(δ) peak value would mean the material has a high viscoelastic component, a material that exhibits both elastic and viscious characteristics, see section 3.6.1 for more details.

After the testing was performed for all specimens, a representative tan(δ)-curve was chosen for all materials and later compared in section 4.6. The ramp temperature rate was set to 2 °C/min, a non-standard value, for all materials except for nylon due to its thickness causing a higher bending stiffness in the single cantilever bending.

After testing, it was noted that all specimens had a slight increase in thickness. This swell was notably the largest on the ABS specimens. Generally, noise was noted in the regions above T_g. This is however not considered a problem because the region of interest for these studies is the T_g region, i.e. where the material softens.

[1] DMTA not performed due to $T_g < 0$ °C according to manufacturer.
[2] T_g not found in the 25–120 °C DMTA temperature region.
[3] Not available from manufacturer.

Table 4.9: Material properties provided by manufacturer.

Materials	Glass-transition temperature T_g (°C)	Peak temperature T_t (°C)
ABS (Innofil3D)	105	N/A[3]
PLA (Primaselect)	60	N/A[3]
TPU (NinjaFlex)	-35	N/A[3]
Nylon (Markforged)	49	N/A[3]

4.5.2 ABS

The DMTA results for Innofil3D ABS specimens 1 and 2 can be seen in Figure 4.15. The found T_g in the DMTA, see Table 4.8, conforms well with the manufacturer's datasheet seen in Table 4.9, only with a slight deviation of approximately 9 %.

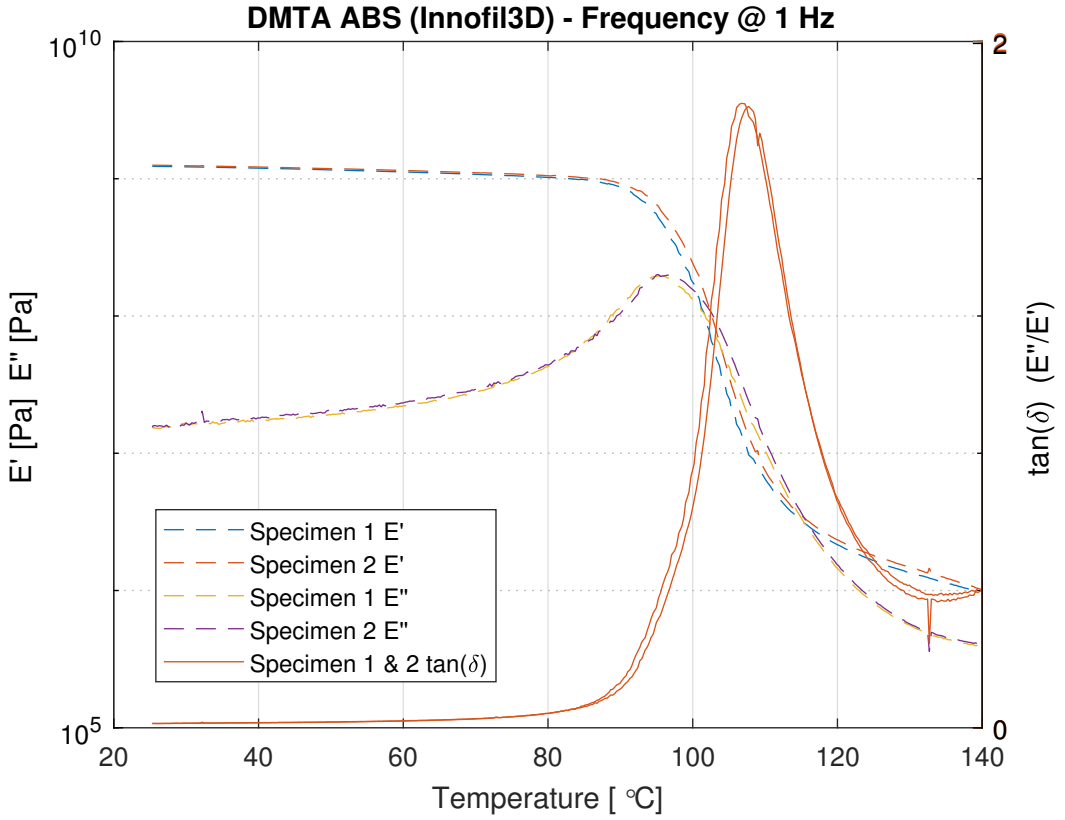

Figure 4.15: DMTA curves for 3D-printed Innofil3D ABS.

4.5.3 PLA

The DMTA results for Primaselect PLA specimens 4 and 5 can be seen in Figure 4.16. When testing of PLA specimens 1–3 there was considerable noise found in the plots. Therefore, only PLA specimens 4 and 5 are presented in the Results section. For specimens 4 and 5, noise in the curves began after 80 and 70 °C respectively. The found T_g agrees well with the one provided by the manufacturer with approximately 16 % difference.

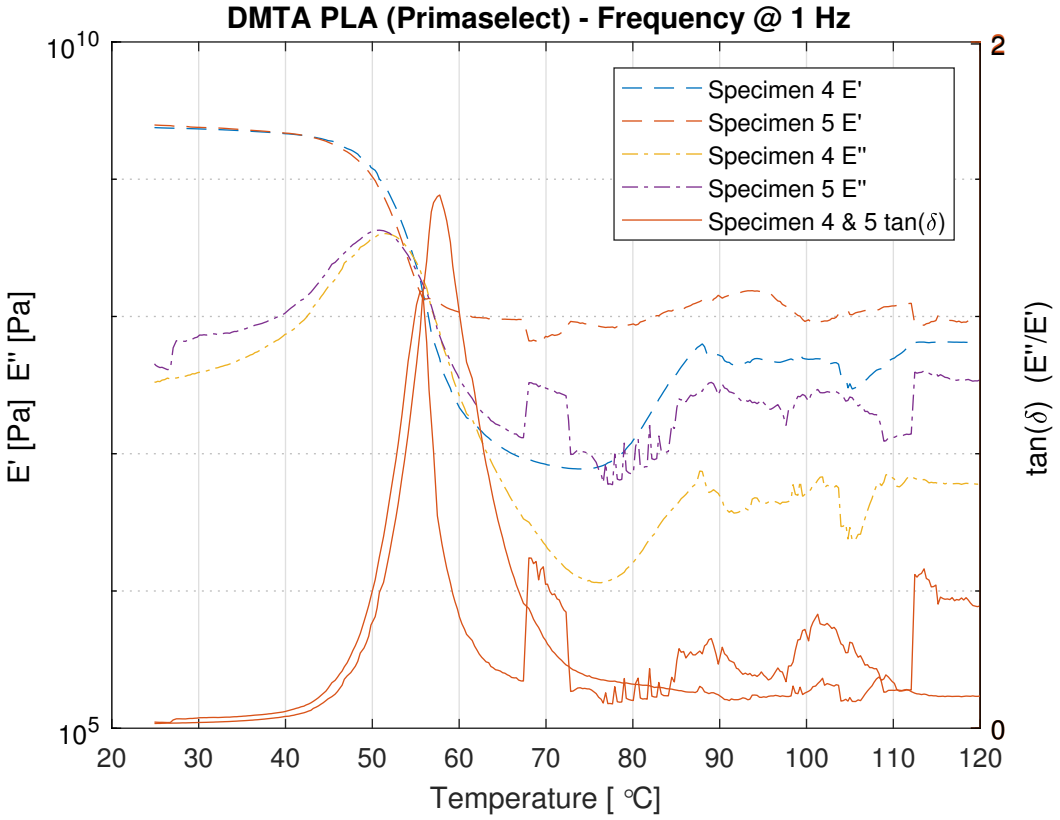

Figure 4.16: DMTA curves for 3D-printed Primaselect PLA.

The noise might be caused by slippage in the holder according to the ASTM D7028 standard [86]. The slippage is indeed a possible cause due to the clamps of the fixture being considerably worn upon inspection (smooth surfaces). Therefore, a higher tightening torque of 40 cNm was used for specimens 4 and 5. The noise was reduced considerably over the lower temperature range but there was still noise at elevated temperatures around 70–120 °C. The torque used for all other materials was following the 30 cNm standard for single cantilever DMTA according to the Rheometrics DMTA Mark IV (section 3.8.1) handbook.

Another probable cause for the noise seen in the plots around the 70–80 °C region might be crystallization of the PLA, which is further discussed in section 4.7.

4.5.4 TPU

DMTA testing of TPU (NinjaFlex) was not performed due to temperature region limitations. As seen in Table 4.9, the material sheet provided by NinjaTek for NinjaFlex TPU has a glass-transition temperature (T_g) of -35 °C. The temperature span of the DMTA tests was held coherent for all materials (25–140 °C) and only in the positive temperature region. The T_g for NinjaFlex TPU was therefore not determined in this study.

Tensile loading mode would have been the choice of method for the TPU. According to the ASTM D7028 standard [86], loading modes such as tensile, torsion or shear may produce different test results. This should have been taken into consideration when comparing the TPU with the other materials.

4.5.5 Nylon

Determining the T_g from the DMTA curve was not possible. This is due to there being no drop in the storage modulus (E'). Examples of non-ideal curves where the T_g cannot be determined are available in Appendix A1 of the ASTM D7028 standard document [86].

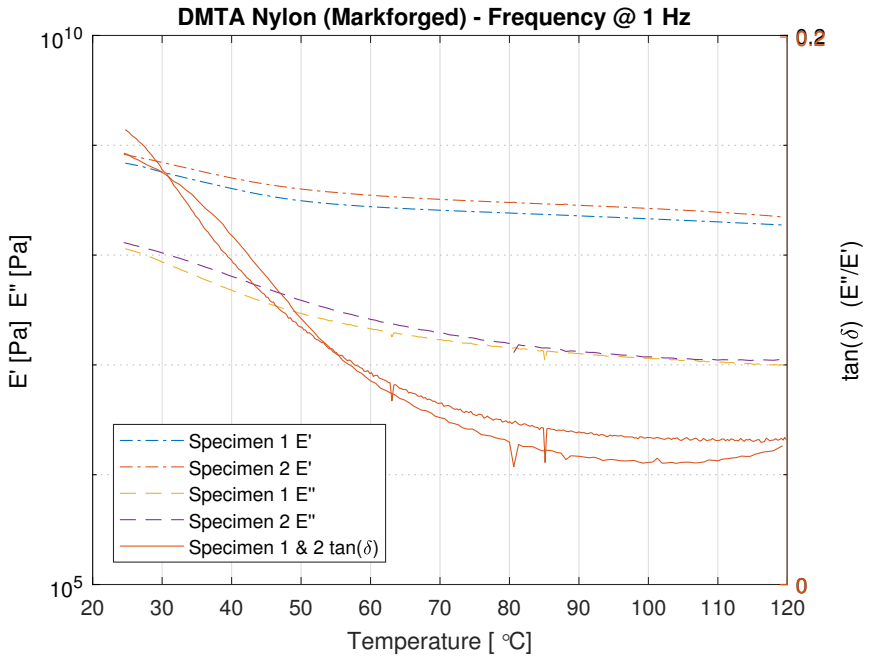

Figure 4.17: DMTA curves for 3D-printed Markforged nylon.

The temperature ramp rate was set to 5 °C/min for both nylon specimens, due to the softer elastomer behaviour of the material compared to the more rigid ABS and PLA. This is the recommended ramp rate according to the ASTM D7028 standard [86].

Additionally specimens 3 and 4 were tested using sharper grips in the testing rig, ideally used for stiffer materials. The tightening torque was set slightly lower than the standard: 25 cNm. The strain was set to 0.05 %. Still no T_g could be determined.

According to the manufacturer datasheet, see table 4.9, a glass-transition should occur at 49 °C. This did however not occur in a temperature range of 25–120 °C in this study. Comparing Markforged nylon with nylon 6 and nylon 66 the T_g should occur similarly in the range 50–60, 60–70 °C respectively [91]. An additional potential reason might be crystallization of the nylon.

Another possible reason for the missing T_g could be the influence of moisture in the nylon. Tests on nylon performed by Perkin Elmer shows how the humidity acts as a plasticizer in nylon and thus decreases the T_g with nearly 40 °C [92].

Additional tests on using plasticizers to decrease the T_g in nylon 6 was performed by Milliman et al. [14] which could suggest that the T_g for nylon by Markforged is lower than room temperature (25 °C).

As already mentioned, the importance of a flat and ground specimen is crucial for yielding interpretable DMTA results. It was noted after testing, that the curvature of the nylon specimens had increased, this might be another possible reason why the loss modulus (E') tends to just decrease slowly in the tested temperature region (25–120 °C), without any drop. The specimens also had a noticeable swell situated in the middle of the specimen, where the material is free to expand in between the holder and clamps.

Additionally, the standard used by Markforged is ASTM D648: *Standard Test Method for Deflection Temperature of Plastics Under Flexural Load in the Edgewise Position*, a way of measuring the T_g for plastics. As the requirements are not met for the tests performed in this study, this could be another reason for unsuccessful calculation of the T_g of nylon by Markforged.

Finally, the possibility of not changing the infill pattern in a such way that the material appears as a solid is thought to be the main reason why determination of the T_g in this study fails. The quality of the specimens are of such high importance that this alone serves as a motivation as to why no T_g could be found. Further investigation to determine whether this is related to orientation is needed. The layers are, as stated in the 3D-printing software section 3.4.2, positioned in a [-45°/45°] orientation in this study. Information about the structure of the nylon by Markforged was limited. Furthermore, investigation into the crystallinity of the nylon material is suggested. A microscope image of the DMTA nylon specimen can be seen in Figure 4.18.

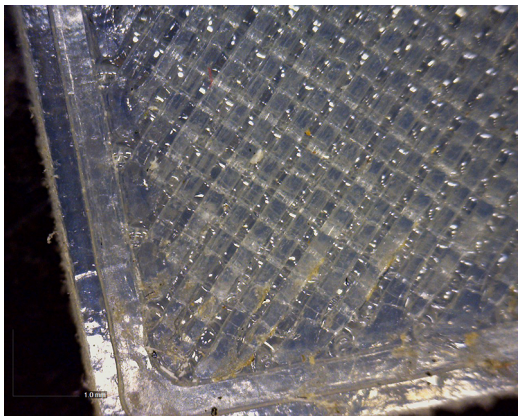

Figure 4.18: Microscopy image of nylon, showing the 45° layer orientation.

4.6 Loss tangent comparison

The comparison of the tan(δ) for ABS, PLA and nylon, i.e. the energy absorption capability of the material, can be seen in Figure 4.19.

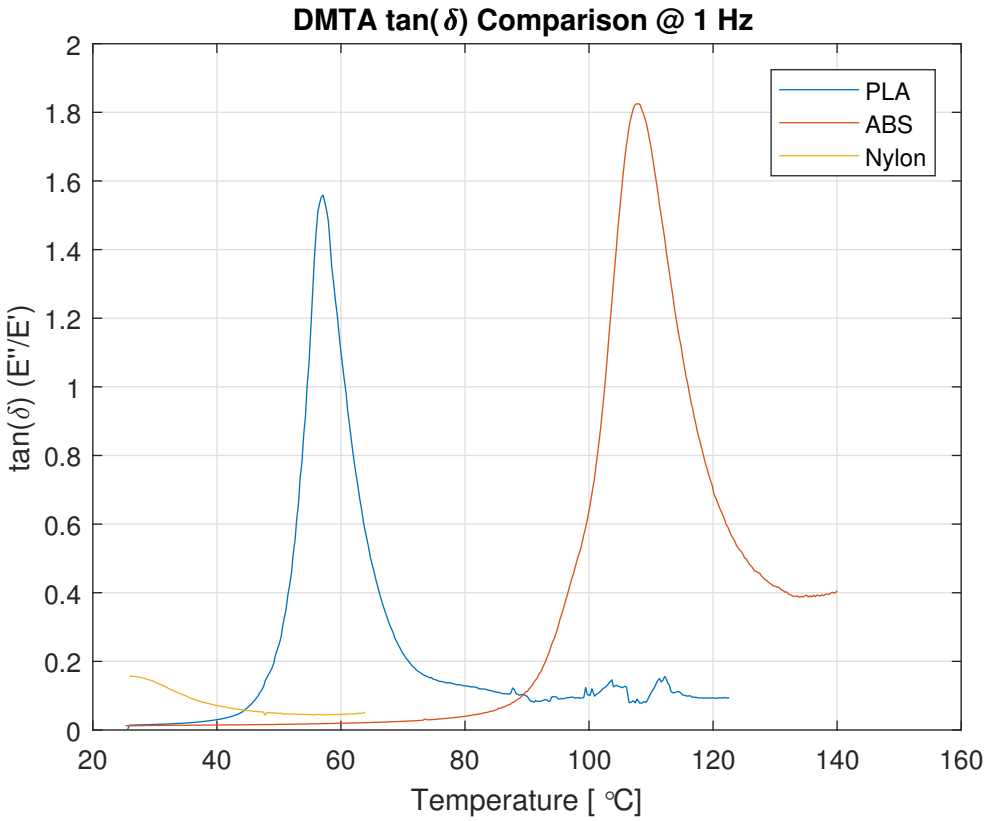

Figure 4.19: Representative tan(δ) curves for ABS, PLA and nylon.

The ABS exhibits a higher T_t compared to PLA and no T_g was found for the nylon which results in no T_t, i.e. peak temperature of tan(δ).

Generally, polymers has a very high damping factor (tan(δ)). Damping is the material's ability to dissipate energy under cyclic load. It is a measurement of how well a material can get rid of energy and is reported as tan(δ). The data tell us how good the polymer will be at absorbing energy. It varies with the state of the polymer, its temperature, and frequency [84].

For the performed DMTA, a frequency of 1 Hz was used and the temperature range was 25–120 °C. All polymers except nylon by Markforged had a defined T_g. The tan(δ) of ABS by Innofil3D exhibits the highest loss tangent, this would mean that it is best suited for an impact application of bicycle helmets. Worth noting is that this was only performed for a specific frequency of 1 Hz.

Additionally there is no perforance data for the NinjaFlex TPU as it would not show any T_g in the temperature range used. Also, nylon has no distinct T_g for either its storage modulus, loss modulus or loss tangent.

4.7 Storage modulus (E') comparison

In order to analyze the drop in storage modulus (E'), representative curves for all materials were chosen. The curves were all normalized for qualitative study. See Figure 4.20.

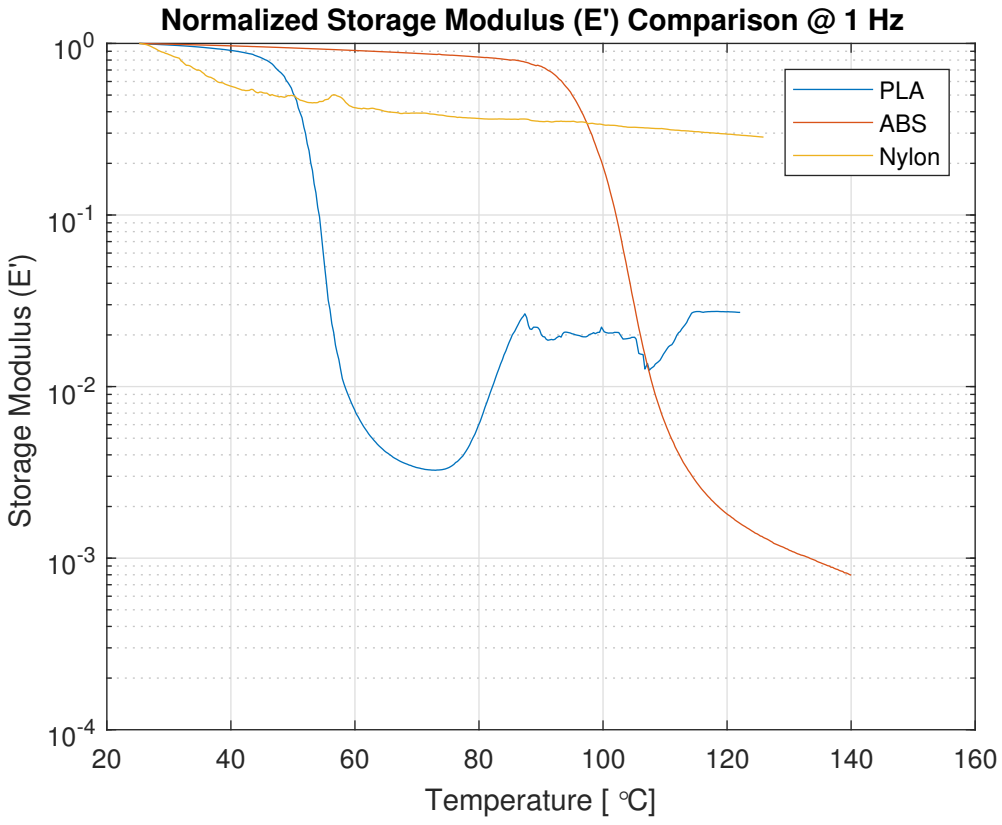

Figure 4.20: Representative E' curves for ABS, PLA and nylon.

According to CPSC's *Safety Standard for Bicycle Helmets* [94] the conditions for low, ambient and high temperature ranges are (-17 to -13), (17 to 27) and (47 to 53) °C respectively.

- The PLA experiences a drop at 45 °C which could be considered to occur in the high temperature range.
- ABS experiences its modulus drop at 90 °C which would be considered outside any standard temperature regions.
- Nylon does not experience any modulus drop within any standard temperature ranges tested in this study.

Nylon by Markforged would be the choice of material if the modulus is preferred to be held constant. Considerations regarding storage modulus (E') not being identical to the elastic modulus (E) are taken.

Additionally, this test is assuming a dynamic frequency of 1 Hz applied to the material which is not considered applicable in a practical crash situation where the material would rather be subjected to an initial high-load impact followed by minor bumps and sliding. This dynamic vibration case would however be a good representation of normal usage during changing weather conditions and/or riding over bumpy roads. However, this comparison between materials is only to be considered as a qualitative study and a first-step rough estimation. It should be noted that the frequency of 1 Hz is although considered a suitable reference frequency and changing this would not yield much more usable information of the material behavior.

The PLA is further experiencing an increase in its storage modulus (E') around 80 °C after the initial drop. This is thought to be due to the crystallization of the polymer. If the temperature ramp would be changed in the DMTA analysis, this crystallization would most likely not be experienced. Further investigation regarding ramp rate and crystallization of the polymer is needed. Additionally, T_g is only affecting amorphous materials and not crystals. If an additional DMTA would be performed on the supposedly crystallized PLA specimen, a different behaviour of the storage modulus would be found.

4.8 3D-printing challenges

Generally, long (time-consuming) prints in commercially available 3D-printers available today usually tend to fail due to mechanical system errors. Possible reasons include clogging in the extruding nozzle and slipping of filament in extruder feeding gear. This greatly limits the size and complexity of parts that require longer time to be printed. Additionally, the time to complete a print is generally extended by the cooling needed for individual filaments before additional filaments can be laid on top of them. One way to get around this, currently utilized in the medical industry, is to print multiple parts in parallel. Additional suggested ways include appropriate cooling mechanism or high speed gantry and precise bed leveling [49].

4.8.1 Printing time

There are mainly two factors affecting the time required for 3D-printing jobs:

- **Volume flow of the material:** basically how much material is being pushed through the nozzle at a certain flow rate. This factor is mainly controlled by the *extrusion multiplier* parameter.
- **Speed of the nozzle:** during deposition, the movement of the nozzle in the xy- and z-plane greatly affects the printing time. This is controlled by the various *printing speed* parameters.

The printing time is the product between the extrusion multiplier ($\dot{V}_{extrusion}$) and printing speed (v_{nozzle}):

$$\text{Printing time} = \dot{V}_{extrusion} \times v_{nozzle}$$

From a process perspective, finding an optimized choice of both parameters would be ideal. This could successfully decrease the lead time for print jobs and increase economical profit. However, these parameters were only adjusted based on empirical observations and experience in a discussion with printing experts at Swerea IVF.

4.9 Environmental and ecological impact

As previously mentioned, the ABS is a toxic thermoplastic with micro-particles as well as odor during printing of its filament [66]. From an environmental perspective, the PLA is clearly more environmentally friendly due to it being obtained from renewable sources [67]. The usage of PLA over typical petroleum-based polymers will reduce the demand on fossil fuels and ultimately reduce CO_2 emissions [71].

In the category of bio-polymers, PLA is today considered the best regarding stiffness, strength, low toxicity and as previously mentioned, recyclability. However PLA is very susceptible to moisture and a well known practice for its filament is to keep it free from moisture by using zip-lock bags. Improvements to such properties as moisture susceptibility are currently researched e.g. by utilizing composite compounds [68][69].

Thermoplastic polyurethane (TPU) presents a problem in the environmental aspect due to its resistance to biodegradation. However, research on addition of starches and vegetable oils to promote disintegration of TPU has been performed [58]. Recent research shows that addition of biodegradable cellulose derivatives to PU foams increases the foam's energy dissipating properties [57].

Nylon (PA6) is a widely used non-degradable petroleum-based material. Reusing PA6 has gained an increased interest due to more strict regulations towards environmental pollution, e.g. in automotive industry. PA6 can be reused via melt blending but recent studies by Pan et al. [59] have demonstrated a promising compression moulding technique which better preserves the mechanical properties, thus increasing the interest in reusing discarded PA6 [59].

4.10 Optimized lattice structure for energy absorbing applications

The compressive tests for the optimized lattice structures performed in the compressive testing rig mounted in the MTS/20 machine resulted in load vs. displacement curves. The three optimized structures were loaded up to 10 kN, the load limit of the load cell. The optimized lattice structures' load vs. displacement curves are presented in a qualitative comparison in Figure 4.21.

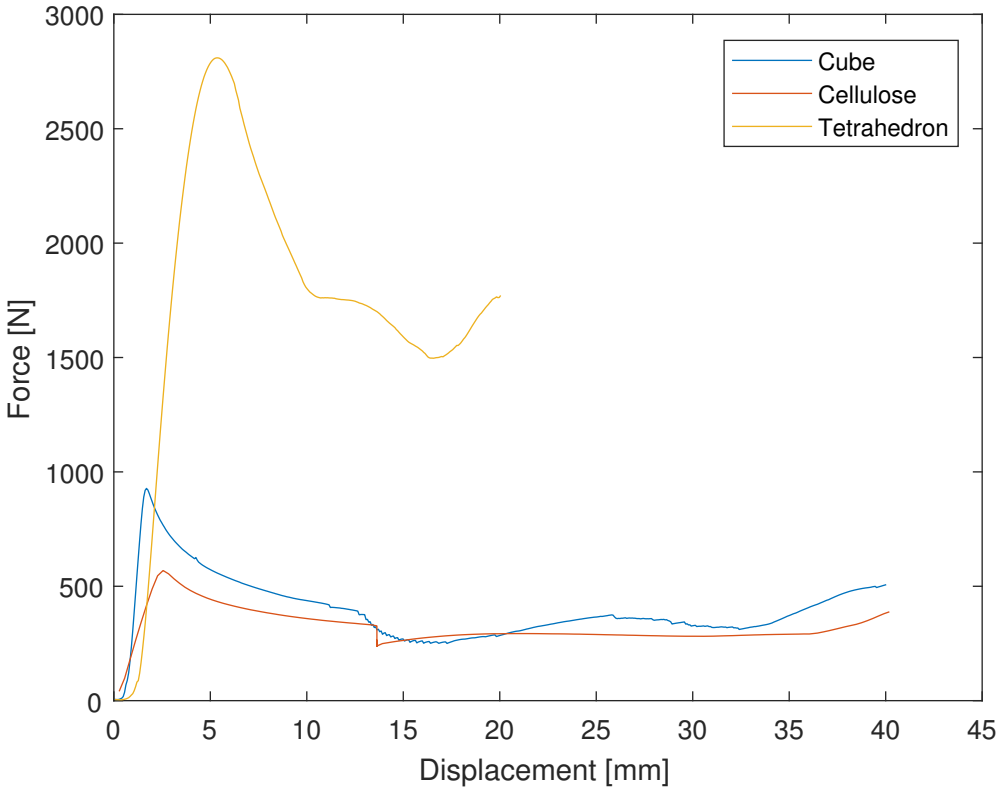

Figure 4.21: Load vs. displacement curves for the optimized nylon lattice structures.

The peak for each loading curve indicates where the structure fails to absorb any more energy. The ideal case would be where all the layers fail simultaneously, which would yield the highest energy absorption possible for the structure. The graphs were trimmed where the load strictly increased up to the max load of 10 kN. After this point, the solid material is simply being compressed and no relevant energy absorption properties are taken from this. Various elements that need to be taken into consideration for each of the structures are presented below:

- Cube: The structure expanded in the in-plane direction causing some difficulties to characterize the structural compressive behaviour from post-video analysis.

- Cellulose: During testing, technical difficulties were experienced causing the test to be performed in two steps. Testing was paused during the loading and this might have caused creep of the polymer during the static load. Additional artifacts found in the load vs. displacement-curve for the cellulose is suggested to be the cause of this.
- Tetrahedral: The support structures of the two bottom layers were not able to be completely removed during post processing. These supports may have caused increased load resistance for the structure during the compression test. This can be suggested from its superior performance and due to the two bottom layers not showing any buckling behavior compared to the two uppermost layers without support structures. The fractured layers can be seen in Figure 4.22.

The optimized lattice structures after testing are shown in Figure 4.22.

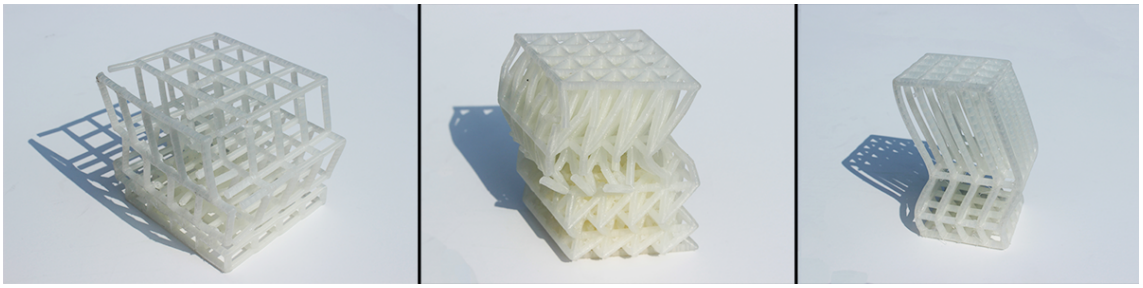

Figure 4.22: The three optimized lattice structures after the compressive test.

It can be clearly seen that the cellulose suffered the most severe fracture whereas the cube was found intact. The tetrahedron only fractured in the top two layers, this again is due to the support material not being removed from the bottom layers.

4.10.1 Conventional EPS foam vs. optimized lattice structures

Calculations by the parallel thesis project [51] on specific energy per kilogram on results for the optimized structures were performed. Additionally, specific energy for tests performed by Di Landro et al. [52] on conventional EPS foams were also determined. The resulting specific energy absorption values for various densities of conventional expanded polystyrene (EPS) foams and optimized lattice structures are presented in Table 4.10.

Table 4.10: Specific energy absorption for expanded polystyrene (EPS) and optimized lattice structures [51].

Specific energy for EPS and optimized lattice structures	
Conventional EPS foam	
Nominal density [g/l]	**Specific energy absorption [kJ/kg]**
28	3.93
40	4.25
55	4.55
70	5.43
Optimized lattice structure	
Structure	**Specific energy absorption [kJ/kg]**
Cube	3.27
Cellulose	1.56
Tetrahedron	2.73

The conventional EPS foam is superior regarding specific energy absorption. A conventional EPS foam of 70 g/l is absorbing approximately 100 % more energy than the tetrahedron, that had the highest energy absorption of all three lattice structures. However, it should be noted that the optimized lattice structures are all highly weight and material usage optimized whereas the EPS can basically be regarded as a high density solid foam material.

4.10.2 Snapshot sequence from video

The snapshots from the testing of the optimized cube, cellulose and tetrahedral structures are shown in Figure 4.23, Figure 4.24 and Figure 4.25 respectively. For demonstration purposes, five snapshots were acquired during compression loading and unloading.

Cube

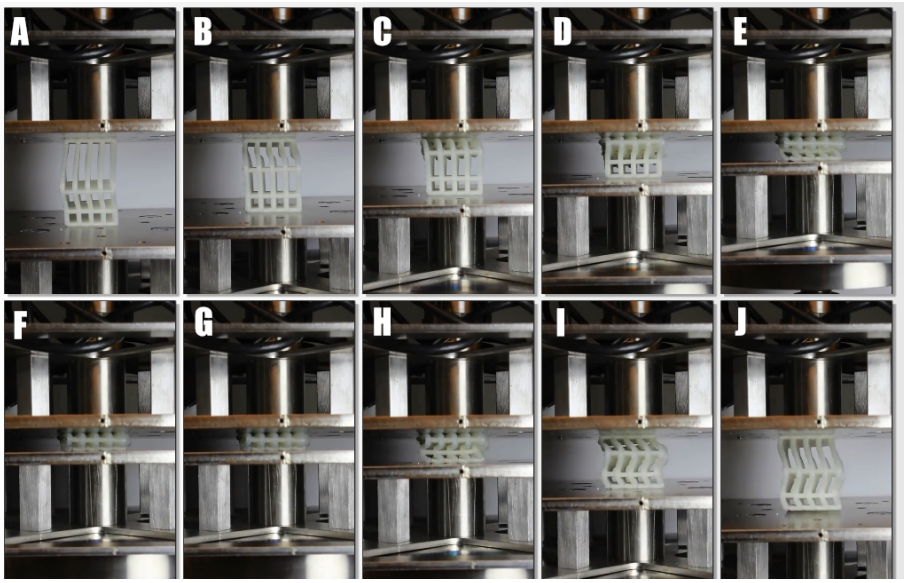

Figure 4.23: Snapshots of compressive test on cube structure from video recording. Images (A-E) show loading and images (F-J) show unloading.

Cellulose

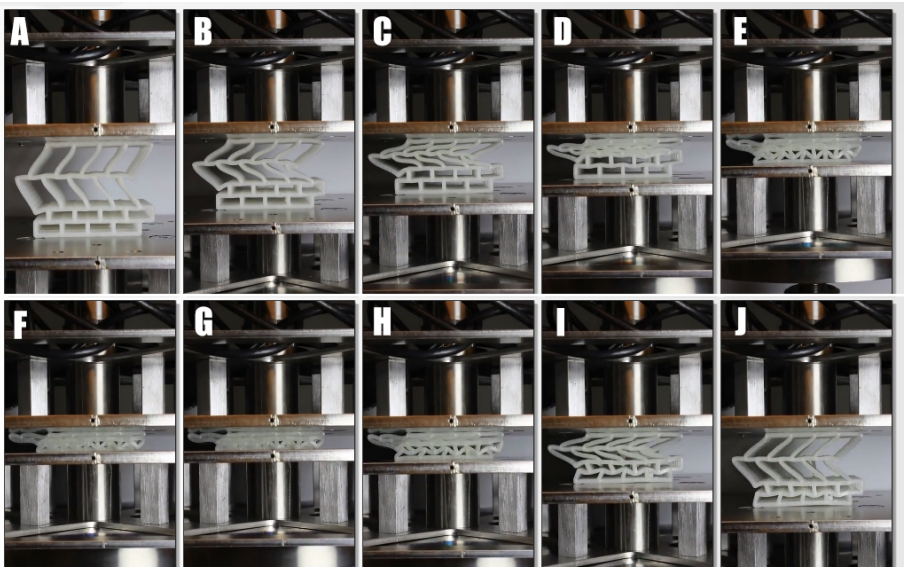

Figure 4.24: Snapshots of compressive test on the cellulose structure from video recording. Images (A-E) show loading and images (F-J) show unloading.

Tetrahedral

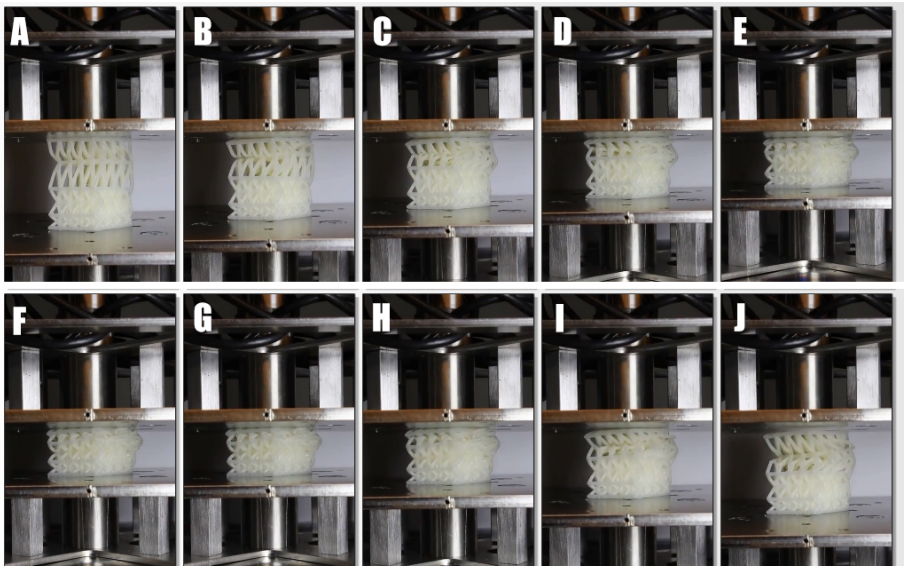

Figure 4.25: Snapshots of compressive test on the tetrahedral structure from video recording. Images (A-E) show loading and images (F-J) show unloading.

5

Conclusions

Various thermoplastic and elastomer 3D-printer filaments were characterized in this study. This comparison was suggested to be a unique contribution for comparison of 3D-printing filaments with widely different material properties.

As of today, there are two ways to mimic nature: tailoring the architecture and combining properties of multiple materials. In this study, a combination of the two approaches was made using various 3D-printer filaments.

The material nylon by Markforged was chosen to be the best material of the tested commercially available 3D-printing filaments, nylon, manufactured by Markforged performed best in energy-absorbing applications. This was due to its similarity in stress-strain behaviour with the ideal foam curve, the current material found in helmets today.

Finally, the EPS found in the energy-absorbing liner in today's protective helmet gear is absorbing approximately 100 % more specific energy [51] than the optimized tetrahedron lattice structure printed in this study, thus making it far superior in this aspect.

However, this study was intended to be a first step and act as a proof of concept in introducing optimized lattice structures inspired by nature as a lightweight substitute to EPS. This was conducted by using additive manufacturing technology and only using commercially available 3D-printer filaments.

6

Future Work

A suggestion for future research would be to use shorter specimens for the tensile tests. This would allow the usage of the optical extensometer recording for the full range of elongation until break (ϵ_B), especially for the TPU. This would show the behaviour up until break which is highly relevant in the case of energy absorbing and impact/crash applications. Additionally, a machine that can accommodate such high extensions is needed. Furthermore, a suggested testing method would be the ASTM D882 which utilizes thin plastic filament sheets as testing bars.

The finite element analysis (FEM) in the parallel thesis project only covered the linear-region of the material and used the assumption that the material is behaving isotropicaly. This caused only tensile testing to be performed in this study. However, in the energy absorption and impact/crash, a compression test would be suggested future work to correctly characterize the material behaviour in these applications. This would also provide validation for a non-linear FEM analysis. An additional testing method of interest would be impact testing (Charpy), where the behaviour in the presence of a crack could be characterized.

Optimization of printing parameters is highly suggested as future work, as this could increase the compressive performance of the structures but also decrease the printing time. Finally, further investigation into the usage of multi-material 3D-printers is considered the next step in mimicking the structures found in nature. Also, Stereolithography (SL) is one potential printing method for producing high resolution prints. Additionally, SL allows for water soluble support structures which would, in turn, ease the post processing.

No manufacturer datasheet of the filaments used in this study provides any loss tangent peak-temperatures, which is another common way to characterize the glass-transition region in DMTA. These values are therefore additionally seen as a contribution to the material characterization of the tested 3D-printer filament materials.

The DMTA was suggested to be unsuccessful in some cases due to the 3D-printed specimens not being complete solids. Investigation of whether this could be eliminated by optimizing the layer-orientations and infill is suggested. The TPU could also be tested in a single cantilever bending with a smaller frame, this would remove the extensive elastic behaviour of the specimens. Additionally the DMTA temperature range could be extended in the sub-zero temperature region to characterize the TPU.

An investigation of the PLA and its increased storage modulus (E') after an initial drop and its relation to the crystallization of the polymer is recommended. This would also suggest a simple crystallinity check for the different materials using the DMTA. Additionally the effect of the temperature ramp rate and its effect on crystallinity is also suggested.

Nylon by Markforged was the only polyamide (PA) characterized in this study. Further investigation of other nylon-like 3D-printing filament materials could further improve the energy absorbing performance of the optimized lattice structures.

The structures were all tested in a 4x4 lattice structure size, another suggestion would be to test individual 1x1 pillars of the optimized architectures with additional failure analysis of their fracture surfaces.

Furthermore, the optimized structures were free to move in the in-plane direction during testing. Using a test fixture where the in-plane movement is prohibited would be suggested to see how this affects the buckling and overall failure.

To further replicate the gradient density and material properties found in nature, one suggested way would be to use multi-material additive manufacturing techniques combining different material properties. However, attempts at mimicking these gradient structures by tailoring the architecture were performed in this study.

The ultimate objective would be to develop smart materials that can both detect a certain event and change the structural formation in response of said event, currently seen in for example bones of mammals. However, this is far from achievable in man-made materials as of today, although Wegst et al. [53] also suggest that this might be achievable within 10–20 years of continued research.

Bibliography

[1] McKittrick, J., Chen, P. Y., Tombolato, L., Novitskaya, E. E., Trim, M. W., Hirata, G. A., Meyers, M. A. (2010). "Energy absorbent natural materials and bioinspired design strategies: A review". Materials Science and Engineering C, 30(3), 331–342. https://doi.org/10.1016/j.msec.2010.01.011

[2] Fernandes, F. A. O., & Alves De Sousa, R. J. (2013). Motorcycle helmets - A state of the art review. Accident Analysis and Prevention, 56, 1–21. https://doi.org/10.1016/j.aap.2013.03.011

[3] Chen, I. H., Kiang, J. H., Correa, V., Lopez, M. I., Chen, P., Mckittrick, J., & Meyers, M. A. (2011). Armadillo armor : Mechanical testing and microstructural evaluation. Journal of the Mechanical Behavior of Biomedical Materials, 4(5), 713–722. https://doi.org/10.1016/j.jmbbm.2010.12.013

[4] Martin, R. B. (2003). Bones: structure and mechanics. (J. D. Currey, Ed.), Journal of Biomechanics. New Jersey: Princeton University Press. https://doi.org/10.1016/S0021-9290(03)00033-2

[5] Weaver, J. C., Milliron, G. W., Miserez, a., Evans-Lutterodt, K., Herrera, S., Gallana, I., ... Kisailus, D. (2012). The Stomatopod Dactyl Club: A Formidable Damage-Tolerant Biological Hammer. Science, 336(6086), 1275–1280. https://doi.org/10.1126/science.1218764

[6] Svensson, E., 2017. Bicycle/BMX helmet. Unpublished photograph.

[7] Ma, X. L. (2013). Research on Application of SLA technology in the 3D printing technology. Frontiers of Manufacturing Science and Measuring Technology Iii, Pts 1-3, 401, 938–941. https://doi.org/10.4028/www.scientific.net/AMM.401-403.938

[8] Kim, G. H., Lee, O. S., & Yoo, S. S. (1997). Experimental Study on Impact Absorbing Performance of Motorcycle Helmets. KSME International Journal, 11(3), 292–299. https://doi.org/10.1007/BF02946321

[9] Kapok Seeds. I, J.M.Garg via Wikimedia Commons from Wikimedia Commons https://commons.wikimedia.org/wiki/File%3AKapok_seeds_I_IMG_8004.jpg. Retrieved at 2017-05-04.

[10] FDM Process. Jona (Own work) via Wikimedia Commons from Wikimedia Commons https://commons.wikimedia.org/wiki/File:Filament_Driver_diagram.svg. Retrieved at 2017-05-05.

[11] Seki, Y., Schneider, M. S., & Meyers, M. A. (2005). Structure and mechanical behavior of a toucan beak. Acta Materialia, 53(20), 5281–5296. https://doi.org/10.1016/j.actamat.2005.04.048

[12] Sergey Bibikov and Mikhail Prokof'Ev (2011). Composite Materials for Some Radiophysics Applications, Metal, Ceramic and Polymeric Composites for Various Uses, Dr. John Cuppoletti (Ed.), ISBN: 978-953-307-353-8, InTech, Available from: http://www.intechopen.com/books/metal-ceramic-and-polymeric-composites-forvarious-uses/composite-materials-for-some-radiophysics-applications

[13] Berinskii, I., & Krivtsov, A. (2015). Shell and Membrane Theories in Mechanics and Biology (Vol. 45). https://doi.org/10.1007/978-3-319-02535-3

[14] Milliman, H. W., Ishida, H., & Schiraldi, D. A. (2012). Structure property relationships and the role of processing in the reinforcement of nylon 6-poss blends. Macromolecules, 45(11), 4650–4657. https://doi.org/10.1021/ma3002214

[15] Lino, F. J., Vasconcelos, P. V., Neto, R. J. L., & Paiva, R. (2008). Stereolitography, the Front Edge of Rapid Prototyping. Materials Science Forum, 587–588, 998–1002. https://doi.org/10.4028/www.scientific.net/MSF.587-588.998

[16] Gao, H. (2006). Application of fracture mechanics concepts to hierarchical biomechanics of bone and bone-like materials. International Journal of Fracture, 138(1–4), 101–137. https://doi.org/10.1007/s10704-006-7156-4

[17] Helmets.org: Liners. http://www.helmets.org/liners.htm retrieved at 2017-02-03.

[18] Veale, P. (2010). Investigation of the Behavior of Open Cell Aluminum Foam, (May). Retrieved from http://scholarworks.umass.edu/theses/443/

[19] Expanded Polystyrene Australia. http://epsa.org.au/about-eps/what-is-eps/how-is-eps-made/ retrieved at 2017-03-08.

[20] Compact bone. Lord of Konrad (2009). Wikimedia Commons from Wikimedia Commons https://commons.wikimedia.org/wiki/File%3ACompact_bone.png. Retrieved at 2017-05-08.

[21] Chen, P. Y., Lin, A. Y. M., McKittrick, J., & Meyers, M. A. (2008). Structure and mechanical properties of crab exoskeletons. Acta Biomaterialia, 4(3), 587–596. https://doi.org/10.1016/j.actbio.2007.12.010

[22] Raabe, D., Romano, P., Sachs, C., Al-Sawalmih, A., Brokmeier, H. G., Yi, S. B., ... Hartwig, H. G. (2005). Discovery of a honeycomb structure in the twisted plywood patterns of fibrous biological nanocomposite tissue. Journal of Crystal Growth, 283(1–2), 1–7. https://doi.org/10.1016/j.jcrysgro.2005.05.077

[23] Wegst, U. G. K., & Ashby, M. F. (2004). "The mechanical efficiency of natural materials". Philosophical Magazine, 21(21), 2167–2181. https://doi.org/10.1080/14786430410001680935

[24] Ashby, M. F. (2017). "Materials Selection in Mechanical Design". 5th edition, published by Butterworth Heinemann.

[25] Pohl, G., & Nachtigall, W. (2015). Biomimetics for Architecture & Design (2nd ed.). Stuttgart: Springer International Publishing Switzerland 2015. https://doi.org/10.1007/978-3-319-19120-1

[26] Gibson LJ, Ashby MF. Cellular solids: structure and properties. Cambridge university press; 1999 Jul 22.

[27] Young, M. F. (2003). Bone matrix proteins: their function, regulation, and relationship to osteoporosis. Osteoporosis International : A Journal Established as Result of Cooperation between the European Foundation for Osteoporosis and the National Osteoporosis Foundation of the USA, 14 Suppl 3, S35-42. https://doi.org/10.1007/s00198-002-1342-7

[28] DeMarco, A. L., Chimich, D. D., Gardiner, J. C., & Siegmund, G. P. (2016). The impact response of traditional and BMX-style bicycle helmets at different impact severities. Accident Analysis and Prevention, 92, 175–183. https://doi.org/10.1016/j.aap.2016.03.027

[29] Martin, J. J., Fiore, B. E., & Erb, R. M. (2015). Designing bioinspired composite reinforcement architectures via 3D magnetic printing. Nature Communications, 6, 8641. https://doi.org/10.1038/ncomms9641

[30] Ritchie, R. O., Buehler, M. J., & Hansma, P. (2009). Plasticity and toughness in bone. Physics Today, 62(6), 41–47. https://doi.org/10.1063/1.3156332

[31] Fantner, G. E., Rabinovych, O., Schitter, G., Thurner, P., Kindt, J. H., Finch, M. M., Hansma, P. K. (2006). Hierarchical interconnections in the nano-composite material bone: Fibrillar cross-links resist fracture on several length scales. Composites Science and Technology, 66(9), 1202–1208. https://doi.org/10.1016/j.compscitech.2005.10.005

[32] Katti, D. R., Pradhan, S. M., & Katti, K. S. (2010). Directional dependence of hydroxyapatite-collagen interactions on mechanics of collagen. Journal of Biomechanics, 43(9), 1723–1730. https://doi.org/10.1016/j.jbiomech.2010.02.027

[33] Li, L., Sun, Q., Bellehumeur, C., & Gu, P. (2002). Composite Modeling and Analysis for Fabrication of FDM Prototypes with Locally Controlled Properties. Journal of Manufacturing Processes, 4(2), 129–141. https://doi.org/10.1016/S1526-6125(02)70139-4

[34] Fonda, C. (2013). A Practical Guide to Your First 3D Print. Low-Cost 3D Printing for Science, Education and Sustainable Development. http://sdu.ictp.it/3D/ retrieved at 2017-02-16.

[35] Dimas, L. S., Bratzel, G. H., Eylon, I., & Buehler, M. J. (2013). Tough composites inspired by mineralized natural materials: Computation, 3D printing, and testing. Advanced Functional Materials, 23(36), 4629–4638. https://doi.org/10.1002/adfm.201300215

[36] H.J. Gao, B.H. Ji, I.L. Jaeger, E. Arzt and P. Fratzl, “Materials Become Insensitive to Flaws at Nanoscale: Lessons from Nature,” 2003, Proceedings of the National Academy of Sciences of USA, Vol. 100, pp. 5597–5600.

[37] H.J. Gao, “Application of Fracture Mechanics Concepts to Hierarchical Biomechanics of Bone and Bone-like Materials,” 2006, International Journal of Fracture, Vol. 138, pp. 101–137.

[38] Compton, B. G., & Lewis, J. A. (2014). 3D-printing of lightweight cellular composites. Advanced Materials, 26(34), 5930–5935. https://doi.org/10.1002/adma.201401804

[39] Azarov, A. V., Antonov, F. K., Vasil’ev, V. V., Golubev, M. V., Krasovskii, D. S., Razin, A. F., ... Khaziev, A. R. (2017). Development of a two-matrix composite material fabricated by 3D printing. Polymer Science, Series D, 10(1), 87–90. https://doi.org/10.1134/S1995421217010026

[40] Weng, Z., Wang, J., Senthil, T., & Wu, L. (2016). Mechanical and thermal properties of ABS/montmorillonite nanocomposites for fused deposition modeling 3D printing. Materials & Design, 102, 276–283. https://doi.org/10.1016/j.matdes.2016.04.045

[41] Thakur, V. K., & Thakur, M. K. (2014). Processing and characterization of natural cellulose fibers/thermoset polymer composites. Carbohydrate Polymers, 109, 102–117. https://doi.org/10.1016/j.carbpol.2014.03.039

[42] Aziz, M. S., & El sherif, A. Y. (2015). Biomimicry as an approach for bio-inspired structure with the aid of computation. Alexandria Engineering Journal, 707–714. https://doi.org/10.1016/j.aej.2015.10.015

[43] Hwang, J., Jeong, Y., Park, J. M., Lee, K. H., & Hong, J. W. (2015). Biomimetics : forecasting the future of science , engineering , and medicine, 5701–5713.

[44] Brennan-Craddock, J., Brackett, D., Wildman, R., & Hague, R. (2012). The Design of Impact Absorbing Structures for Additive Manufacture. Journal of Physics: Conference Series, 382(1), 12042. https://doi.org/10.1088/1742-6596/382/1/012042

[45] Bates, S. R. G., Farrow, I. R., & Trask, R. S. (2016). 3D printed polyurethane honeycombs for repeated tailored energy absorption. Materials and Design, 112, 172–183. https://doi.org/10.1016/j.matdes.2016.08.062

[46] Brett Compton, "3D printing of composites with controlled architecture" in "Composites at Lake Louise (CALL 2015)", Dr. Jim Smay, Oklahoma State University, USA Eds, ECI Symposium Series, (2016). http://dc.engconfintl.org/composite_all/37

[47] Kochesfahani, S. H. (2016). Improving PLA-based Material for FDM 3D-Printers Using Minerals (Principles and Method Development). Spe Antec, 1958–1614.

[48] Generic stress-strain graph for a ductile material. Moondoggy via Wikimedia Commons from Wikimedia Commons. [GFDL (http://www.gnu.

org/copyleft/fdl.html) or CC-BY-SA-3.0 (http://creativecommons.org/licenses/by-sa/3.0/)] https://commons.wikimedia.org/wiki/File%3AStress-strain1.svg. Retrieved at 2017-05-31.

[49] Wimpenny, D. (2009). 3D Printing, Rapid Prod. https://doi.org/10.1007/978-1-4842-0904-2_3

[50] Pandey, R. (2014). "Photopolymers in 3D printing applications". Plastics Technology. http://urn.fi/URN:NBN:fi:amk-2014081213420

[51] Alexander Olsson & Mattias Naarttijärvi (2017). Design Optimization for 3D Printed Energy Absorbing Structures Inspired by Nature. Applied Mechanics Department Chalmers, Gothenburg.

[52] Di Landro, L., Sala, G., & Olivieri, D. (2002). Deformation mechanisms and energy absorption of polystyrene foams for protective helmets. Polymer Testing, 21(2), 217–228. https://doi.org/10.1016/S0142-9418(01)00073-3

[53] Wegst, U. G. K., Bai, H., Saiz, E., Tomsia, A. P., Ritchie, R. O., Ortiz, C., ... Ritchie, R. O. (2014). Bioinspired structural materials. Nature Materials, 14(1), 23–36. https://doi.org/10.1038/nmat4089

[54] Soe, S. P., Martin, P., Jones, M., Robinson, M., & Theobald, P. (2015). Feasibility of optimising bicycle helmet design safety through the use of additive manufactured TPE cellular structures. International Journal of Advanced Manufacturing Technology, 79(9–12), 1975–1982. https://doi.org/10.1007/s00170-015-6972-y

[55] Sanladerer, T & Walker,S (2017). Filaween - Explore and compare 3D printing filaments. https://www.filaween.com/#/about

[56] ASTM D638-14 Standard Test Method for Tensile Properties of Plastics, ASTM International, West Conshohocken, PA, 2014, https://doi.org/10.1520/D0638-14

[57] Rivera-Armenta, J. L., Heinze, T., & Mendoza-Martínez, A. M. (2004). New polyurethane foams modified with cellulose derivatives. European Polymer Journal, 40(12), 2803–2812. https://doi.org/10.1016/j.eurpolymj.2004.07.015

[58] John K. Borchardt, Improving polyurethane biodegradability, Materials Today, Volume 7, Issue 11, 2004, Page 25, ISSN 1369-7021, http://dx.doi.org/10.1016/S1369-7021(04)00497-3 (http://www.sciencedirect.com/science/article/pii/S1369702104004973)

[59] Pan, G., Zhao, Y., Xu, H., Hou, X., & Yang, Y. (2016). Compression molded composites from discarded nylon 6/nylon 6,6 carpets for sustainable industries. Journal of Cleaner Production, 117, 212–220. https://doi.org/10.1016/j.jclepro.2016.01.030

[60] Fernandez-Vicente, M., Calle, W., Ferrandiz, S., & Conejero, A. (2016). Effect of Infill Parameters on Tensile Mechanical Behavior in Desktop 3D Printing. 3D Printing and Additive Manufacturing, 3(3), 183–192. https://doi.org/

10.1089/3dp.2015.0036

[61] MakerBot (2017). MakerBot Replicator 2 Desktop 3D printer User Manual, One MetroTech Center, 21st Floor, Brooklyn, NY. http://downloads.makerbot.com/replicator2/MakerBot_Replicator2_user_\manual.pdf retrieved at 2017-03-09.

[62] MakerBot (2017). MakerBot Replicator 2x Desktop 3D printer User Manual, One MetroTech Center, 21st Floor, Brooklyn, NY. http://downloads.makerbot.com/replicator2x/MakerBot_Replicator2X_User-Manual_Eng.pdf retrieved at 2017-03-16.

[63] MakerBot (2017). MakerBot Replicator 2x Desktop 3D printer troubleshooting, One MetroTech Center, 21st Floor, Brooklyn, NY. http://download.makerbot.com/replicator2x/MakerBot_Replicator_2X_Troubleshooting___Maintenance.pdf retrieved at 2017-03-21.

[64] Swerea SICOMP Piteå (2016). Tensile testing of Nylon document "3D_Dragprover_Nylon.xlsx". Retrieved at 2017-04-20.

[65] MakerBot (2017). Custom settings, One MetroTech Center, 21st Floor, Brooklyn, NY. https://support.makerbot.com/learn/makerbot-desktop-software/print-settings/custom-settings_11912 retrieved at 2017-03-12.

[66] Azimi, P., Zhao, D., Pouzet, C., Crain, N. E., & Stephens, B. (2016). Emissions of Ultrafine Particles and Volatile Organic Compounds from Commercially Available Desktop Three-Dimensional Printers with Multiple Filaments. Environmental Science and Technology, 50(3), 1260–1268. https://doi.org/10.1021/acs.est.5b04983

[67] Gutierrez, R.,Raquel, C. (2016). Improving the engineering properties of PLA for 3D printing and beyond, ProQuest Dissertations Publishing.

[68] M. A. Huneault and H. Li. Morphology and properties of compatibilized polylactide/thermoplastic starch blends. Polymer 48(1), pp. 270-280. 2007.

[69] B. Imre, K. Renner and B. Pukánszky. Interactions, structure and properties in poly (lactic acid)/thermoplastic polymer blends. Express Polymer Letters 8(1), 2014.

[70] Grunenfelder, L. K., Suksangpanya, N., Salinas, C., Milliron, G., Yaraghi, N., Herrera, S., ... Kisailus, D. (2014). Bio-inspired impact-resistant composites. Acta Biomaterialia, 10(9), 3997–4008. https://doi.org/10.1016/j.actbio.2014.03.022

[71] E. T. H. Vink, K. R. Rábago, D. A. Glassner and P. R. Gruber. Applications of life cycle assessment to NatureWorks™ polylactide (PLA) production. Polym. Degrad. Stab. 80(3), pp. 403-419. 2003. . DOI: http://dx.doi.org/10.1016/S0141-3910(02)00372-5

[72] MoldMaking Technology (2014). Nylon FDM Material Offers Greater Strength, Additive manufacturing. Cincinnati,

USA. http://www.additivemanufacturing.media/products/stratasys-nylon-fdm-material-offers-greater-strength

[73] Shubham, P., Sikidar, A., & Soni, T. C. (2016). The Influence of Layer Thickness on Mechanical Properties of the 3D Printed ABS Polymer by Fused Deposition Modeling, 706, 8–12. https://doi.org/10.4028/www.scientific.net/KEM.706.63

[74] Song, Y., Li, Y., Song, W., Yee, K., Lee, K.-Y., & Tagarielli, V. L. (2017). Measurements of the mechanical response of unidirectional 3D-printed PLA. Materials & Design, 123, 154–164. http://dx.doi.org/10.1016/j.matdes.2017.03.051

[75] Kamaljit Singh Boparai, Rupinder Singh, Harwinder Singh, (2016) "Process optimization of single screw extruder for development of Nylon 6-Al-Al2O3 alternative FDM filament", Rapid Prototyping Journal, Vol. 22 Issue: 4, pp.766-776, doi: 10.1108/RPJ-09-2014-0119

[76] 3D Hubs (2017). Master of ninja flex on Makerbot Replicator 2 and 2x. https://www.3dhubs.com/talk/thread/master-ninja-flex-makerbot-replicator-2-and-2x retrieved at 2017-03-15.

[77] Qiao, L., Dong, X., Ying, Y., Zheng, J., Li, W., & Che, S. (2016). Toughening mechanism of PPS/Sr ferrite composites by TPU elastomer. Journal of Applied Polymer Science, 133(25), 6–11. https://doi.org/10.1002/app.43564

[78] 3D Matter (2017). What is the influence of infill %, layer height and infill pattern on my 3D prints?, New Lab, Brooklyn, NY. http://my3dmatter.com/influence-infill-layer-height-pattern/ retrieved at 2017-03-15.

[79] Horvath, J., & Cameron, R. (2015). Mastering 3D Printing. The New Shop Class, Rapid Prod, 31–46. https://doi.org/10.1007/978-1-4842-0904-2_3

[80] EngineerDog (2014). Mechanical Testing 3D Printed Parts: Results and Recommendations, Beavercreek, OH, USA. https://engineerdog.com/2015/09/02/mechanical-testing-3d-printed-parts-results-and-recommendations/ retrieved at 2017-03.15.

[81] Wood, B. M. (2015). Multifunctionality in Additive Manufacturing. Design and Manufacture of Plastic Components for Multifunctionality: Structural Composites, Injection Molding, and 3D Printing. Elsevier Inc. https://doi.org/10.1016/B978-0-323-34061-8.00005-3

[82] Moscato, S., Bahr, R., Le, T., Pasian, M., Bozzi, M., Perregrini, L., & Tentzeris, M. M. (2016). Infill-Dependent 3-D-Printed Material Based on NinjaFlex Filament for Antenna Applications. IEEE Antennas and Wireless Propagation Letters, 15, 1506–1509. https://doi.org/10.1109/LAWP.2016.2516101

[83] Rankouhi, B., Javadpour, S., Delfanian, F., & Letcher, T. (2016). Failure Analysis and Mechanical Characterization of 3D Printed ABS With Respect to Layer Thickness and Orientation. Journal of Failure Analysis and Prevention, 16(3), 1–15. https://doi.org/10.1007/s11668-016-0113-2

[84] Principles of Polymer Engineering by N.G. McCrum, C.P Buckley and C.B. Bucknall (MBB), 2nd ed., 1997, Oxford Science Publications (Oxford University Press), ISBN 19 856526 7

[85] Dana, M. & Howard, K. 2000, "Tension, Compression, Bend, and Shear Testing" in ASM International, pp. 1-2.

[86] ASTM D7028-07(2015), Standard Test Method for Glass Transition Temperature (DMA Tg) of Polymer Matrix Composites by Dynamic Mechanical Analysis (DMA), ASTM International, West Conshohocken, PA, 2015, www.astm.org

[87] ASTM D882-12 Standard Test Method for Tensile Properties of Thin Plastic Sheeting, ASTM International, West Conshohocken, PA, 2012, https://doi.org/10.1520/D0882-12

[88] ASTM D3039/D3039M-14 Standard Test Method for Tensile Properties of Polymer Matrix Composite Materials, ASTM International, West Conshohocken, PA, 2014, https://doi.org/10.1520/D3039_D3039M-14

[89] Mills, N. J. (1990). Protective capability of bicycle helmets. British Journal of Sports Medicine, 24(1), 55–60. https://doi.org/10.1136/bjsm.24.1.55

[90] Markforged (2017). Markforged Materials, 10 Fawcett St, Cambridge, MA 02138, USA. https://markforged.com/materials/ retrieved at 2017-04-05.

[91] Lin S-K. Handbook of Polymers. By George Wypych, ChemTec Publishing, 2012; 680 Pages, ISBN 978-1-895198-47-8. Polymers. 2013; 5(1):225-233.

[92] PerkinElmer, Inc. (2007). Nylon 6 – Influence of Water on Mechanical Properties and Tg. 940 Winter Street Waltham, MA 02451 USA. Available at: http://www.perkinelmer.com/CMSResources/Images/46-74182APP_InfluenceofWaterOnMechPropsandTG.pdf retrieved at 2017-04-20.

[93] Plastics - Determination of tensile properties - Part 1: General principles (ISO 527-1:2012)

[94] CPSC Bicycle helmet standard rules and regulations (1998). Publisher: Federal Register. Volume 63, number 46. Pages 11711-11747. From the Federal Register Online via GPO Access [https://www.gpo.gov/] [DOCID:fr10mr98-23]. Document available on alternative source: http://www.helmets.org/cpscstd.pdf retrieved at 2017-05-11.

A

Appendix

A.1 Tensile test specimens measurements

On the next page, the measurements of the tensile test specimens according to the ASTM D638 [56] are shown.

Table A.1: Tensile test specimen geometries according to the ASTM D638 standard [56].

Tensile Test Specimens Part Geometries (ASTM D638)		
Specimen number	**Width (w) [mm]**	**Thickness (t) [mm]**
ABS (Innofil3D)		
1	13.52	3.23
2	13.65	3.17
3	13.68	3.18
4	13.61	3.16
5	13.56	3.14
PLA (Primaselect)		
1	13.37	3.38
2	13.45	3.33
3	13.56	3.39
4	13.32	3.28
5	13.33	3.27
NinjaFlex TPU (NinjaTek)		
1	12.95	3.20
2	12.77	3.17
3	12.54	3.18
4	12.88	3.21
5	12.94	3.20
Nylon (Markforged)		
1	10.25	4.04
2	10.16	4.09
3	10.09	4.1
4	10.20	4.11
5	10.08	4.08
6	10.18	4.09
7	10.15	4.08

A.2 DMTA specimens measurements

Measurements of the DMTA test specimens are shown in Table A.2 below.

Table A.2: DMTA test bar part geometries.

DMTA Test Bars Part Geometries (Single cantilever bending)			
Specimen number	**Length (l) [mm]**	**Width (w) [mm]**	**Thickness (t) [mm]**
ABS (Innofil3D)			
1	35.63	10.53	3.00
2	35.46	10.37	2.99
PLA (Primaselect)			
4	35.09	10.11	2.04
5	35.25	10.18	2.02
Nylon (Markforged)			
1	35.29	10.27	1.99
2	35.48	10.23	1.68
3	35.15	10.18	2.12
4	34.94	10.03	1.38
NinjaFlex TPU (NinjaTek)			
1	34.67	10.03	2.03
2	34.63	9.91	2.01

A.3 Cellulose printing

The overview of the 3D-printed optimized cellulose structure is presented in Figure A.1. The illustration shows a cross-section of the structure and the table presents successful and failed beams. The total ratio of successful to failed prints is also presented.

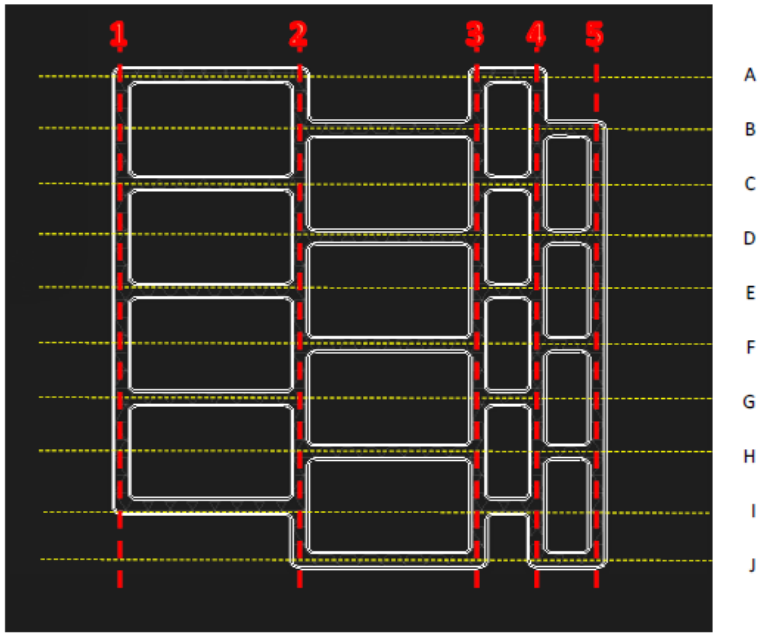

		column				
level	row	1	2	3	4	5
I	A	OK	OK	OK	OK	-
I	B	-	OK	OK	OK	OK
I	C	X	X	X	OK	-
I	D	-	X	OK	OK	OK
I	E	X	X	OK	OK	-
I	F	-	X	OK	OK	OK
I	G	X	/	X	OK	-
I	H	-	X	OK	OK	X
I	I	X	X	X	OK	-
I	J	-	X	OK	OK	OK
II	A	OK	OK	OK	OK	-
II	B	-	OK	OK	OK	OK
II	C	OK	OK	OK	OK	-
II	D	-	OK	OK	OK	OK
II	E	X	X	OK	OK	-
II	F	-	OK	OK	OK	OK
II	G	OK	OK	OK	X	-
II	H	-	OK	OK	OK	OK
II	I	OK	OK	OK	OK	-
II	J	-	X	OK	OK	OK
III	A	OK	OK	OK	OK	-
III	B	-	OK	OK	OK	OK
III	C	OK	OK	OK	OK	-
III	D	-	OK	OK	OK	OK
III	E	OK	OK	OK	OK	-
III	F	-	OK	OK	OK	OK
III	G	OK	OK	OK	OK	-
III	H	-	OK	OK	OK	OK
III	I	OK	OK	OK	OK	-
III	J	-	OK	OK	OK	OK
IV	A	OK	OK	OK	OK	-
IV	B	-	OK	X	OK	OK
IV	C	OK	OK	OK	X	-
IV	D	-	OK	OK	OK	OK
IV	E	OK	OK	OK	OK	-
IV	F	-	OK	OK	OK	OK
IV	G	OK	OK	OK	OK	-
IV	H	-	OK	OK	OK	OK
IV	I	OK	OK	OK	OK	-
IV	J	-	OK	OK	OK	OK

correct beams	OK	138
missing beams	X	21
semi-detached beams	/	1
total beams		160

Figure A.1: Complete overview of failed parts of the cellulose lattice structure.